

1996

# Scanning probe microscopies for the creation and characterization of interfacial architectures: studies of alkyl thiolate monolayers at gold

John-Bruce DeVault Green  
*Iowa State University*

Follow this and additional works at: <https://lib.dr.iastate.edu/rtd>

 Part of the [Materials Science and Engineering Commons](#), and the [Physical Chemistry Commons](#)

## Recommended Citation

Green, John-Bruce DeVault, "Scanning probe microscopies for the creation and characterization of interfacial architectures: studies of alkyl thiolate monolayers at gold " (1996). *Retrospective Theses and Dissertations*. 11527.  
<https://lib.dr.iastate.edu/rtd/11527>

This Dissertation is brought to you for free and open access by the Iowa State University Capstones, Theses and Dissertations at Iowa State University Digital Repository. It has been accepted for inclusion in Retrospective Theses and Dissertations by an authorized administrator of Iowa State University Digital Repository. For more information, please contact [digirep@iastate.edu](mailto:digirep@iastate.edu).

## INFORMATION TO USERS

This manuscript has been reproduced from the microfilm master. UMI films the text directly from the original or copy submitted. Thus, some thesis and dissertation copies are in typewriter face, while others may be from any type of computer printer.

**The quality of this reproduction is dependent upon the quality of the copy submitted.** Broken or indistinct print, colored or poor quality illustrations and photographs, print bleedthrough, substandard margins, and improper alignment can adversely affect reproduction.

In the unlikely event that the author did not send UMI a complete manuscript and there are missing pages, these will be noted. Also, if unauthorized copyright material had to be removed, a note will indicate the deletion.

Oversize materials (e.g., maps, drawings, charts) are reproduced by sectioning the original, beginning at the upper left-hand corner and continuing from left to right in equal sections with small overlaps. Each original is also photographed in one exposure and is included in reduced form at the back of the book.

Photographs included in the original manuscript have been reproduced xerographically in this copy. Higher quality 6" x 9" black and white photographic prints are available for any photographs or illustrations appearing in this copy for an additional charge. Contact UMI directly to order.

# UMI

A Bell & Howell Information Company  
300 North Zeeb Road, Ann Arbor MI 48106-1346 USA  
313/761-4700 800/521-0600



Scanning probe microscopies for the creation and characterization of interfacial  
architectures: Studies of alkyl thiolate monolayers at gold

by

John-Bruce DeVault Green

A dissertation submitted to the graduate faculty  
in partial fulfillment of the requirements for the degree of  
**DOCTOR OF PHILOSOPHY**

Major: Physical Chemistry  
Major Professor: Marc D. Porter

Iowa State University

Ames, Iowa

1996

**UMI Number: 9712555**

---

**UMI Microform 9712555**  
**Copyright 1997, by UMI Company. All rights reserved.**

**This microform edition is protected against unauthorized  
copying under Title 17, United States Code.**

---

**UMI**  
**300 North Zeeb Road**  
**Ann Arbor, MI 48103**

**Graduate College  
Iowa State University**

**This is to certify that the doctoral dissertation of**

**John-Bruce DeVault Green**

**has met the dissertation requirements of Iowa State University**

Signature was redacted for privacy.

**Major Professor**

Signature was redacted for privacy.

**For the Major Program**

Signature was redacted for privacy.

**For the Graduate College**

## **DEDICATION**

This dissertation is dedicated to my family, whose support and confidence were the most responsible for its completion, my wife Lie-Ling Wu, my brother Jere Green, and my parents John and Diana Green.

## TABLE OF CONTENTS

<b>ACKNOWLEDGMENTS.....</b>	<b>vi</b>
<b>ABSTRACT.....</b>	<b>vii</b>
<b>GENERAL INTRODUCTION.....</b>	<b>1</b>
Scanning Probe Microscopy.....	4
Scanning Tunneling Microscopy.....	8
Measurable Properties and Modes of Operation.....	9
Experimental Ranges.....	9
Scanning Force Microscopy.....	10
Measurable Properties and Modes of Operation.....	10
Experimental Ranges.....	18
Resolution Issues.....	18
Spontaneously Adsorbed Monolayers.....	19
Dissertation Organization.....	25
<b>STRUCTURAL CHARACTERIZATIONS.....</b>	<b>26</b>
SPM of Alkyl Thiolate Monolayers at Au(111).....	26
Molecular Scale Structure.....	27
Meso-Scale Structural Investigations Including Steps, Pits and Domain Boundaries.....	33
Surface Evolution.....	35
Barrier Properties and Structural Defects.....	36
Example Study (Counter-Intuitive Barrier Properties).....	38
Counter-Intuitive Response.....	38
Experimental.....	39
Models.....	41
Conclusions.....	52
Conclusions.....	52
<b>MATERIAL CHARACTERIZATIONS.....</b>	<b>54</b>
SPM Measured Mechanical Properties of Alkyl Thiolate Monolayers.....	54
Example Study (Chain-Length Dependent Friction).....	55
Experimental Section.....	56
Sample Preparation.....	56
Friction Measurements.....	57
SFM Image Acquisition.....	57
STM Image Acquisition.....	58
Results and Discussion.....	58
Microscopic Friction and Wear.....	58
Molecular Friction.....	62
Structural Correlations.....	66
Frictional Damping of Topographic Structures.....	69



Conclusions.....	73
Conclusions .....	73
<b>CHEMICAL INTERPRETATIONS.....</b>	<b>75</b>
Material Properties - Chemical Interpretations.....	75
Example Study (Functional Group Dependent Friction).....	77
Experimental Section.....	79
Sample Preparation.....	79
Friction Measurements.....	80
Image Acquisition.....	84
Results and Discussion .....	84
Conclusions.....	91
Conclusions .....	91
<b>REAL TIME <i>IN SITU</i> CHARACTERIZATIONS .....</b>	<b>93</b>
Example Study (Electrochemically Dependent Adhesion).....	93
Introduction .....	94
Experimental Section.....	94
Results and Discussion .....	96
Conclusions .....	103
<b>GENERAL CONCLUSIONS .....</b>	<b>104</b>
<b>FUTURE DIRECTIONS.....</b>	<b>107</b>
<b>APPENDIX: COMPREHENSIVE LISTING OF DEFECT MODELS.....</b>	<b>109</b>
<b>REFERENCES.....</b>	<b>128</b>

## ACKNOWLEDGMENTS

I would like to acknowledge that the results presented in this dissertation are a product of the combined efforts of myself with a select set of Marc Porter's research group, and to a lesser extent with the entire group. As the text includes four of my main projects, I thought it best to separately acknowledge some of the primary individual efforts that have significantly contributed to each. The counter-intuitive project was a true group effort, with data and interpretation from Christie McDermott, Chuanjian Zhong, and Mark McDermott. Christie and CJ both obtained electrochemical data, however, the success of the project is primarily a result of the high resolution STM images of domain boundaries that Christie obtained. These images in turn lead to the development of our models. The chain-length dependent friction project was primarily a two person effort spear-headed by Mark McDermott and myself. And it grew out of the investigations for the end-group dependent friction project which was similarly manned, with the exception being that it would probably never have been initiated if not for the foresight of Lorraine Siperko who got it started. Finally, although I consider the electrochemical adhesion project to be my own pet project, significant assistance was always forthcoming from both Mark and Vivian Jones. As always Marc was an ever-present guiding force for the development of these as well as my other projects.

I would also like to acknowledge the contributions of some specific group members who taught me the fundamentals of my research: Duane Weisshaar and Brian Lamp, who took the time to show a physical chemist/physicist how to do electrochemistry; Carla Alves who taught me about the intricacies of scanning probe microscopy; CJ, whose wisdom is only exceeded by his willingness to share it; and of course the many other members of the group, especially ManKit Ho, Randall Deinhammer, Vivian Jones, Bob Brush, and Neal Simmons for their comradery and support.

Additionally I should acknowledge that this work was performed at Ames Laboratory under Contract No. W-7405-Eng-82 with the U.S. Department of Energy, and the United States government has assigned the DOE Report number IS-T 1804 to this thesis.

## ABSTRACT

At this time, technology is approaching a point where molecular scale knowledge of interfacial architectures is required for further progress. The successful creation and characterization of functioning molecular scale architectures requires techniques which can probe the molecular structure and properties of these interfaces. Scanning probe microscopy (SPM) offers access to the structural and material properties of interfaces, and when combined with macroscopic characterization techniques results in a powerful interfacial development tool. However, the relative infancy of SPM techniques has dictated that initial investigations concentrate on model interfacial systems as benchmarks for testing the control and characterization capabilities of SPM. One such family of model interfacial systems results from the spontaneous adsorption of alkyl thiols to gold.

This dissertation examines the application of SPM to the investigation of the interfacial properties of these alkyl thiolate monolayers. Structural investigations result in a proposed explanation for counterintuitive correlations between substrate roughness and heterogeneous electron transfer barrier properties. Frictional measurements are used for characterization of the surface free energy of a series of end-group functionalized monolayers, as well as for the material properties of monolayers composed of varying chain length alkyl thiols. Additional investigations used these characterization techniques to monitor the real-time evolution of chemical and electrochemical surface reactions.

The results of these investigations demonstrates the value of SPM technology to the compositional mapping of surfaces, elucidation of interfacial defects, creation of molecularly sized chemically heterogeneous architectures, as well as to the monitoring of surface reactions. However, it is the future which will demonstrate the usefulness of SPM technology to the advancement of science and technology. These investigations are only a prelude to the more adventurous applications to molecular manufacturing, mechanically directed molecular synthesis, and other directions in the rapidly evolving fields of nanotechnology. While SPM will assist in controlling and understanding our current micro-technologies, it will be most

crucial to the next wave of the technological development for emerging molecular scale technologies.

## GENERAL INTRODUCTION

Interfacial phenomena have been, and continue to be, crucial to the expansion of technological boundaries. The creation and characterization of low dimensional architectures represent a crucial direction which interfacial investigations must proceed. Some key low dimensional systems include: a) 2-dimensional structures: polymer films, Langmuir-Blodgett monolayers and multilayers, spontaneously adsorbed monolayers (SAMs), etc. and b) 0- and 1-dimensional structures: molecular wires, molecular gates and channels, as well as other nanofabricated structures. The goals of these approaches are to design and manipulate these surface architectures in ways that optimize the rates and/or selectivities of the interfacial phenomena relevant to technologies such as catalysis, corrosion, energy production and storage, photoelectrochemistry, chemical analysis, synthesis, and nanotechnology [1, 2]. In many instances, approaches to modify reactivity exploit an alteration of the molecular architecture of the surface via the deposition of a thin organic film [3]. These approaches, however, contain a high degree of empiricism in that a projection of the performance of a surface often assumes a direct translation of the reactivity of a precursor in the three-dimensional environment of solutions for the lower dimensionality for an immobilized species at a surface.

Though useful as a starting point in the creation of novel interfaces, the lack of a detailed understanding of how immobilization can affect reactivity limits the ability to proceed predictively in subsequent design steps for optimization of performance. It is therefore important to develop insights into the fundamental issues that govern the chemistry and physics of interfaces by asking questions like:

1. What is the chemical identity of the immobilized species?
2. What is the mode of attachment, spatial orientation, coverage, and two-dimensional arrangement of the immobilized species?
3. How do the interactions between adsorbate, solvent, supporting electrolyte, and substrate influence the reactivity and stability of the immobilized species?

4. How does the size of the molecular scale architecture affect the reactivity and specificity of the immobilized species within or near the architecture?
5. How do thermal, entropic, processes affect the reactivity, specificity, or stability of the immobilized species within or near the architecture?

These questions are also relevant on a broader level to numerous other areas of surface and materials science, such as adhesion, biocompatibility, nanotechnology, and colloidal stabilization. For example, factors that facilitate the ionization of acidic functionalities at the surface of organic materials are crucial to the stabilization of polymer dispersions and colloidal solutions. Similarly, fundamental studies of electrocatalysis probe how adsorbate-substrate interactions perturb the electronic structure of an adsorbate and the subsequent impact of such perturbations on electron transfer kinetics. Additionally, the behavior of micromechanical devices is dominated by surface and interfacial properties, which are controlled by the chemical composition of that interface. Seeking answers to the above questions is therefore one of the most important and yet difficult challenges in interfacial science today.

To address the above questions, it is necessary to develop surface analytical techniques that probe the details of the interface at a molecular level. Ideally, such a method would produce information that would identify the types and quantities, spatial orientation, two-dimensional arrangement, and microscopic reactivities. In view of these requirements and the general complexity and diversity of interfaces, it is not surprising that the ideal surface probe is nonexistent. Thus, the application of an integrated approach that combines a carefully selected set of surface analysis probes represents a more tractable strategy. Such approaches generally employ techniques that can be divided into two broad groups. The first includes techniques that characterize interfaces at a macroscopic level, yielding details about the general (i.e., average) population of the immobilized species [4]. For example, techniques such as X-ray photoelectron spectroscopy (XPS) have been used to probe the elemental composition of surfaces, providing semi-quantitative data at sub-monolayer coverages; approaches have also been devised for the identification of chemical functionalities. However, the integrity of the observation may be compromised by the transfer of a sample into the

artificial environment of an ultra high vacuum chamber required for XPS. Vibrational spectroscopic techniques (e.g., infrared and Raman spectroscopes) open avenues for in situ characterizations as well as yield data directly attributable to the chemical identity and spatial orientation of an organic adsorbate. Contact angle measurements probe the macroscopic surface free energy, which may be interpreted to give structural information, e.g., order/disorder, orientation, etc.

The second class of techniques includes those that probe an interface at nanometer length scales. These techniques entail in large part the many forms of scanning probe microscopy (SPM). Following the invention of the scanning tunneling microscope (STM) [5], a family of derivative techniques have been developed, each which measure different properties, and thus interrogate different aspects of the interface. These techniques can be classified according to the properties being probed; STM measures a tunneling current; scanning force microscopy (SFM) measures interaction forces; scanning near-field optical microscopy (SNOM) measures optical light intensity. Not only can these microscopes probe the interfacial structure and properties with atomic resolution, but they can also be used to modify these interfaces. With the extraordinarily high spatial resolution of these microscopes direct chemical, or electrochemical, modification of molecular sized regions is viable, and the possible applications for microelectronics, microsensor arrays, nanofabrication, directed molecular synthesis, etc., invite future inquiry.

The central goal of the research in this dissertation has been the development of a better understanding of interfacial properties. Although the principle thrust has focused upon refinement of techniques for the characterization of monolayers, some subcurrents of this theme have focused on techniques for the creation and characterization of interfacial architectures with molecular dimensions. The research summarized herein demonstrates that significant progress toward that goal has been attained through the utilization of SPM technologies. The relative infancy of these techniques has dictated that initial investigations concentrate on model interfacial systems, as benchmarks for testing the control and characterization capabilities. Given the extensive experience which our group has with alkyl

thiolate monolayers at gold, the bulk of my research has exploited these as the model interfaces. The principle advances reported here include:

1. The development of models based on STM images, that are able to explain counter-intuitive correlations between substrate roughness and heterogeneous electron transport across alkyl thiolate monolayers at gold.
2. The development of an understanding of how frictional measurements made with SFM are affected by the material properties of the interface.
3. The development of an understanding of how frictional measurements made with SFM are affected by chemical interactions between the probe and the interface.
4. The application of SFM to follow the progress of electrochemical reactions.

Each of the above four points are examined in detail following a brief description, and literature review of SPM and SAMs. It should be noted that this literature review is not intended to be exhaustive, serving rather as a guide to key research papers that can be used as starting points for understanding SPM and SAMs.

## Scanning Probe Microscopy

This section presents an overview of scanning probe microscopies. Following a broad introduction to the fundamentals of SPM, two subsections detail the key aspects of scanning tunneling microscopy (STM) and scanning force microscopy (SFM). Figure 1 depicts the features common to all scanning probe microscopes: 1) a probe capable of interacting with a sample, and 2) a micropositioning device. The achievement of effective SPM relied upon one key technological step: the development and use of piezoelectric materials that could be used as nanopositioners. This extraordinary positional precision allowed sub-angstrom control over the position of the probe, and thus the potential measurement of properties with similar resolution. An image is created by scanning the sample, or probe, in a raster-like fashion while measuring the probe-sample interaction. There are two basic modes for controlling the sample-probe separation as the image is obtained, and are illustrated for the case of STM in Figure 2. In the *constant height mode*, the sample or probe is rastered in the xy plane (i.e., surface plane) without any change in the z position (i.e., surface normal) of either the sample



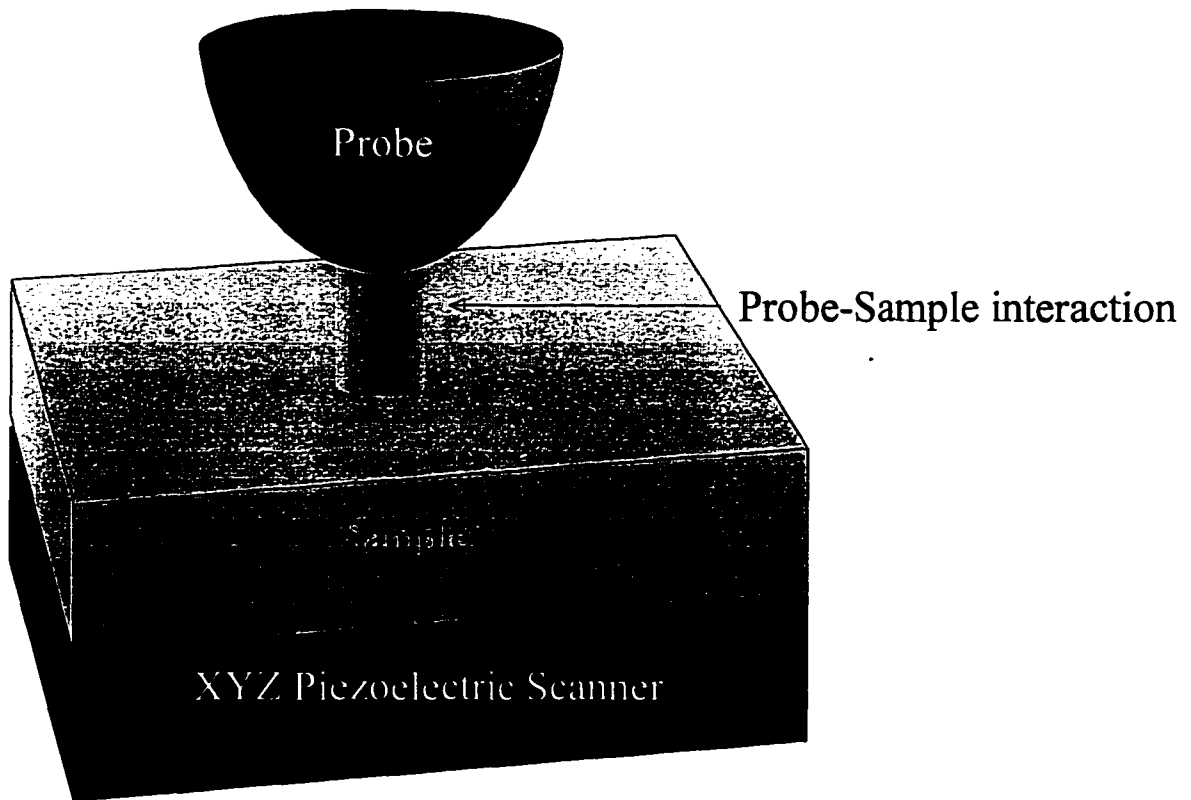
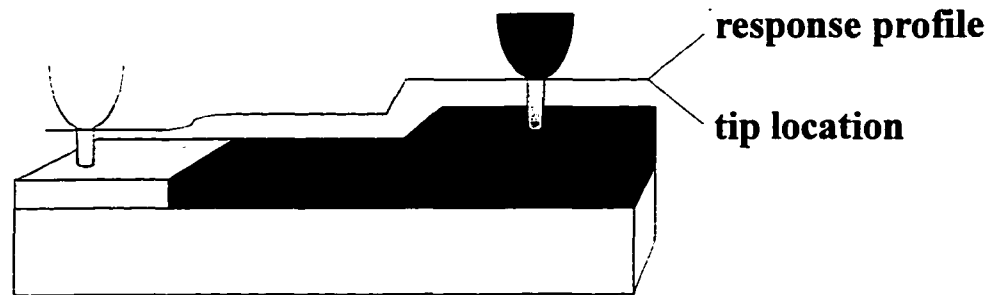


Figure 1 Schematic of SPM showing common instrumental features: 1) probe tip capable of measuring interfacial properties, and 2) a piezoelectric micropositioning system for scanning the sample or probe tip.

## Constant Current



## Constant Height

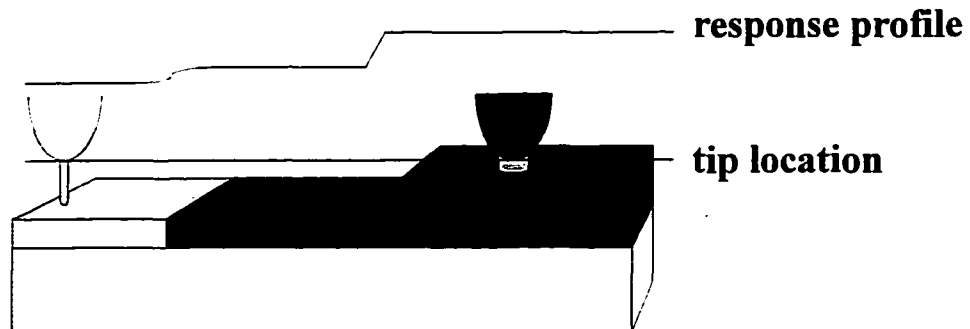



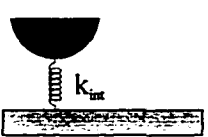
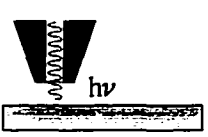
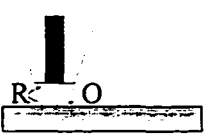
Figure 2

Schematic of STM modes of operation. In the *constant height mode*, the sample or probe is rastered in the  $xy$  plane (i.e., surface plane) without any change in the  $z$  position (i.e., surface normal) of either the sample or probe. In this mode the response is measured and plotted as a function of the  $xy$  coordinates. In the *constant interaction mode*, the sample-probe separation is varied to keep the measured property at a fixed setpoint value. Therefore, as the sample or probe is scanned in the  $xy$  plane, the  $z$ -position is plotted as a function of the  $xy$  coordinates.

or probe. In this mode, the response is measured and plotted as a function of the  $xy$  coordinates. In the *constant interaction mode*, the sample-probe separation is varied to keep the measured property at a fixed setpoint value. Therefore, as the sample or probe is scanned in the  $xy$  plane, the  $z$ - position is plotted as a function of the  $xy$  coordinates.

As the development of SPM progressed, there have been numerous technological advances to positional precision, vibrational isolation, as well as in the types and designs of the probes and detection. The original SPM, scanning tunneling microscopy (STM), has rapidly advanced to produce a wide set of derivative techniques, including scanning force microscopy (SFM), scanning electrochemical microscopy (SECM), scanning near-field optical microscopy (SNOM), scanning thermal microscopy (SThM). Table 1 lists a few of these derivative SPM techniques along with some important parameters. While each of these techniques offers unique approaches to interfacial characterizations and surface modification, my research concentrated on applications of STM and SFM, and the following subsections introduce some of the critical aspects of these two techniques.

**Table 1 Probe-Sample Interactions**

	<b>Transduction Mechanism</b>	<b>Schematic</b>	<b>Critical Variables</b>
STM	tunneling current		electronic states of both the probe and the sample, morphology of the probe and sample
SFM	interaction forces		short range interactions: electrostatic repulsion, compression, long range interactions: van der Waals, double layer, coulombic, etc.
SNOM	optical detection		transmission, absorption, fluorescence, reflection, ...
SECM	electrochemical current		redox species concentration, substrate conductivity, radius of electrode

## Scanning Tunneling Microscopy

There have been several in-depth discussions on both the theory of and issues in the application of STM as a surface characterization tool [6, 7, 8]. Operationally, STM employs piezoelectric micropositioners to position an atomically sharp metal tip and conductive sample surface within a few angstroms of each other. At such separations, the electron wavefunctions of the two surfaces overlap, allowing electrons to tunnel through the classically insulating barrier between the two surfaces. Upon application of a bias voltage,  $V_b$ , between the probe and sample, a net tunneling current flows. The images are composed from maps of the tunneling current as the tip rasters across the surface. Since the wave function of a surface decays exponentially into the insulating barrier, the dependence of the tunneling current exhibits a marked sensitivity to separation of a tip and sample, and can be roughly approximated by the one-dimensional model represented below, where  $s$  is the probe-sample separation,  $\kappa$  is the inverse decay length, for Au  $\kappa \approx 12 \text{ nm}^{-1}$ , and the proportionality constant is related to the local density of states (LDOS) accessed at a given bias voltage between the probe and sample. The decay length is related to the height of the potential energy barrier through which the electron must tunnel. Since the imaging current is a function of the electron states of both the probe and the sample, STM images represent a mixing of both structural and electronic factors. Although this mixing poses complications for structural interpretation of the images, it opens up the possibilities for STM to perform spectroscopic analysis, even to create maps of electron tunneling spectra. By holding the probe-sample separation fixed, the tunneling current may be monitored as the bias voltage is varied. In this way, the electron tunneling spectrum may be obtained as a function of sample location. However, the interpretation of these spectra are complicated by the uncertainties associated with the probe, as its morphology, surface chemistry, and surface states are not well understood and can vary between tips. In attempts to clarify the structure and states of the probe, some studies have examined the field emission/ion microscopy (FEM/FIM) images of the probe [9]; however, these are limited to cases in ultra high vacuum (UHV) conditions where FEM/FIM techniques are operative. The bulk of STM studies are concerned with

surface morphology, generally assuming that local electronic effects caused by surface states are only of limited influence.

### **Measurable Properties and Modes of Operation**

The STM probes one measurable surface property, tunneling current. The measurement of this current is achieved through conventional electronic means. The various modes of operation generally concentrate on monitoring the DC or AC components to the tunneling current, or alternatively varying levels of feedback, as shown in Figure 2. The AC techniques apply an oscillating bias voltage to the tip-sample couple, and monitor the corresponding AC current. Differences in the amplitude and phase of this AC current give information about the sample conductivity, and surface LDOS. Our investigations focused on the structural imaging produced with STM, operating in a DC constant current mode.

### **Experimental Ranges**

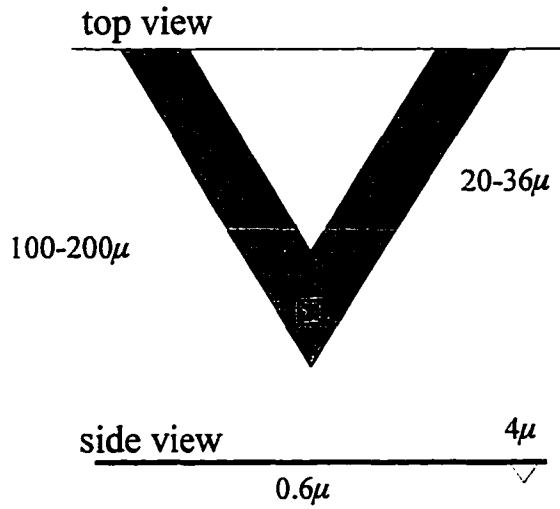
The most prominent experimental limitation of STM is that there must be somewhere for the electrons to tunnel. Previously, such imaging has required conductive substrates; however, recent efforts have obtained STM images of insulating substrates by using an adsorbed water layer as the conductive surface. So at this time STM may be applied to virtually any substrate, under the appropriate conditions [10]. The STM is therefore environmentally versatile, as it can image conductors in conditions ranging from the pristine conditions of UHV to the severe conditions required for in situ electrochemical experiments. While the structural investigation of conductors are readily attainable, the incorporation of an organic, and often insulating, film at the electrode surface complicates theoretical explanations of tunneling processes considerably. Probe-sample interaction forces produced during STM imaging can become quite large, often large enough to irreversibly disrupt an organic adlayer. In an effort to minimize these forces, the probe-sample separation should be maximized. To withdraw the probe to a position above the organic film extremely low currents are required. The range of these tunneling currents are limited by electrical noise and amplifier components, and are currently limited to about 1 pA.

## Scanning Force Microscopy

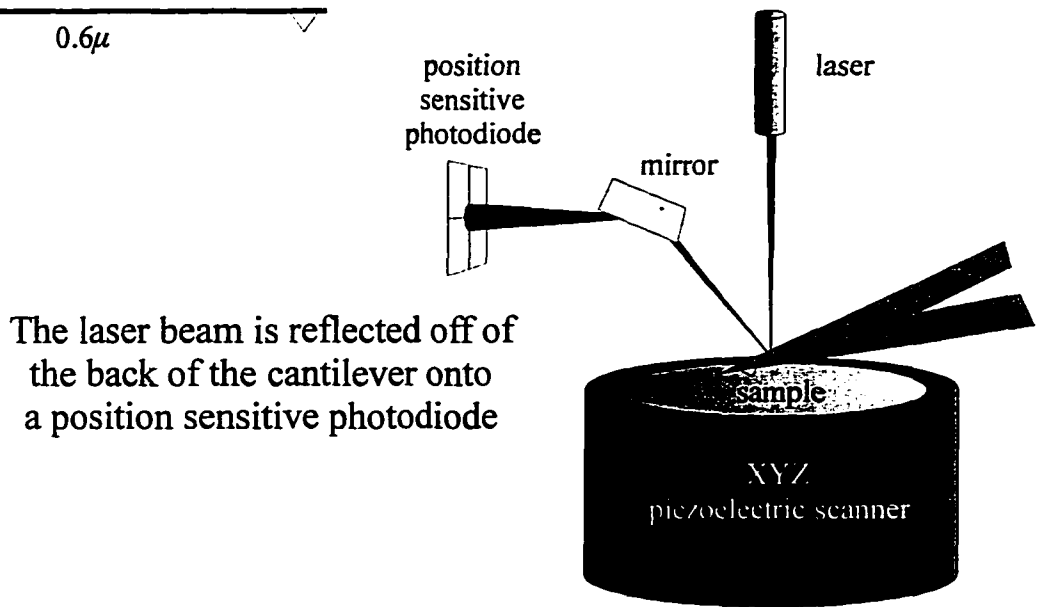
A number of excellent reviews of SFM are available, which range from broad introductions [11, 12, 13] to detailed examinations of fundamental [14, 15], and design [16] issues. Operationally, SFM is not that different from STM; a probe is rastered over a surface while measuring a property. The fundamental difference lies with the interaction being measured, while STM measures a tunneling current, SFM measures the physical deflection of a cantilever mounted tip. Unlike the STM, there is not a comparatively simple distance dependence to the probe-sample interaction. This situation reflects the complex set of molecular interactions that can arise between two molecules. An excellent introduction into the kinds of forces at work can be found in the text by Israelachvili on intermolecular and surface forces [1]. There is a rich set of operative interactions, and that is what makes the SFM a valuable and versatile probe.

### Measurable Properties and Modes of Operation

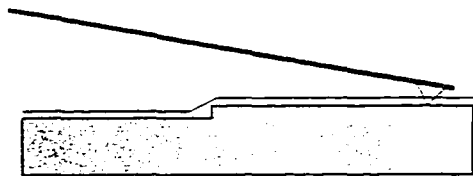
SFM relies on one measurable transduction mechanism: the deflection of a cantilever. However, unlike STM there are a number of different methods for detecting the deflection of the cantilever, including: capacitance [17], interferometry [15], STM [5], optical beam deflection [14], and others. All of the experimental data presented herein were obtained from an optical beam deflection type SFM, of similar design to that shown in Figure 3, equipped with a commercially available microfabricated cantilever. A laser beam is reflected off of the back of a cantilever, onto a mirror, and then onto a position sensitive photodiode. The optical lever created by this reflected beam has the effect of amplifying the deflections of the cantilever resulting in vertical deflection detection limits on the order of 0.1 nm. Commercially available cantilevers [18] come in a wide range of size shape and material composition ( $\text{Si}_3\text{N}_4$ , Si, etc.), yielding a range of force constants ( $\sim 0.001$ -100 N/m), radius of curvature ( $\sim 5$ -100 nm), and the appropriate choice of cantilever type is an important decision which should be determined according to the goals for each experiment. For example, molecular imaging of compliant monolayers should use a sharp probe with a small force constant, and be conducted in liquid to minimize excessive capillary forces. In contrast,



The probe is a pyramidal  $\text{Si}_3\text{N}_4$  tip on a cantilever beam



The laser beam is reflected off of the back of the cantilever onto a position sensitive photodiode



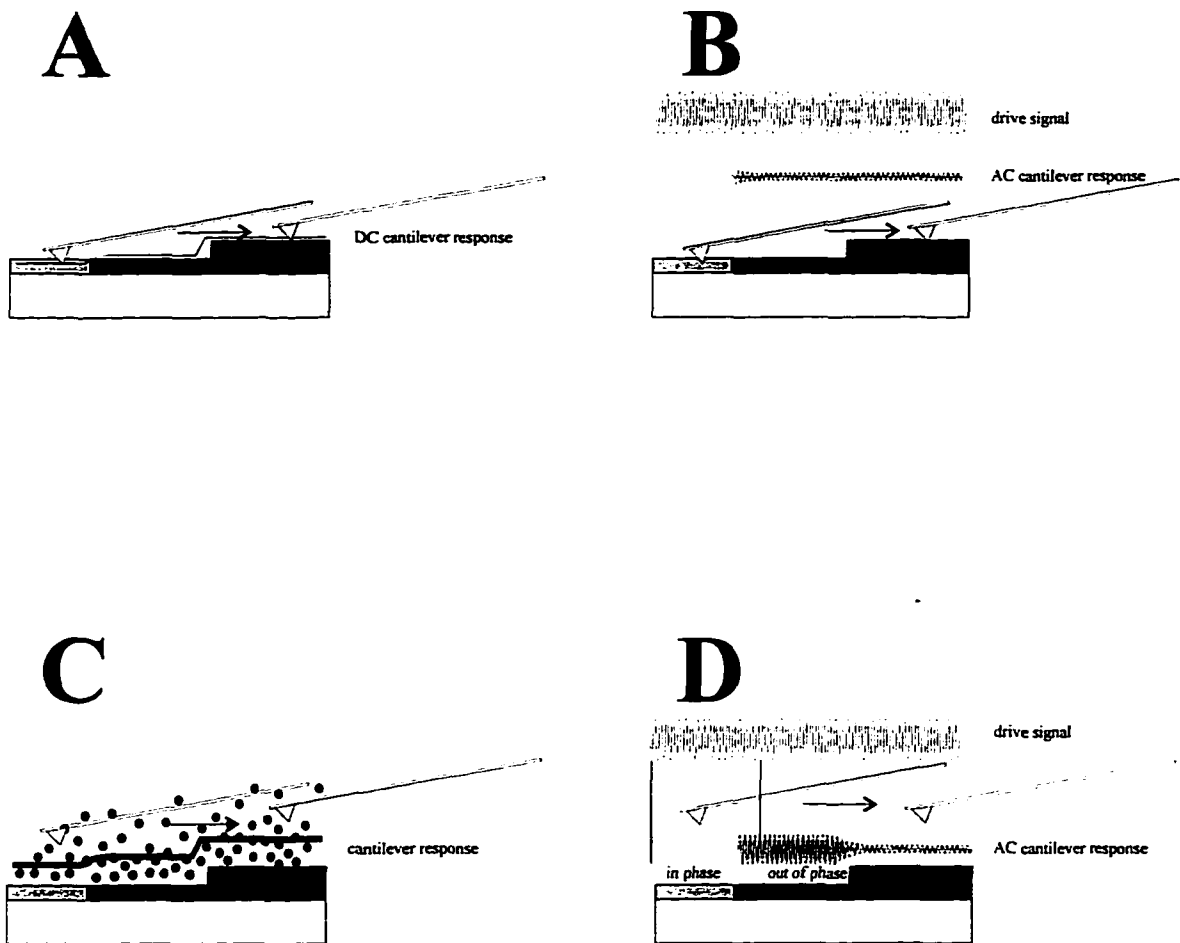
As the sample is scanned below the probe-tip, the cantilever beam bends in response to the variations in surface topography

Figure 3 Schematic of the principle components for an optical lever type AFM.

micron scale topographical images of rough diamond films could be acceptably imaged with electron beam deposited probes with a wide range of force constants.

The SFMs that operate by optical beam deflection offer access to a variety of material and interactional properties, as shown in Figure 4. In the most elementary mode of SFM operation, which is known as contact mode [5, 19] and is depicted in Figure 4A, a cantilevered tip is brought into direct physical contact with a sample. As the tip is rastered across the surface, the deflection of the tip is used to map out the topography. As with all SPM techniques, the use of a feedback loop is optional. In one case, deflection without feedback is plotted as a function of sample position, and in the other case, a feedback loop dynamically adjusts the vertical position of the sample in an effort to keep the deflection constant. Topographical information can be obtained in this way but one must recognize the possibility of artifacts that may arise from local material variations (elasticity, adhesion, friction, etc.) [20, 21, 22, 23, 24] as might be found at compositionally inhomogeneous surfaces. However, instead of being discouraged by these effects, new modes of SFM have been developed to focus on and measure these properties [25]. Elasticity, for example, may be determined from one variation of contact mode known as force modulation [26] which is depicted in Figure 4B. The vertical position of the sample is modulated while the tip is in contact with the sample, and the resulting cantilever deflection may be correlated with the elasticity of the tip-sample contact zone. This modulation can be performed over a range of frequencies [27]. In the high frequency mode a kHz, signal is passed to the piezo controlling the z-position of the sample (or probe) while the amplitude and phase of the cantilever response are monitored. If the drive frequency is sufficiently high, with respect to the raster rate, *elasticity* is the *imaged* property. The slower acquisition of elasticity usually passes a larger amplitude triangular wave to the z-position. The resulting plot of cantilever deflection signal versus sample z-position is known by many names: a deflection-distance curve, a force-distance curve, or simply a *force curve*. The elasticity of the sample is related to the slope of such a curve. For a completely rigid probe-sample combination, a 1 nm displacement of the sample would result in a 1 nm deflection of the probe, producing a slope of 1 nm/nm (1 nm tip deflection for 1 nm sample excursion). However, a non-zero elasticity of either the tip or





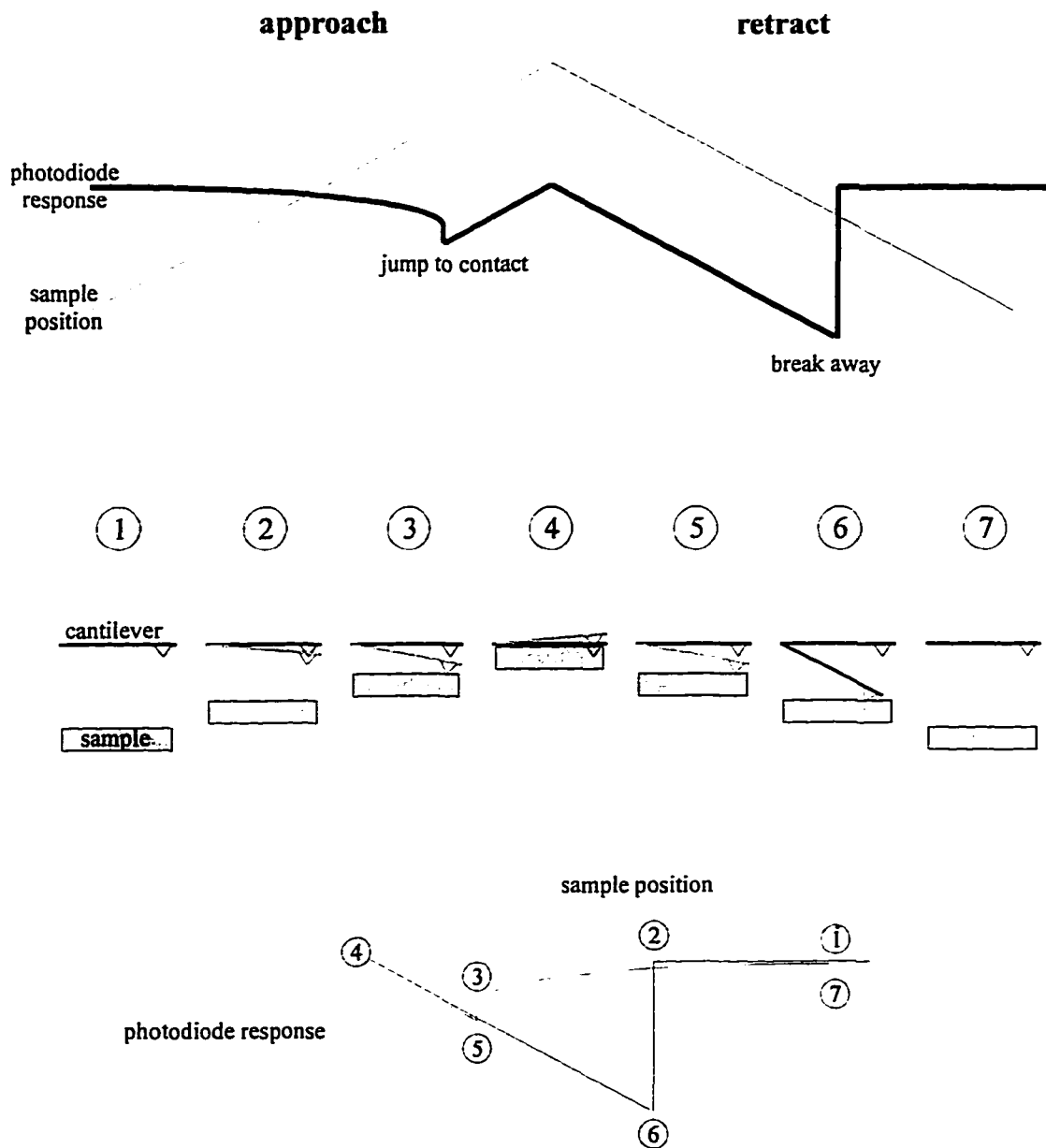
**Figure 4** Measurable properties and modes of operation for SFM: **A.** the classical contact mode measures the topography. **B.** an AC contact mode, force modulation, measures viscoelastic response of the tip-sample contact. **C.** a DC non-contact mode, has been used for initial work on imaging long range interactions (i.e., double layers). **D.** an AC non-contact mode, currently the most popular mode for imaging soft samples.

sample will cause the slope to decrease. These force curves may also be used to determine the adhesive forces actively holding the tip in contact with the sample. Since the tip is mounted at the end of a cantilever that acts as a Hooke-like spring with force constant  $k$ , the force required to separate the tip from the surface may be determined from the deflection of the cantilever as the sample and tip are separated [25, 28, 29, 30, 31, 32, 33, 34, 35] through the following relationship.

$$F = k \Delta z$$

Figure 5 outlines the major components of force curves where the interaction forces are greater than the restoring forces of the cantilever. The force curve is an approach-retract cycle, as the sample first approaches the probe and is subsequently retracted from the probe. A force curve is typically composed of the following regions:

1. First, there is a region where the probe and sample are not interacting. Here, the cantilever deflection is unaffected by movement of the sample.
2. Next, there is the region where the sample and probe are interacting through weak long range attractive or repulsive forces; these forces cause the cantilever to deflect toward or away from the sample, respectively.
3. If, at some point, the attractive forces of the sample overcome the restoring forces of the cantilever, the tip jumps into contact with the sample. Otherwise, at a certain point, the tip is pressed into the sample. In either case, the sample and probe are then usually in repulsive contact.
4. As the sample continues to approach the probe, there is a linear deflection of the cantilever, which results from the physical contact of the probe and sample, as mentioned above the slope of this line is an important measurable quantity which may be related to the elasticity of the contact.
5. The same line is traced as the sample retracts away from the probe; however, as the sample passes the point of contact, hysteresis may be observed.
6. If there is any adhesive interaction between the probe and the sample, then the probe and sample will remain in contact beyond the initial jump to contact until the probe deflection is greater than the probe sample adhesive interaction. At that



**Figure 5** Normal force measurements with SFM: force curves. 1. the probe-sample separation,  $z$ , is large and they are not interacting; 2.  $z$  is decreased and the probe and sample begin to interact, but the strength is less than the restoring force of the cantilever; 3. at this point, the interactions become greater than the cantilever restoring force, and there is an instability as the probe "jumps to contact" with the sample; 4. at this point  $z$  is decreased; 5. here  $z$  is still being decreased; 6. however, due to adhesion more force is required to break contact; at this point the cantilever force exceeds the adhesive forces and the probe and contact is broken; 7. the probe and sample are returned to the noninteracting large separation.

point, the cantilever will break away from the surface, and will no longer be affected by the movement of the sample.

Detailed discussions about the intricacies of these normal forces with SFM are covered by Burnham [25, 32]. Importantly, the slope of this contact line (3-6) can be used to calibrate the sensitivity of the voltage output of the detector to the cantilever deflection by assuming the sample and probe are noncompliant.

So far, the transduction mechanism has centered on deflections of the cantilevered tip normal to the surface; however, lateral forces are also at work and affect the tip-sample contact. In this case, as the sample is scanned perpendicular to the principal axis of the cantilever, (i.e., the x-direction), lateral forces cause the cantilever to twist about this axis. Figure 6A shows how an optical beam deflection system can detect these torsional deflections of the cantilever. These torsional displacements again result in an angular change in the cantilever, and thus in the reflected laser beam, and can be measured as lateral displacements of the laser beam at the photodiodes. The parallel plot to the force curve is the friction loop, a plot of the torsional response of the cantilever with respect to the sample excursion in the x direction. The anatomy of these friction loops is presented in Figure 6B. With the appropriate calibration these displacements can be correlated with the frictional forces at work in the contact zone [36, 37, 38, 39]. These friction loops are typically composed of the following regions:

1. As the sample scans left, the cantilever torsion reflects the laser to the right. In this region of the friction loop, the friction is *sliding* friction. (a-b)
2. As the scan direction is reversed, the cantilever rotates clockwise, and the laser beam is deflected to the left. Throughout this process, the point of contact is fixed, at the end of the previous scan, and this can be likened to *static* friction (b-e)
3. Eventually, the torsion of the cantilever exceeds the static friction at the interface in the contact zone, and the probe begins to slide to the right. (e-f)

Just as the slope of the contact portion of force curves calibrated the detector response to the deflection of the cantilever, so the slope of the static friction portion of the friction loop (b-e)

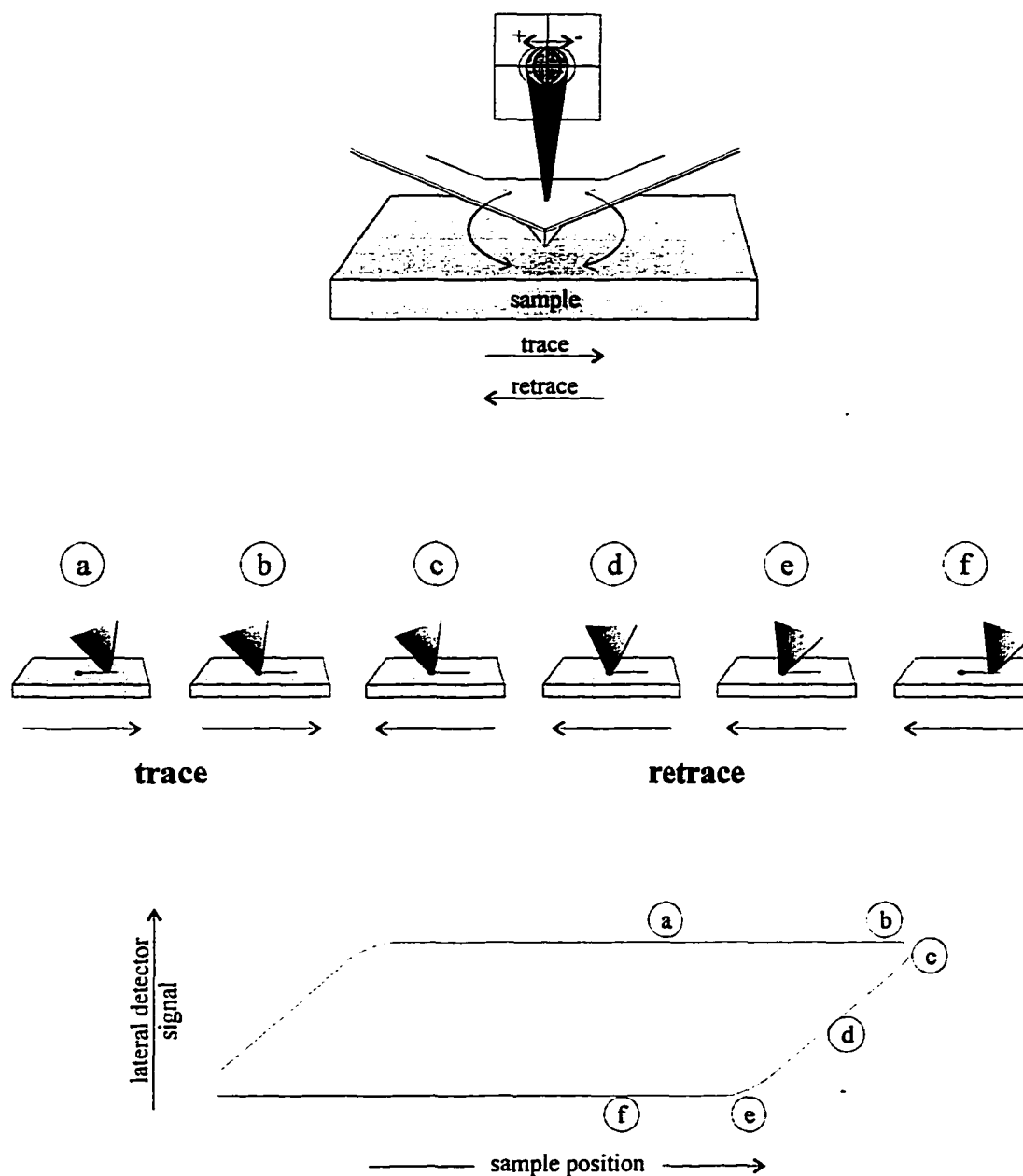


Figure 6

Lateral force measurements with SFM, friction loops. **a.** as the sample is scanned to the right the cantilever experiences a torsion that deflects the laser beam to the left; **b.** eventually the scan reaches the right limit; **c.** and the scan direction reverses, initially there is no change in the torsion of the cantilever; **d.** however, as the scan progresses to the left the cantilever rotates about a fixed tip-sample contact point; **e.** eventually cantilever restoring force (torsional) exceeds the static friction **f.** and the probe begins sliding across the surface.

calibrates the detector response to the torsion of the cantilever. Specific examples and more experimental details of both force curves and friction loops will be presented below.

Finally, force microscopy allows a host of long range forces to be probed, such as double layer forces [29, 40], van der Waals forces, electric and magnetic forces [41, 42, 43, 44] as well as other attractive and repulsive long range interaction forces [45, 46, 47]. Typically, these forces are determined by an AC technique where by the probe is oscillated near resonance, and changes in the amplitude, frequency, and phase of the oscillation are monitored as a function of probe-sample separation [19, 44]. These three measurables are influenced by the interaction force and its gradient between the probe and the sample. Access to these interactional and material properties of surfaces at these length scales offers the surface chemist unprecedented view of the surface before, during, and following modification with organic films.

### **Experimental Ranges**

One of the most versatile aspects of SFM is the ability to characterize a broad variety of samples under a wide range of environmental conditions: from the pristine conditions of ultra high vacuum to the extremely harsh environments of some electrochemical solutions, encompassing wide pH ranges. In the electrochemical environment, the SFM has the advantage of an insulating probe, which does not rely upon current for feedback. This decouples the tip from the electrochemical processes, and is a significant advantage over STM with respect to ease of use in the electrochemical in situ experiments.

### **Resolution Issues**

While STM has produced molecular *resolution* images, the corresponding studies with SFM have typically produced images with molecular *periodicity*. The distinction results from the mechanistic differences between the measurements made by the two instruments. While a single pixel of an STM image represents the current from a narrow electron tunneling filament, the corresponding data for contact SFM images is a deflection of a cantilever that may be caused by the cumulative cooperative repulsive force from tens or even hundreds of molecules [48]. The area of the contact between the probe and surface is dependent upon the

imaging force, the elasticity of the sample, and the morphology (i.e., size and shape) of the probe. Thus, to obtain atomic resolution with contact SFM, sharp tips, low forces, and relatively rigid layers are preferable [23, 24, 48, 49, 50, 51, 52, 53]. Additionally, atomic resolution has been achieved with non contact SFM [48] at Si(7x7); however, these cases are rare, and are extraordinarily difficult experimentally.

This concludes the brief introduction into SPM, and some of these topics will be described again in some detail as they become relevant in the later sections. At this point, the general introduction continues with a brief overview of spontaneously adsorbed monolayers, in particular alkyl thiolate monolayers at gold. The use of these systems is particularly prudent because not only do they form relatively rugged, well ordered, systems but they have also been thoroughly studied by a variety of techniques, as will soon become evident.

### **Spontaneously Adsorbed Monolayers**

In recent years, there has been a virtual explosion in the growth of studies that have explored the applications of spontaneously adsorbed monolayers [3]. Of those, the most well studied are formed by the chemisorption of alkyl thiols ( $X(CH_2)_nSH$ ) to gold electrodes [3]. This adsorbate-substrate combination is attractive as a route to creating interfaces that, in comparison to the compositional and morphological heterogeneity of polymer materials, have a well defined composition, thickness, and spatial arrangement. This system also offers the opportunity to tailor surface structures by changing the precursor (i.e., variation of alkyl chain length and alteration of the end group) or the composition of the assembly solution (i.e., the combination of different precursors for formation of a multi-component monolayer). From a fundamental perspective, this system has proven effective as barrier films to electron transfer and ion transport [54, 55], constituting important models for testing and extending theories of heterogeneous electron transfer and of the structure of the electrical double layer. Additionally, this barrier is crucial to the development of these films as the two dimensional templates for nanofabrication of molecular devices, the creation of molecular recognition gates [56], electroanalysis, electrocatalysis, and protein electrochemistry, and as a new route

for the fabrication of microelectrode arrays. An excellent review of these monolayers as well as other organically modified surfaces is presented in Ulman's text [3].

As with all organically modified surfaces there are effectively three regions to the monolayer film: 1) the adsorbate-substrate interface; 2) the body of the adsorbate; and 3) the adsorbate-environment interface. Figure 7 illustrates these regions for alkyl thiolate monolayers, along with some associated characterization techniques. Each of these characterization techniques interrogate slightly different aspects of each of these three regions. For example, contact angle measurements probe the surface free energy, as well as interfacial free energies with respect to different probe liquids. Contact angles have a demonstrated depth sensitivity on the order of 0.5 nm [57], and thus are primarily concerned with the structure of the terminal groups of the monolayer. While these measurements have been applied to the disorder/order studies of the body of the monolayer, infrared reflection absorption spectroscopy (IRRAS) has proven the most valuable in that arena [54]. Additionally, IRRAS has been invaluable as an orientational probe, due to a surface selection rule present when the substrate is conductive. While Raman spectroscopy offers complimentary orientational information, it accesses information about the adsorbate-substrate bonds (Au-S-C) and has been used to monitor orientational changes of these headgroup bonds as a function of electrochemical potential [58]. Optical ellipsometry has been used as a probe of film thickness, and in some cases where the thickness is known, it has been used to more accurately determine the effective dielectric constants of the film. Additional information about dielectric constants has been gleaned from some surface potential measurements, which have also provided information about both the headgroup dipole moment, and the dipole moment of the alkyl chains. XPS can provide information about all three regions of the monolayer: from the basic elemental composition of the surface, to the binding strengths of the headgroups or endgroups (in some cases), as well as information about the monolayer coverage. Electrochemical techniques such as differential capacitance, electrochemical reductive desorption of the adsorbate, cyclic voltammetric reduction/oxidation of solution bound electroactive species, and others provide information about a broad range of monolayer properties: headgroup binding strengths, chain-chain interactions, electron barrier properties, and of course



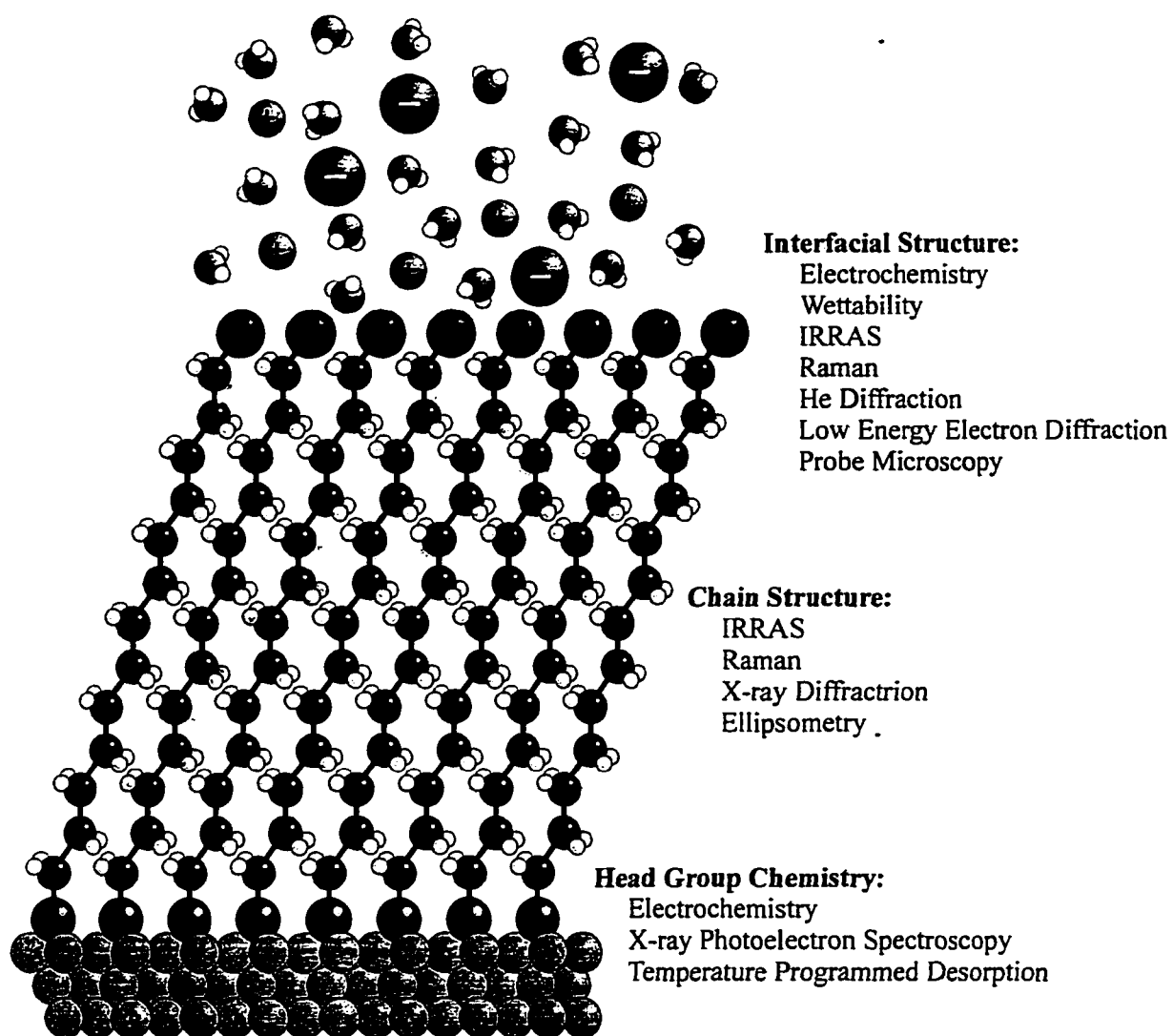


Figure 7 Idealized structure of alkyl thiolate monolayers at Au(111) along with some key characterization techniques and the properties which they probe.

coverage. Temperature programmed desorption of the adsorbate gives information about the energetics of the monolayer, and some piezoelectric mass sensor techniques have also examined the kinetics of monolayer formation.

The following is a select set of references which aptly applied these techniques to the characterization of alkyl thiolate monolayers at gold, and a summary of their key findings is included here as an aid in understanding the properties of these model films. The headgroup (Au-S-C) has been characterized by TPD [59] to have a Au-S bond strength of  $\sim 44$  kcal/mole and Raman data [58] suggest that the S-C bond is largely parallel to the Au surface. Careful characterizations with XPS [60] have concluded that the state of the sulfur in monolayers formed at our laboratory is unrelated to the precursor (thiol, disulfide, or thioether) as they all produce the corresponding gold thiolate. *Ab initio* calculations [61] produced surface-S distance of 0.1936 nm, a S-CH<sub>3</sub> distance of 0.1817 nm and the hollow-S-CH<sub>3</sub> angle of 104° is consistent with the Raman data, and the calculated force constants for the surface-S bond is consistent with the TPD bond energy. Additionally a combined XPS and electrochemical study of monolayers formed at rough and smooth gold substrates [62], found that the Au-S binding depends strongly upon the kind of binding site, and that binding to Au steps is  $\sim 6$  kcal/mole stronger than binding at the three-fold hollows of terraces. Diffraction [63, 64, 65, 66] and TEM studies have provided information about the two dimensional periodicity of the thiolate which is  $(\sqrt{3} \times \sqrt{3})R30^\circ$  with respect to the underlying Au(111). This pattern is depicted in Figure 8 and corresponds to a hexagonal pattern with thiolate nearest-neighbor spacings of 0.50 nm and thiolate next-nearest-neighbor spacings of 0.87 nm, these values lead to a coverage,  $\Gamma = 4.62 \times 10^{14}$  molecules/cm<sup>2</sup> or  $7.7 \times 10^{-10}$  moles/cm<sup>2</sup>. Additional information regarding the coverage is obtained from the amount of charge required for an electrochemical process, such as the electrochemical reductive desorption of one monolayer, assuming a one electron process this gives coverages of  $\Gamma = 8.7 \pm 0.5 \times 10^{-10}$  moles/cm<sup>2</sup>.

The thickness of monolayer has been characterized by ellipsometry [54] (0.15 nm per CH<sub>2</sub>), surface potential [67] (9.3mV per CH<sub>2</sub>), differential capacitance [54] (0.055cm<sup>2</sup>/μF per CH<sub>2</sub>), and IRRAS [54] to increase with chain length; however, interpretations of some of the

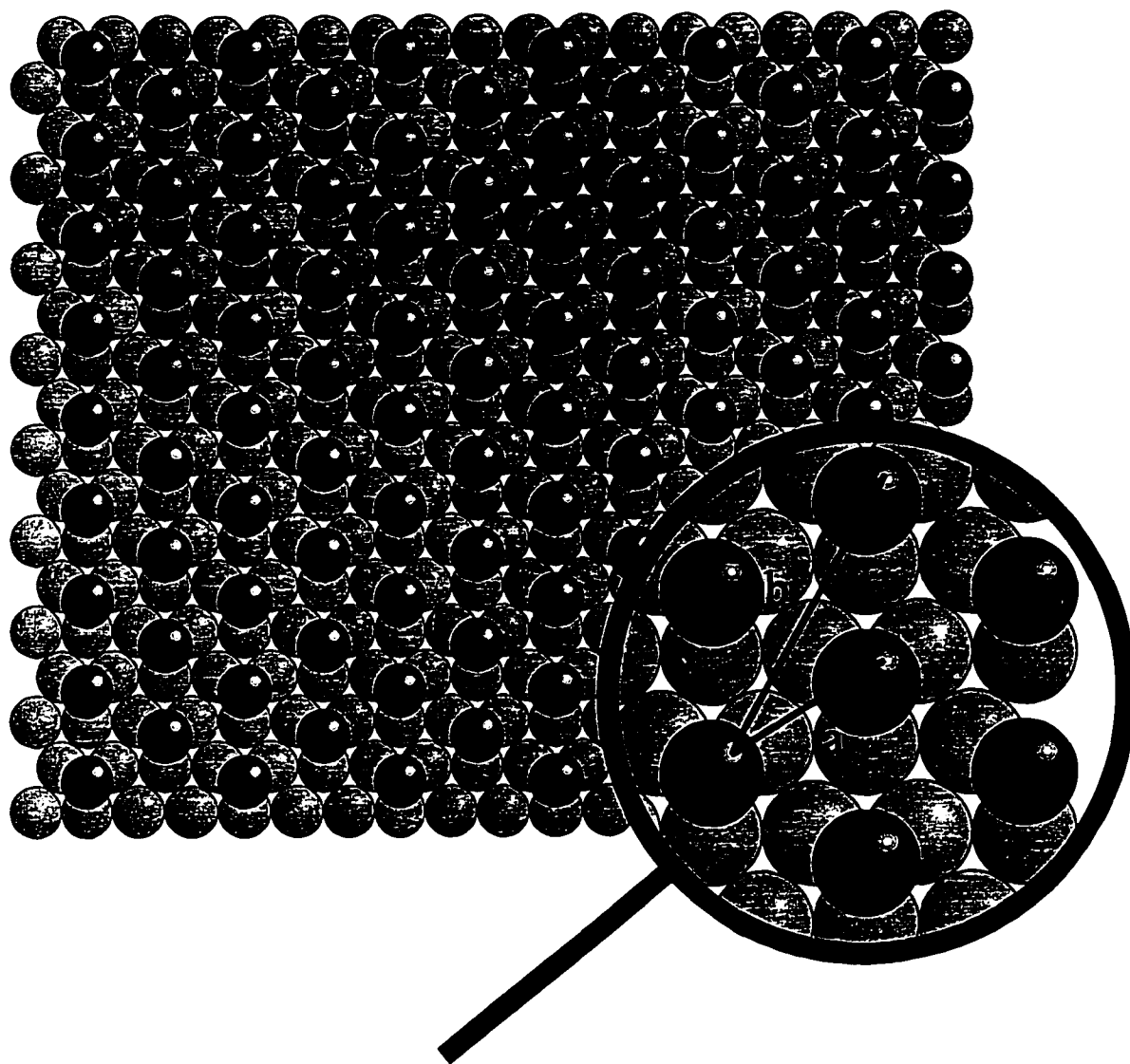


Figure 8  $\sqrt{3} \times \sqrt{3}$  adsorbate structure of the alkylthiolates at Au(111).  $a=0.50$  nm and  $b=0.87$  nm.

slopes are complicated as in the case with the ellipsometric measurements [54]. The monolayers formed from the long chainlength alkanethiols ( $H_{2n+1}C_nSH$  with  $n > 9$ ) have been shown to have a crystalline packing with all trans conformations tilted  $\sim 30^\circ$  from the surface normal and twisted axially  $\sim 45^\circ$  with IRRAS [54], and Raman [58]. Electrochemical data suggests that there is a  $\sim 0.1$ - $0.8$  kcal per mole per  $CH_2$  stabilization energy from the chain-chain interactions. Additionally, these monolayers form well packed barriers to electron transport and ion penetration [54]. Monolayers formed from shorter chain length molecules tend to be more liquid-like, according to Raman data [58] containing more gauche kinks, and IRRAS data [54] having more methylene C-H stretching peak positions characteristic of being in a liquid-like environment. These more disordered monolayers have also been shown to be less effective as barriers to electron transport, and are permeable to some ions [54].

The properties of the terminal groups of these monolayers has been probed by contact angle measurements, which determined that the free energy of the surface is effectively that of the outermost few angstroms of the monolayer [57]. Thus, the terminal group of the monolayer precursor effectively defines the free energy of the resulting monolayer. Additional studies of the order of the outermost groups have been studied by He diffraction [64-65], and IRRAS [54]. The conclusions of an IRRAS study of  $-CH_3$  terminated monolayers were that even at room temperature the  $-CH_3$  groups were sufficiently well oriented to observe that the orientation depended upon the number of  $CH_2$  groups, for odd numbers the  $-CH_3$  group pointed perpendicular to the surface, and for even number  $CH_2$  groups the  $-CH_3$  group pointed more parallel to the surface. In fact some diffraction results [64] suggest that there is a superstructure of the  $-CH_3$  groups at the outer interface.

The advent of STM and its derivatives; however, have opened the door for exploring issues related to the two-dimensional arrangement, domain size, formation mechanism, and presence and location of structural defects at the molecular level. The most common monolayers are formed from alkanethiolates at Au(111), and the two dimensional arrangement has been determined by diffraction techniques as well as SPM to be consistent with that shown in Figure 8. The projects summarized herein detail efforts to elucidate the structure and dynamics of these monolayers, the exploitation of these model interfaces for the

development and refinement of SPM techniques for expanded applicability, and information content applied to other more complex real-world systems.

### **Dissertation Organization**

As noted above, there are four primary components to this dissertation: 1) the use of SPM to develop insights into the counterintuitive correlations between surface roughness and heterogeneous electron transfer for alkyl thiolate monolayers at gold; 2) the development of a more quantitative understanding of chemical effects in frictional measurements with SPM; 3) the development of a more quantitative understanding of how frictional measurements are affected by the material properties of the interface; and 4) the application of SPM to follow the progress of electrochemical reactions. Accordingly, this dissertation is divided into four sections and each section describes in detail the procedures, results and conclusions from each of these four components. Although papers have been published for two of these sections and papers are planned to be submitted for the other two parts, the amount of information suitable for this dissertation is beyond the scope allowed for the format of those papers. So while the general topics of these sections are consistent with the papers, the content is sufficiently different to merit this format.

## STRUCTURAL CHARACTERIZATIONS

Scanning probe microscopy has produced a clearer understanding of the structure of interfaces in general, and of alkyl thiolate monolayers at Au(111) more specifically. Since SPM offers a clear view of the structure of these films, surface scientists can directly address some of the fundamental questions related, for example, to spatial orientation, coverage, and defect density. Additionally, with in situ electrochemical SPM, electrochemical effects on the structure, and structural effects on electrochemistry can begin to be delineated. It is with the utilization of this structural information that this section is concerned. Following a short literature review of structural investigations of alkyl thiolate monolayers with SPM, a study is presented which focuses on how the structure of the monolayer and the substrate affect the heterogeneous electron transfer across the monolayer. However, before the details of this study are discussed, a review of studies that have focused on the use of SPM for structural characterizations of alkyl thiolate monolayers is presented.

### SPM of Alkyl Thiolate Monolayers at Au(111)

The early efforts aimed at characterizing this adsorbate-substrate system with SPM focused on both the molecular scale and meso-scale (10 nm-100 nm) structure. In the case of molecular scale images, helium diffraction and transmission electron microscopic precedents revealed that the structure of these layers existed predominately as a  $(\sqrt{3}\times\sqrt{3})R30^\circ$  adlayer superimposed on the surface of a Au(111) single crystal. Figure 8 depicts this two-dimensional arrangement, with respective nearest-neighbor and next-nearest-neighbor spacings of 0.50 nm and 0.87 nm. The arrangement shown places the sulfur head group in the three-fold hollows of the Au(111) lattice. Although, there is no direct experimental evidence for the binding site location, it is supported by the general preference of adsorbates similar to sulfur favoring surface sites with high coordination, and by results of some recent molecular dynamics simulations [61].

Images obtained using STM consistent with this general depiction are shown in Figure 9 for layers from long ( $n=17$ ), intermediate ( $n=9$ ), and short ( $n=2$ ) chain lengths. In each case, the 10 nm x 10 nm images exhibit the hexagonal periodicity and spacing expected for a  $(\sqrt{3} \times \sqrt{3})$  adlayer, demonstrating the ability to probe the two-dimensional arrangement of these layers using STM. An image of uncoated Au(111) is included for comparison purposes.

In addition to revealing the adsorbate spacing, STM has also been applied to assess the larger scale topographies of the surface. These studies are motivated by the need to probe the long range morphology of these systems to deduce correlations between the adlayer structure and their effectiveness as barriers to heterogeneous electron transfer. Examples of such images are shown in Figure 10. These images exhibit a large number of apparent depressions embedded on the relatively flat surface of the underlying Au(111) substrate. The depressions are not observed at uncoated gold or after exposure to the solvents used for sample preparation (e.g., ethanol and hexadecane), indicating that the depressions are a direct consequence of the formation of the adlayer structure.

### Molecular Scale Structure

As noted previously, the early STM investigations of alkanethiolate monolayers characterized the structures formed at gold from methyl-terminated systems ( $n = 1, 17$ ) at a nanostructural level. These images revealed a hexagonal adsorbate lattice with a nearest neighbor spacing of 0.50 nm and a next-nearest neighbor spacing of 0.87 nm [68]. Importantly, these spacings are in agreement with the  $(\sqrt{3} \times \sqrt{3})R30^\circ$  structure deduced from X-ray and He diffraction experiments [69,65, 66, 70] for the same types of systems on Au(111) ( $n = 9 - 21$ ).

A subsequent study [71] investigated the structure of thiolate films at Au(111) that had been derivatized with endgroups of various average molecular diameters ( $d$ ). A goal of this effort was to determine the effect of the size of the end group on the packing density of the layer, and the interplay between the packing density preferences of the polymethylene spacer groups and the end group. The precursors included 4-aminothiophenol ( $d = 0.43$  nm),  $\{\text{Ru}(\text{bipyridine})_2(4\text{-methyl-4'-(12-mercaptododecyl)-2,2'-bipyridine})\}(\text{PF}_6)_2$  ( $d = 1.3$  nm),

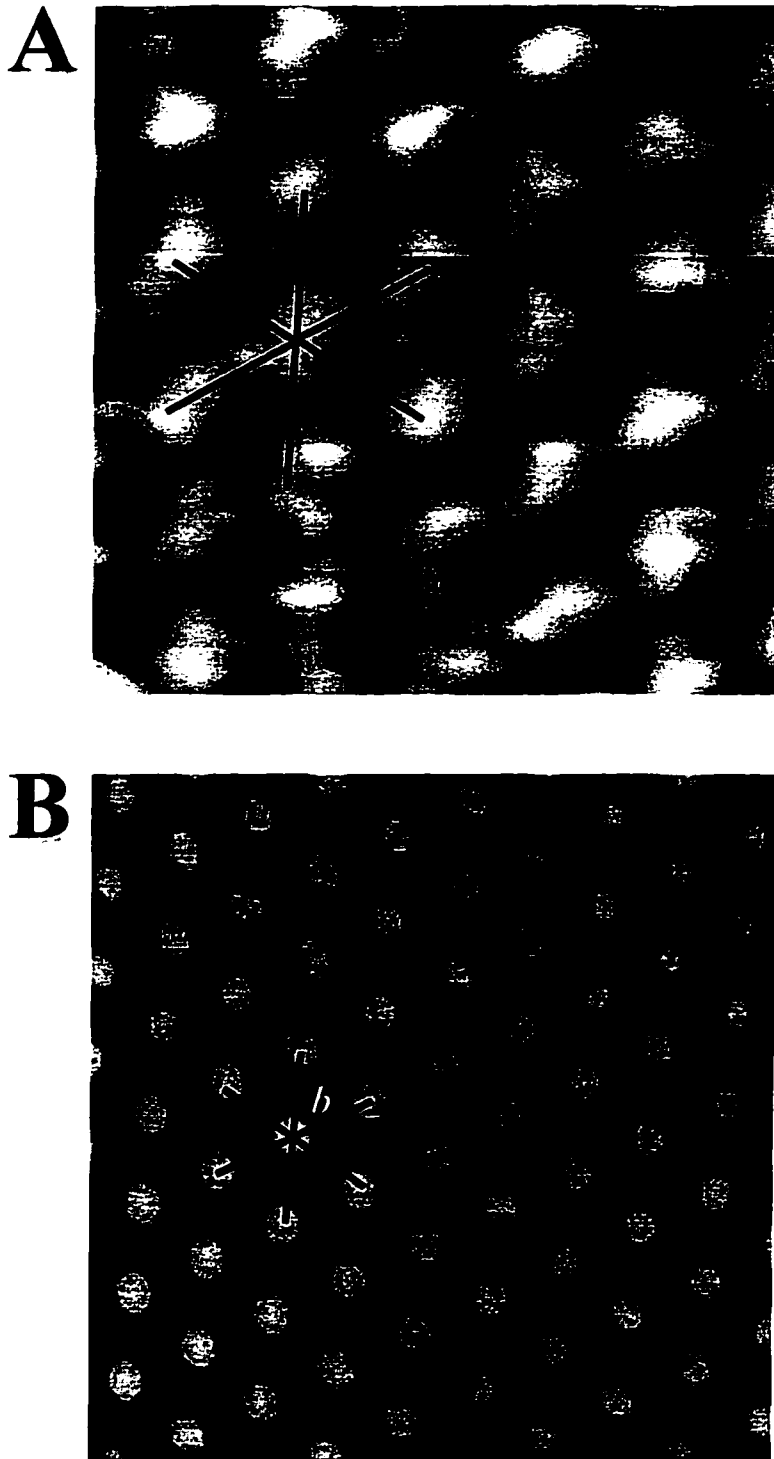


Figure 9 2.5 nm x 2.5 nm constant current STM images of **A.** ethanethiolate monolayer (mildly low pass filtered) and **B.** bare Au(111) (heavily filtered) demonstrating the ability of STM to image atomic periodicity, as well as the  $\sqrt{3} \times \sqrt{3}$  periodicity of the alkanethiolate with respect to the underlying Au(111) lattice, as represented by the fact that  $a = \sqrt{3} b$ .



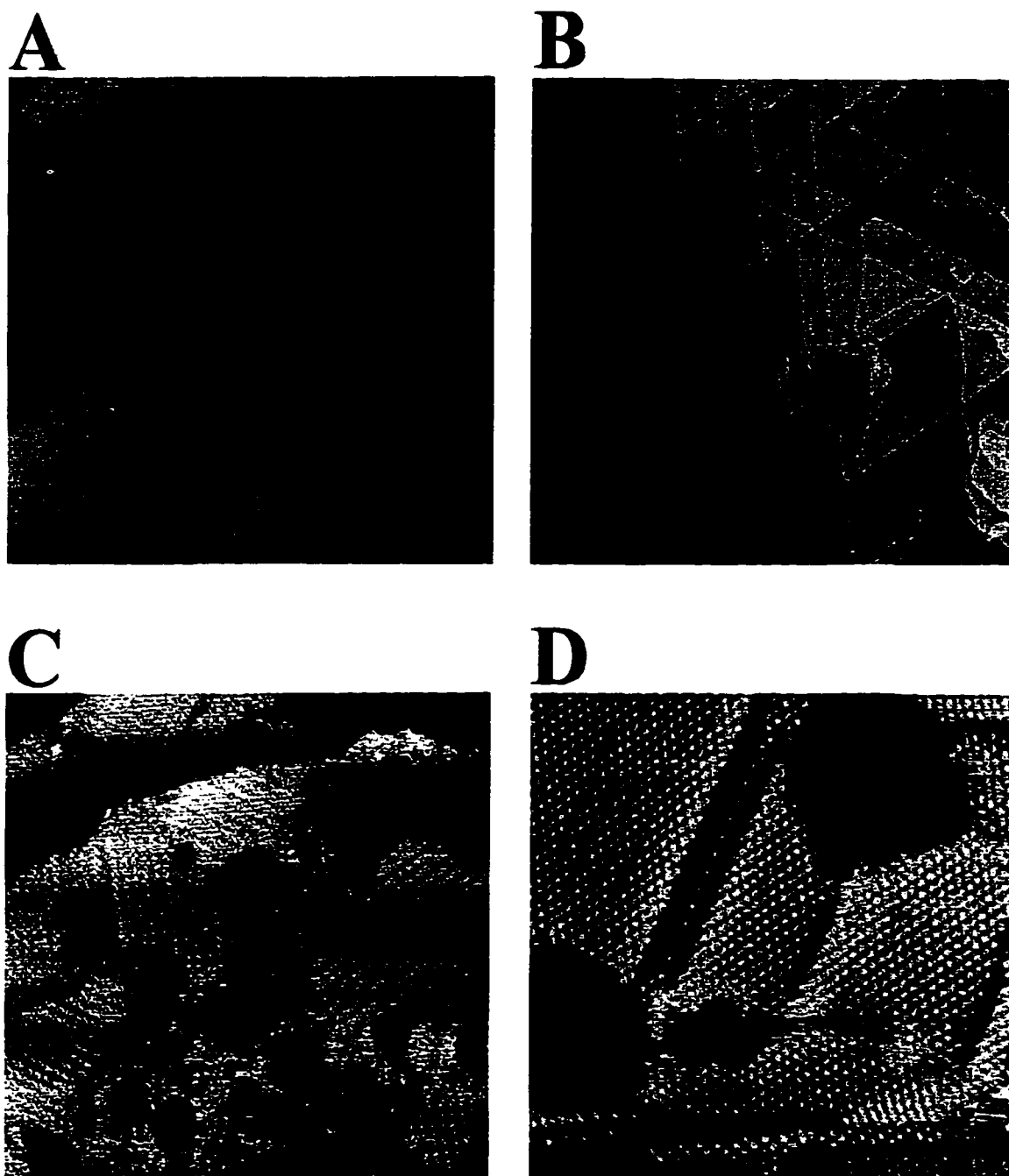


Figure 10 STM images that demonstrate the meso-scale structure of these alkyl thiolate monolayers. **A.** 195 nm x 195 nm STM image of bare Au(111) **B.** 1000 nm x 1000 nm image of an octadecanethiolate-Au(111) monolayer. **C.** 45 nm x 45 nm image of hexanethiolate-Au(111) monolayer **D.** 21 nm x 21 nm image of a decanethiolate-Au(111) monolayer. The key features include the noticeable pitting in images with thiolate monolayers (**B-D**), and structure of the monolayer within the pits (**D**), as well as the hexagonal slip planes present in the high temperature annealed Au (**B**).

(C<sub>5</sub>H<sub>5</sub>)Fe(C<sub>5</sub>H<sub>4</sub>CO<sub>2</sub>(CH<sub>2</sub>)<sub>16</sub>SH (d = 0.65 nm), and [2]staffene-3,3'-dithiol pentaamine-ruthenium(II) hexafluorophosphate (d ~ 0.7 nm). Surprisingly, a  $\sqrt{3} \times \sqrt{3}$  adlayer spacing was observed in all cases, even for precursors with endgroups too large to allow theoretically the  $\sqrt{3} \times \sqrt{3}$  packing density dictated by the polymethylene chains. Surface coverages based on the charge passed to electrolytes from the endgroups, however, indicated packing densities closer to predictions based on limitations of the sizes of the endgroups, which was significantly less than expected from the adlayer spacings in the images. Because of these discrepancies, the features assigned to the molecular structure of the adlayer in earlier STM images [71] were attributed to an adsorbate-induced perturbation in electron density of the underlying Au(111) surface. This assertion points to the importance of more advanced theoretical treatments of the imaging mechanism at these systems. Which in retrospect is quite reasonable, as the imaging conditions used were quite extreme resulting in the mechanical probe-sample scraping caused by such a low tunneling resistance ( $V\sqrt{i_t} = 300 \text{ mV} / 6 \text{ nA} = 50 \text{ M}\Omega$ ), additionally there is a high flux of electrons ( $\sim 2.5 \times 10^9 \text{ e}^-$  per thiolate per image).

More recent STM efforts have successfully imaged these systems at higher tunneling resistances. These conditions result in a larger tip-sample separation distance, which reduces the destructiveness of the imaging process [72, 73]. In imaging dodecanethiolate monolayers, it was found that high tunneling resistances ( $> 100 \text{ G}\Omega$ ) were required to avoid mechanical interactions between the tip and sample [72]. Interestingly, images of such a system at even higher tunneling resistances (i.e., 670 G $\Omega$ ) revealed the pattern of the adlayer structure, whereas those at lower tunneling resistances (e.g., 33 G $\Omega$ ) exhibited the pattern of the underlying gold substrate [72, 74]. The likelihood of tip interactions with the adlayer structure is also supported by a study of the layer formed at Au(111) from mercaptohexadecanol [75]. In this case, force gradient measurements indicated that low tunneling resistances (0.1 - 1 G $\Omega$ ) resulted in an elastic compression of the chain structure [75].

Recent studies have also detected the movement of features associated with the adlayer structure which have also been correlated to imaging effects [71, 72, 74, 75]. As a consequence, the most recent efforts have employed large tunneling resistances to minimize

the possibility of tip-induced effects [76, 77, 78, 79, 80, 81]. In imaging at high tunneling resistances, a variety of new molecular structures, in addition to the  $\sqrt{3} \times \sqrt{3}$  adlayer, have been detected. As shown for a dodecanethiolate/Au(111) sample, "missing row" structures have also been observed [74, 80]. Within each row, the adlayer exhibits a  $\sqrt{3}$ -nearest neighbor separation distance; however, the voids between rows are consistent with the adlayer. A detailed examination of such samples concluded that the most common missing row structure is comprised of a missing row alternating regularly with four rows of chemisorbed molecules in a  $5\sqrt{3} \times \sqrt{3}$  adlayer arrangement [80].

Characterizations of monolayers from various alkanethiols ( $n = 4, 6, 8, 10, 12$ ) have also found a fundamentally different adlayer structure not observed in previous STM experiments. This structure is a repeating rectangular unit mesh containing four thiolate moieties with a  $3a \times 2\sqrt{3}a$  nearest neighbor spacing, where  $a$  equals the 0.29 nm interatomic spacing of Au(111) [76, 78]. This structure, described as a  $c(4 \times 2)$  superlattice with respect to the hexagonal thiolate lattice, was previously observed in helium and X-ray diffraction experiments [64, 82]. Similar types of structures were also suggested by low temperature infrared reflection spectroscopic studies and in low energy electron diffraction experiments [83, 84]. Structurally, the superlattice reflects a twisting of the polymethylene chains about their molecular axes, a situation speculated to give rise to the height variations observed in images obtained in a constant current mode [64, 76, 78]. An alternative suggestion is a variation in the hybridization on the S-C bond.

In addition to the superlattice structure, several other structures have been observed at monolayers from short chain alkanethiols. A study characterizing the formation process at these monolayers ( $n = 4, 6$ ) showed that these samples initially exhibit regions of disorder interspersed between the depression features discussed earlier [76, 78]. The disordered regions are attributed to a two-dimensional liquid-phase monolayer. Upon annealing in vacuum, the area of ordered regions increased, the area of the disordered regions decreased, and the number of depressions decreased. The ordered regions were further characterized by lower coverage structures that have a  $p \times \sqrt{3}$  spacing, where  $p$  usually varies from 8 to 10. The association between the  $p \times \sqrt{3}$  structure and the lower packing density phase was

deduced by observing a conversion of a superlattice to  $p \times \sqrt{3}$  structure for longer chain monolayers after inducing desorption by high temperature treatments. As such, the ordering process was envisioned in which the slow desorption of short chain thiolates proceeded concurrently with the nucleation of crystalline domains [78].

As with the original STM efforts, initial studies with SFM were focused on structural characterization. The first molecular level images of alkanethiolate monolayers produced by SFM verified the  $\sqrt{3} \times \sqrt{3}$  packing [85]. And although the same periodicity had been observed at the sterically untenable monolayers listed above with STM [71], a corresponding SFM experiment [86] using perfluorinated alkyl thiolates showed packing consistent with the increased molecular dimensions, lending merit to the electronic nature of the periodicities previously observed with STM imaging under those extreme conditions [71]. Due to the lower resolution of SFM, many of the structural subtleties measured in STM are not readily apparent. For example, STM images reveal the host of complex molecular superstructures detailed above which are currently unobserved via SFM, perhaps due to a combination of the relatively small domain size of these superstructures with the moderate contact area of the SFM tip. Only recently have SFM images revealed the ubiquitous depressions common to thiolate monolayers [87, 88], and even more recently, some of our work has produced images of these domain boundaries with SFM.

Although the SFM operates at a lower resolution, it has the strength of environmental robustness combined with increased information content. Lindsay and coworkers [89] used SFM to monitor changes in molecular periodicity at monolayer surfaces while under potential control. Beginning with the  $\sqrt{3} \times \sqrt{3}$  packing of a thiolate adlayer, the electrode was swept negatively whereupon the adlayer was desorbed and the image was replaced by the periodicity of the underlying Au(111). The value of SFM as a structural probe is clearly exemplified in this experiment which produces molecular periodicity of an organic thin film in an electrolytic solution while under potential control. While this experiment utilizes electrochemical reductive desorption for removal of thiolates from the gold substrate, Salmeron and coworkers [90] found another technique to displace the adlayer. In their procedure, the thiolates may be reversibly displaced by modulating the normal force applied by the SFM

probe. At low normal forces, the  $\sqrt{3} \times \sqrt{3}$  pattern was observed; however, use of higher forces,  $\sim 200$  nN, revealed the Au(111) periodicity, which was again replaced by the initial thiolate periodicity when the force was returned to the initial low values.

Additionally, some molecular dynamics studies have examined monolayer responses to the applied loads of various SPM probes [91, 92], and one of these models suggests that while under low applied loads the methylene chains compress via an elastic change in tilt angle. That same model predicts that more extreme pressures will actually induce structural changes in the molecular periodicity.

### **Meso-Scale Structural Investigations Including Steps, Pits and Domain Boundaries**

As evident in the many earlier images, the STM-determined morphology of alkyl thiolate/Au(111) surfaces consists of features that are attributable to the gold substrate (e.g., 0.24 nm steps between atomically smooth terraces) as well as those that do not appear at Au(111) prior to exposure to a thiol-containing solution, as shown in Figure 10. In the latter case, the features appear as 2-5 nm diameter depressions and are thus associated with the formation of the monolayer. There have been a number of STM investigations of monolayer morphology addressing the structural origins of these depressions [70, 73, 74, 75, 87, 93, 94, 95, 96, 97, 98, 99]. The principle findings of these studies elucidate whether the depressions originate as defects at the gold substrate [70, 73, 74, 75, 87, 93, 94, 95, 96, 97, 98, 99, 100, 101] or as topographic [93, 98] or electronic [70, 96, 97] perturbations within the chain structure of the alkanethiolate layer.

Some of the early characterization evidence supports that the depressions originate from single-layer-deep pits in the gold surface. Several observations support this assertion. First, depression depths were measured to be  $\sim 0.25$  nm, a value similar to the height expected for a step on a Au(111) surface, and less than that expected for a defect in the chain structure in a monolayer [73, 74, 75, 94, 100]. Second, variations in imaging conditions (i.e., tunneling gap resistances) did not affect the measured depths as might be expected if imaging defects within the chain structure of the monolayer [73]. Third, depressions have been observed to move

across a terrace to a step edge, leaving a corrugated step edge with no discernible height difference from an adjacent, lower level terrace [73, 74, 94, 100]. Finally, these features are impervious to the under potential deposition (UPD) of Cu and unaffected by  $\text{CN}^-$  etchants [95, 100]. All of these observations are inconsistent with a model wherein the depressions reflect the existence of a defect in the chain structure in the adlayer.

Subsequent reports have offered conclusive molecular-scale evidence for placement of the depressions at the gold surface. In these studies, the  $\sqrt{3} \times \sqrt{3}$  adsorbate lattice periodicity, along with the other characteristic adlayer two-dimensional arrangements discussed in the next subsection, extend into the depressions. Such images show that the depressions are present even when filled with an ordered adsorbate layer and are therefore not as consequence of defects in the monolayer structure [87, 74].

Given the above evidence, the mechanistic pathway that leads to the formation of the depressions becomes an issue. Two possible routes have been put forth. One poses an adsorbate-induced etching of the gold substrate during layer formation, and is supported by the detection of gold via atomic absorption spectroscopy (AAS) in the deposition solutions after layer formation [74, 73]. These data show that increasing the thiol concentration, and to a lesser extent, decreasing the length of the alkyl chain, results in increased amounts of dissolved gold as expected for an adsorbate-induced etching process [74]. Support for this proposal also arises from the observed dissolution of gold in sulfide and thiocyanate solutions [102]. There are, however, some discrepancies with this model. The amount of gold detected via AAS is in many cases much lower than that expected based on a prediction from the size and densities of the depressions. This discrepancy suggests that an alternative pathway may be of greater significance. The recent observation of depressions of similar sizes and densities at monolayers prepared by a vapor deposition process with those from the conventional solution-based process also mitigates against an etching process as the major mechanism [95]. As an alternative, an adsorbate-induced reconstruction mechanism of the underlying gold surface has been offered as a parallel process for depression formation, relying on preliminary descriptions of the nucleation and growth of the adlayer. Though presently premature to

determine the relative importance of the two processes, ongoing experiments in several laboratories should provide a more clear picture of the situation [87, 95].

### **Surface Evolution**

Imaging by STM has also provided evidence for the evolution of the surface structure through detection of adsorbate movement and measurements of surface diffusion rates [103]. In these cases, movement of the depression features was followed by raising the temperature of a sample after removal of the sample from the incubation solution. Images showed that the depressions migrated into the steps defined by the lower, neighboring terraces [94, 100]. As a consequence, the voids in a terrace from the depressions transformed into a change in the shape of a step edge. This observation suggests that the diffusion of a depression is due either to a highly labile Au-S bond which allows the underlying gold atoms to migrate across the surface or to the diffusion of an adsorbate-substrate complex.

At high tunneling resistances where tip-sample interactions were minimized, annealing in air at approximately 100 °C resulted in an increase in depression size and a decrease in coverage from ~15% to 9% [79, 80]. These and other reports reveal that the adlayer assembles into domains ~5-15 nm in diameter [76, 77, 78, 79, 80, 81, 104]. The domains are bounded by both depressions and features associated with domain boundaries which probably result from sulfur-gold and chain tilt mismatches. Upon annealing in air, the domain boundaries arranged into a striped pattern, which may be a structural change because of thiolate desorption. Prolonged annealing resulted in the disappearance of the depressions and a decrease in the distance separating the lines, due again to the monolayer ordering to reduce strain for lower coverages [79]. Additionally, studies where the monolayer is formed at elevated temperatures yielded surfaces that displayed an increase in domain size and an alignment of domain boundaries along the next nearest neighbor direction of the adlayer lattice [76]. The increase in domain size is attributed to a decrease in the number of sulfur-gold lattice mismatches.

The consistent ability to image at the molecular scale has similarly yielded successful observations of the evolution of monolayer structure with time. An *ex situ* STM study of dodecanethiolate adlayer formation describes low density molecular structures at partial-

coverage monolayers from short immersion times or deliberate desorption [80]. A study at butanethiolate adlayers shows that the surface structure evolves from the liquid-like state discussed above [77, 81] into crystalline-like domains. Although real-time monolayer formation has yet to be observed, these studies promise to further our insight into the formation processes and structure of this important class of monolayers.

### **Barrier Properties and Structural Defects**

Because defects (e.g., pinholes, adsorbate vacancies, and conformational kinks) represent weaknesses in barrier properties, some of the early SPM explorations focused on the development of approaches for assessing structural integrity of these layers. As will be discussed shortly, one approach is to image the monolayer structure at these defects. An alternative approach, however, utilizes what we refer to as “terrain altering” techniques. Since a structural defect represents a weakness in the barrier properties of the layer, solution-based processes that involve the deposition or removal of material by reactions with the underlying gold surface can be used to decorate the location of defects. For example, a defect can be detected by creating a one-atom high terrace at gold by the underpotential deposition (UPD) of lead or copper. On the other hand, a trench can be carved into the gold surface by a substrate specific etchant like cyanide or triiodide.

One of the first uses of the above strategy explored the UPD of copper to follow the formation process as a function of immersion time [105]. In general, the extent of copper deposition diminished with incubation time. Subsequent studies have utilized a cyanide etchant to probe the size and density of structural defects [95, 100, 100]. Etching results in the presence of large triangularly shaped patterns in the sample that have a uniform spatial direction. The patterns are  $\sim 0.59$  nm deep with sides  $\sim 65$  nm in length [100]. To account for the similarity in orientation and the anisotropic shape, a point defect etching mechanism was proposed in which an adsorbate vacancy at a three-fold hollow binding site in the underlying gold substrate acted as a nucleation site for etching. Etching therefore initiates via the dissolution of three equivalent gold atoms that are exposed to attack by  $\text{CN}^-$ . By comparison, an etching process initiated at the “on-top” sites of a Au(111) substrate would yield two sets of triangularly shaped etch pits, with one rotated  $60^\circ$  with respect to the other. This analysis



therefore supports that the thiolate adlayer is bound at the three-fold hollow sites of the underlying substrate.

The same CN-etching procedure was utilized to assess the chain length dependence ( $n = 5, 11, \text{ and } 15$ ) of the relative barrier strengths of alkanethiolate monolayers formed from vapor and liquid-phase depositions [95]. Both liquid and vapor-deposited monolayers were resistant to etching, with greater resistances corresponding to the longer chain lengths. However, the layers from intermediate length precursors ( $n = 11$ ) were more resistant to etching if formed by vapor deposition, whereas those with long chains ( $n = 15$ ) were more resistant if formed by solution deposition. The difference in the barrier properties for the layers formed by the two preparations suggests that solvent may play an important role in the formation of these systems. That is, layers formed from short chain length precursors are affected by the possible incorporation of solvent, which results in a more defective structure than the vapor deposited analogs. The formation of layers from longer chain length precursors is, however, assisted by solvent by increasing the fluidity of the chain structure during formation, and yields a more effective barrier film.

Another study showed that the structural integrity of an octadecanethiolate layer could be manipulated by changes in the tunneling conditions. Both a tip-induced etching and a tip-induced deposition of material could be achieved [93], presenting an opportunity for pursuing nanolithographic patterning of these interfaces. More recent studies revealed that these layers can be easily damaged while imaging, and in fact even that the thiolates may be electrochemically removed from a predefined pattern on the gold surface.

In general, these studies have shown that as-formed monolayers from alkanethiols of intermediate to long chain lengths are fairly resistant to etchants and are thus free of defect sites large enough to permit contact between an etchant and the underlying gold surface. These data, however, do not probe the existence of smaller defects in the chain structure that preclude contact between etchant and substrate. Such possibilities, which include chain conformers and sulfur mismatches are likely to be smaller than that of an adsorbate vacancy, but still represent a weakness in the effectiveness of the layer as a barrier to electron transport. It is with this weakness to electron transport that this first study is focused.

## **Example Study (Counter-Intuitive Barrier Properties)**

As an example of how structural information about an interface can assist in a better understanding of dynamics at that interface, we investigated the possible effects that defects could have on the heterogeneous electron transfer at alkanethiolate monolayer coated gold electrodes. A particularly intriguing problem is the counter-intuitive correlation between the gold substrate roughness and the rate of heterogeneous electron transfer. We propose that an explanation for this counter-intuitive correlation originates with the distribution and size of defects present in the structure of the monolayers at the two morphologically dissimilar substrates.

The chemisorption of alkanethiolate monolayers at gold occupies a unique position in the creation of organic interfacial architectures. Of the many possibilities, the usages of this adsorbate-substrate combination as barrier films for fundamental studies of heterogeneous electron transfer processes and as platforms for the construction of recognition based chemical sensors pose particularly intriguing applications. In these and other applications, however, performance is often governed by the ability to construct interfacial structures effectively devoid of defects. For explorations of heterogeneous electron transfer processes, defects can weaken the barrier properties of the chain structure, resulting in a poorly defined separation distance between donor and acceptor. Defects can also act as nonspecific binding sites, degrading the specificity of structures designed as recognition interfaces. Though the focus of many investigations, the performance limitations presented by defects have been overcome in only a few isolated instances. The limitations caused by defects are therefore a major obstacle to advances in many of the fundamental and technological uses of this important class of interfacial materials.

### **Counter-Intuitive Response**

As a starting point for considering the development of approaches to overcome the above obstacle, intuition argues that the defects in an adlayer structure should mimic those in the underlying substrate. That is, the fewer the number of defects in the underlying substrate

(e.g., monatomic steps and dislocations), the lower the likelihood of the existence of defects in the adlayer structure, this intuitive view of the interfacial barrier properties is depicted in the idealized cartoon in Figure 11. Surprisingly, the results of attempts to take advantage of this concept for improving the barrier properties of alkanethiolate monolayers at gold are without exception contrary to such an expectation, i.e., alkanethiolates formed at rougher surfaces are much more effective as barriers to heterogeneous electron transfer than those formed at smoother surfaces. Through the investigation of the structure of these adlayers we sought to further our insight into these defect related questions.

## Experimental

Substrates were prepared by the deposition of 300 nm gold films onto freshly cleaved mica. The films were deposited in a cryogenically pumped Edwards 306A vacuum chamber at ambient temperatures at 0.3-0.4 nm/s. The gold-coated substrates were then annealed in an oven at 300°C for 4 hr. The annealed gold-coated substrates were immersed into dilute (0.5-1 mM) alkanethiol-containing ethanolic solutions, a procedure that forms a monolayer chemisorbed at gold as the corresponding thiolate [3, 106]. Ethanol was deoxygenated with high-purity argon immediately before, but not after, solution preparation. Prior to imaging, all of the samples were rinsed extensively with ethanol, and dried under a stream of argon. Ethanol (Quantum, punctilious grade), and the alkanethiols (Aldrich) were used as received.

Images were acquired in constant height mode with a Digital Instruments Nanoscope III STM that was equipped with a 0.7  $\mu\text{m}$  scanner. Tunneling currents ( $i_t$ ) ranged from 50 pA to 5 nA and sample bias voltages ( $V_b$ ) from +1000 to -200 mV. Scan rates varied depending on image size: <30 nm, ~300 nm/s; 50 nm, ~1000 nm/s, and >100 nm, ~2000 nm/s. Tips were fabricated by etching of a tungsten wire (0.010-in diameter) in 1 M KOH. After etching, the tips were rinsed with high purity water and mounted in the scanner. Although only an approximate figure of merit, a tip radius of 10-20 nm was estimated using recently described models [98, 99, 107]. Equilibration times of up to 30 min. were generally required to minimize drift. All images were acquired within 1 day of sample removal from the deposition

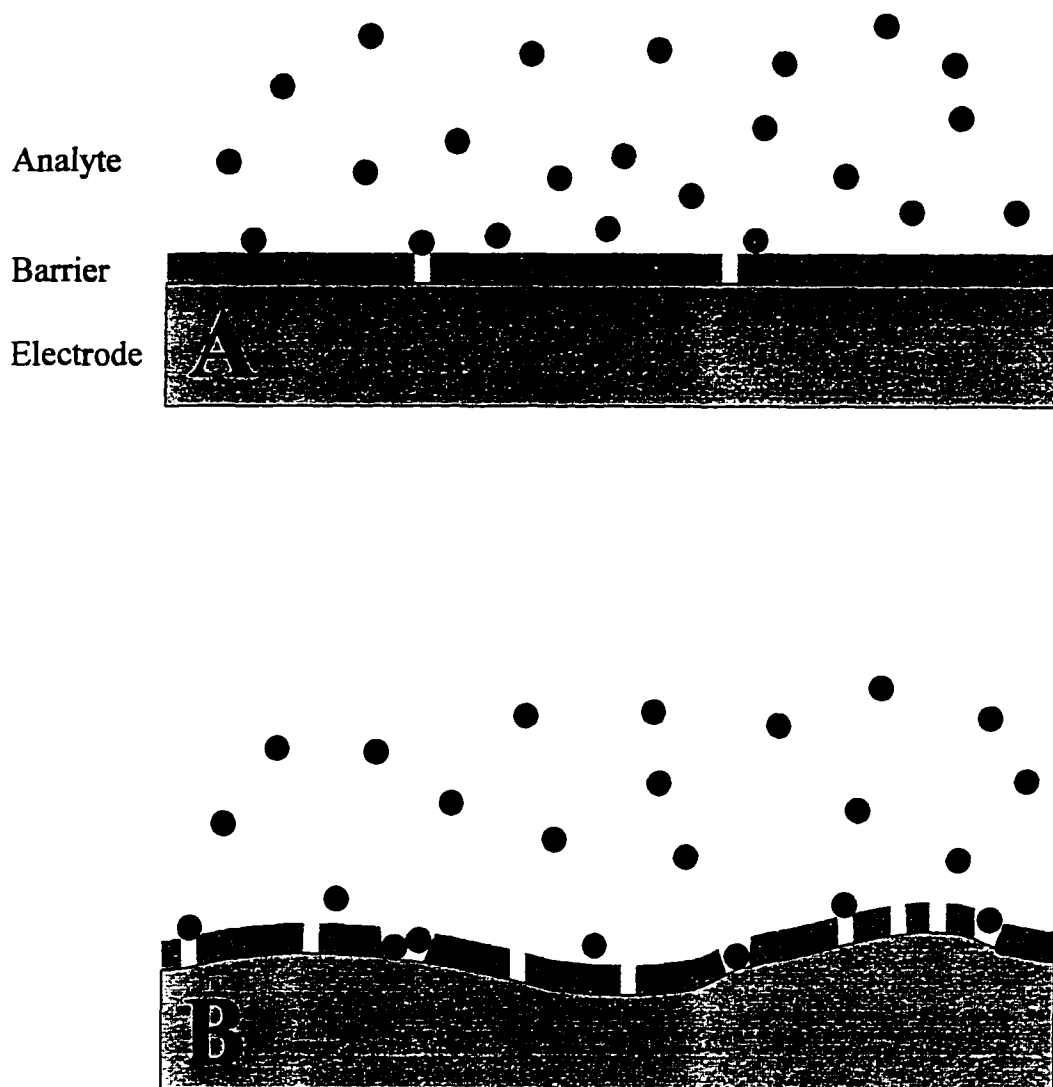


Figure 11 Intuitive view of interfacial barrier to electron transfer. The smooth substrate (A) has fewer defects than the rougher substrate (B), and is therefore less permeable.

solution. Vertical displacements of the tip were calibrated with respect to the average height of monatomic gold steps at each sample.

The experimental data presented here includes STM images for morphological characterization of the gold substrate, and cyclic voltammograms (CV) which provide a measure of electron transfer across the monolayer barrier. The two sets of CV curves and STM images in Figure 12 are representative of the above counter intuitive correlation. The data in Figure 12A were obtained for a decanethiolate (DT) monolayer formed at an unannealed gold film. In contrast, the data in Figure 12B were collected at a gold films that was annealed at 300 °C for ~4 h prior to chemisorption of a DT monolayer. In both cases, the relative strength of the resulting barrier was probed using  $\text{Fe}(\text{CN})_6^{3-/4-}$ . The CV curves at the coated samples are markedly attenuated with respect to that at uncoated gold (Figure 12, dashed curve), indicative of the general barrier capabilities of the two DT monolayers [108]. Further, the lower current flow and more irreversible shape of the CV curve at DT-coated unannealed gold are diagnostic of a more effective barrier in comparison to that at DT-coated annealed Au.

The STM images and corresponding cross-sectional profiles in Figure 12 complete the description of the counter-intuitive correlation. The images indicate that unannealed gold has a “rolling hill” topography with crystallite diameters ranging from 40 to 110 nm. In contrast, annealed gold has a much smoother, more terraced topography, with atomically smooth crystallites of diameters between 150 and 200 nm. The difference in the magnitudes and shapes of the CV curves therefore demonstrates that the monolayer at the smoother substrate is a less effective barrier to electron transfer than that at the rougher substrate. This is counter-intuitive, as the monolayer at the rougher substrate is expected to be comparatively full of defects.

## Models

How, then, to account for the counter-intuitive correlation of the results in Figure 12? We propose that the explanation rests with differences in the density and size of the defects present in the structures of the monolayers formed at the two types of substrates. The most

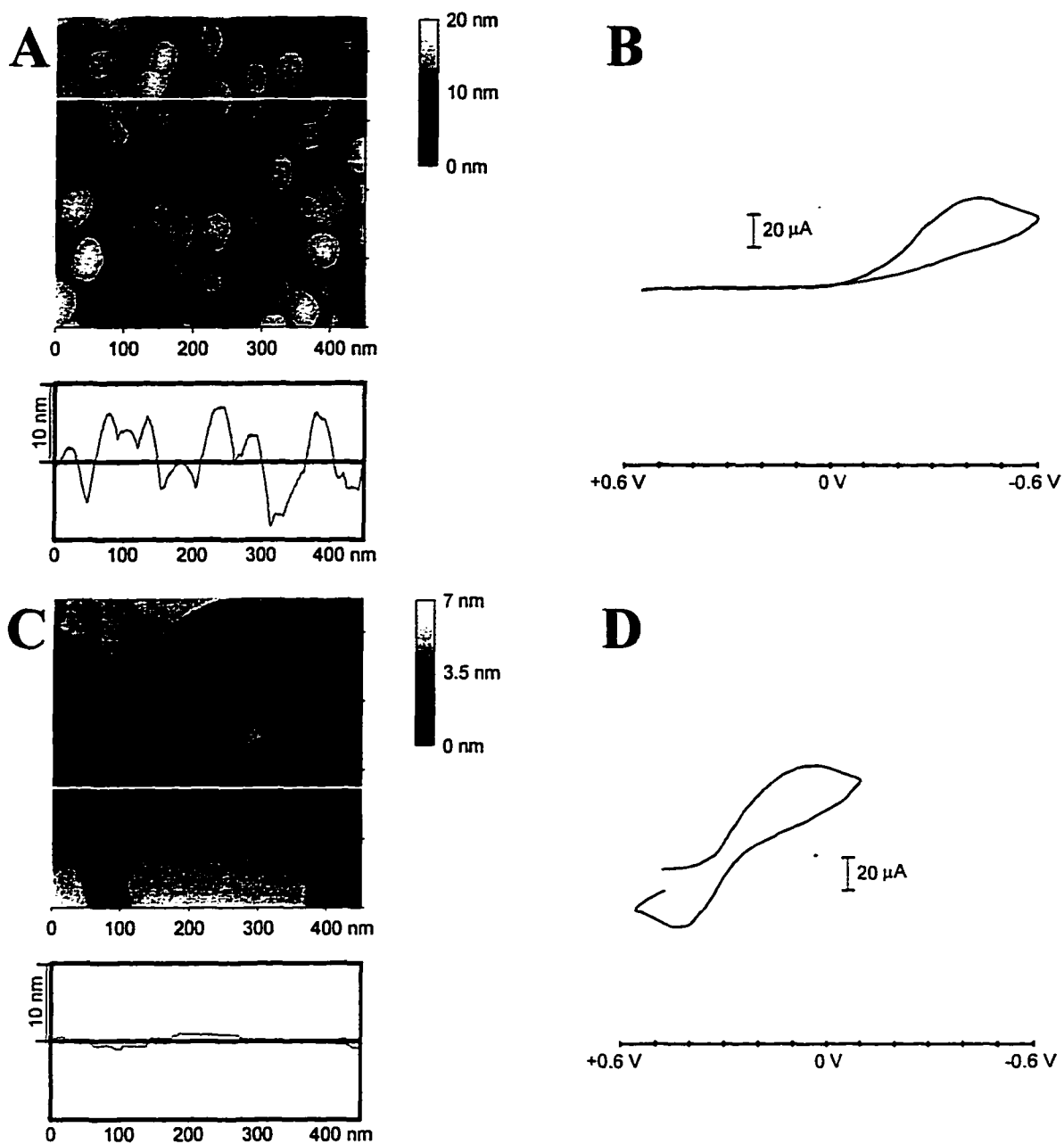


Figure 12 STM images and cyclic voltammogram of decanethiolate modified Au(111) electrodes. (A). STM of rough unannealed sample and corresponding CV (B). The respective image and CV for the annealed samples are shown in (C) and (D).

prevalent defects found at these monolayers may be grouped into three classes: (1) steps in the gold substrate, (2) single atom depressions in the gold substrate, and (3) domain boundaries in the monolayer. While, steps account for nearly all of the defects found at the rough unannealed samples, depressions and domain boundaries account for effectively all the defects at the smoother annealed samples. A comparative picture of both the densities and sizes of these defects is constructed from the combination of STM images with some simplified models. In addition to the contents of this section, the Appendix includes a comprehensive set of figures which pictorially present these models.

First, we address the density of defects at the two substrates. The amount of defects present is expected to depend upon the morphology of the substrate, as well as kinetic and thermodynamic aspects of monolayer formation. The first part of model construction is the development of the gold substrate. The smooth annealed substrates can be effectively modeled as an atomically smooth Au(111) plane, that is free of any other topography. Monolayer formation at terraces begins with random homogeneous nucleation at three-fold hollow sites of the Au(111) surface and is followed by isotropic growth away from the nuclei. This growth is terminated when neighboring domains grow together resulting in the formation of domain boundaries and depressions. Our model is limited to domain boundaries that occur along the gold nearest-neighbor and next-nearest-neighbor directions, a limitation that is supported by several images where domain boundaries predominantly occur at  $60^\circ$ , and to a lesser extent  $30^\circ$ , with respect to each other. This has the effect of more accurately modeling experimentally observed images of these domain boundaries while limiting the complexity of the model. Previous studies have shown that the thiolate monolayer within the depressions are ordered [87], thus the resulting defect is actually one-dimensional defects localized along the perimeters of the depressions. Since all of the defects are one-dimensional structures, a convenient measure of the defect density is the total length of defects per unit area,  $L_d/A$ . Following an extensive review of STM images produced by our group as well as a number published by others, we determined that terrace defects average an  $L_d/A$  of  $\sim 0.2 \text{ nm}^{-1}$ . The “rolling hills” of the unannealed surfaces as deposited in our lab have average radius of  $\sim 36.0$

nm and average heights of  $\sim 18.0$  nm. Because there are no clearly resolved images of step defects at these highly stepped surfaces we estimate their density from a model.

Intuition argues that the corresponding study of rough unannealed substrates will reveal a higher density of defects, and we expect a larger  $L_d/A$ . X-ray diffraction data verifies that the gold at these unannealed substrates is highly oriented with the Au(111) surface pointing in the direction of the surface normal. For a hill 18.0 nm high there will be 77 Au(111) steps, each with a step height of 0.236 nm, and when these steps are fit to this sphere the resulting model, shown in Figure 13A, has 1,227.5 nm of steps per 4,500 nm<sup>2</sup> of area. Notably, however, the widths of these steps are extremely narrow, as shown in Figure 13B, capable of supporting at most only a few thiulates. The above averages produce an estimated  $L_d/A$  of about 2.7 nm<sup>-1</sup>, and comparison of this value with the  $L_d/A$  value for annealed gold confirms the intuitive concept; that is, the rougher surface has more defects, about 15 times as much in length per unit area. Next, we turn to analysis of the sizes of these defects, a property which is also expected to be related to the mechanism of formation. When the thiols adsorb at the wide terraces of annealed Au(111), the adsorption sites are preferentially three-fold hollows. Once a single thiolate binds at a particular three-fold hollow, it defines a registry with respect to which other thiolates will be offset. There are six possible offsets, as seen in Figure 14. Thus, when these domains grow into one another, the resulting domain boundary will be related to the particular offset which exists between the thiolates within those two domains. With six possible sites, there will be 36 possible combinations, and if we limit our model to domain boundaries along the two primary directions, Au(nearest-neighbor) and Au(next-nearest-neighbor), then we have a total of 72 possible boundaries of which there is a vast amount of degeneracy finally resulting in 12 distinct domain boundaries, of which 2 involve merging of neighboring domains into a single domain. With simple molecular models, it is possible to represent these boundaries and compute effective exposed areas per unit defect length,  $\alpha/\lambda$ , some of these boundaries are depicted in Figure 15.

At narrow steps of the rough unannealed substrates the difference in adsorption sites leads to a dramatically different type of growth as well as to different types of defects. Since



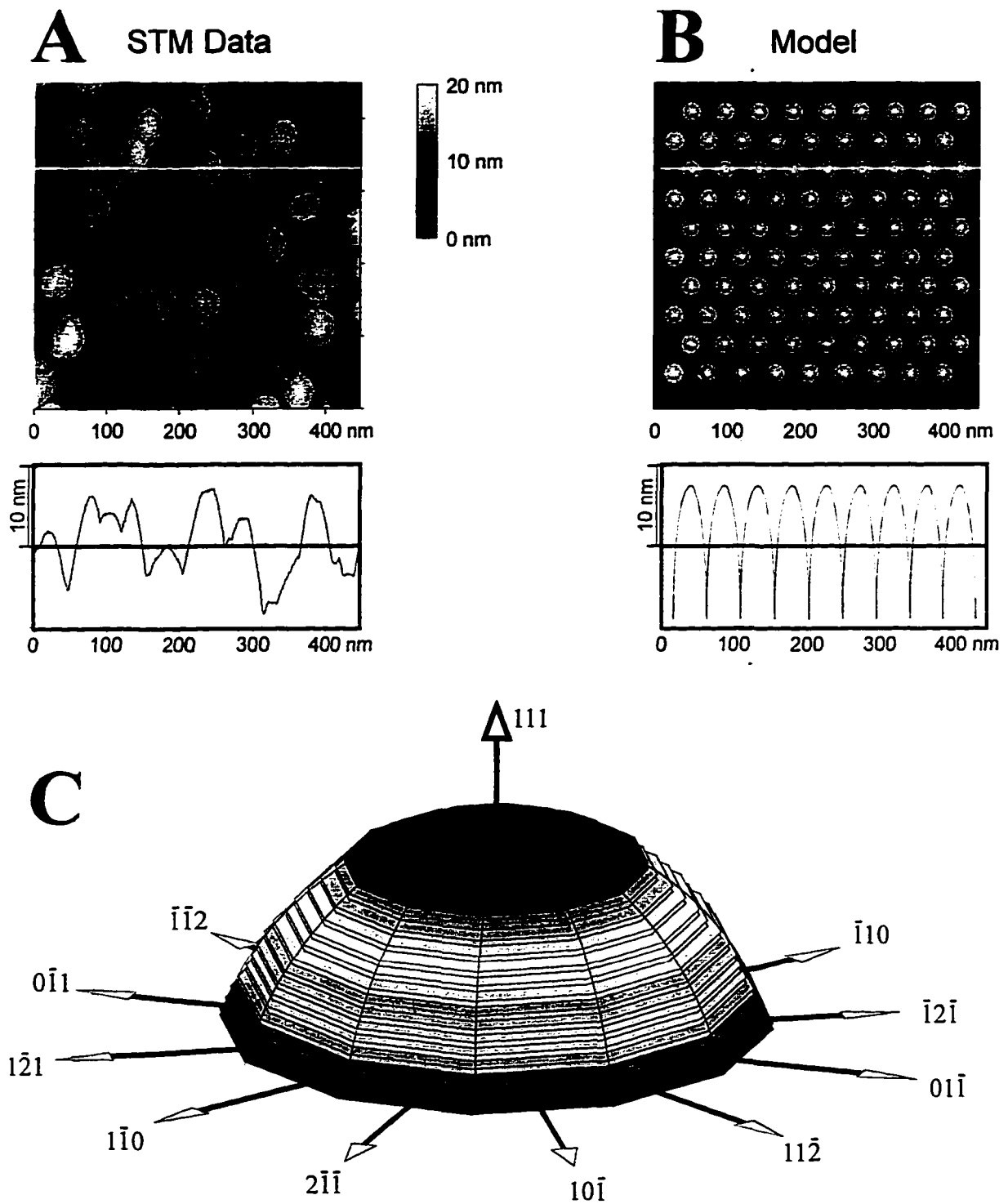
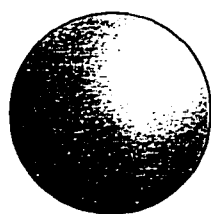
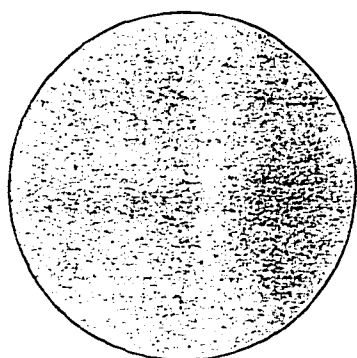


Figure 13 Model for rough unannealed Au(111): (A) an STM image of unannealed Au on mica is shown. (B) This surface is modeled with a hexagonal array of spheres. (C) The tops of these spheres are divided up according to the height of Au(111) steps.



**Gold atom**



**Alkanethiolate**

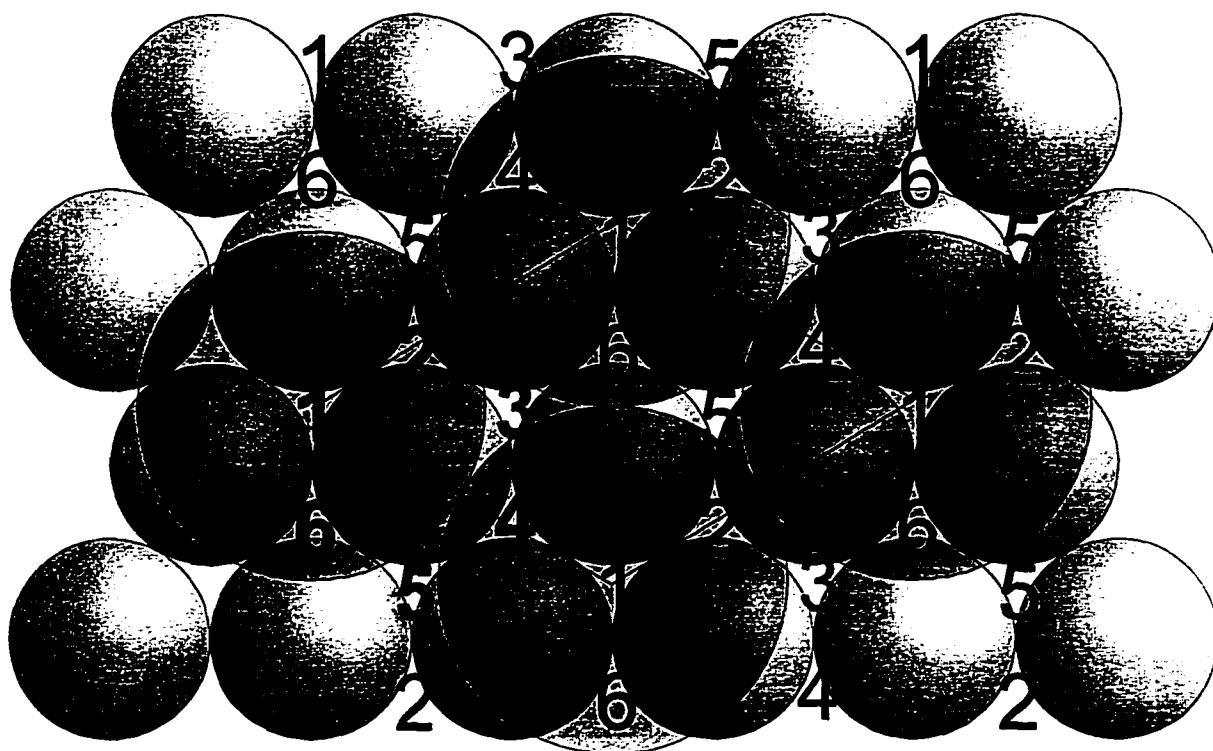
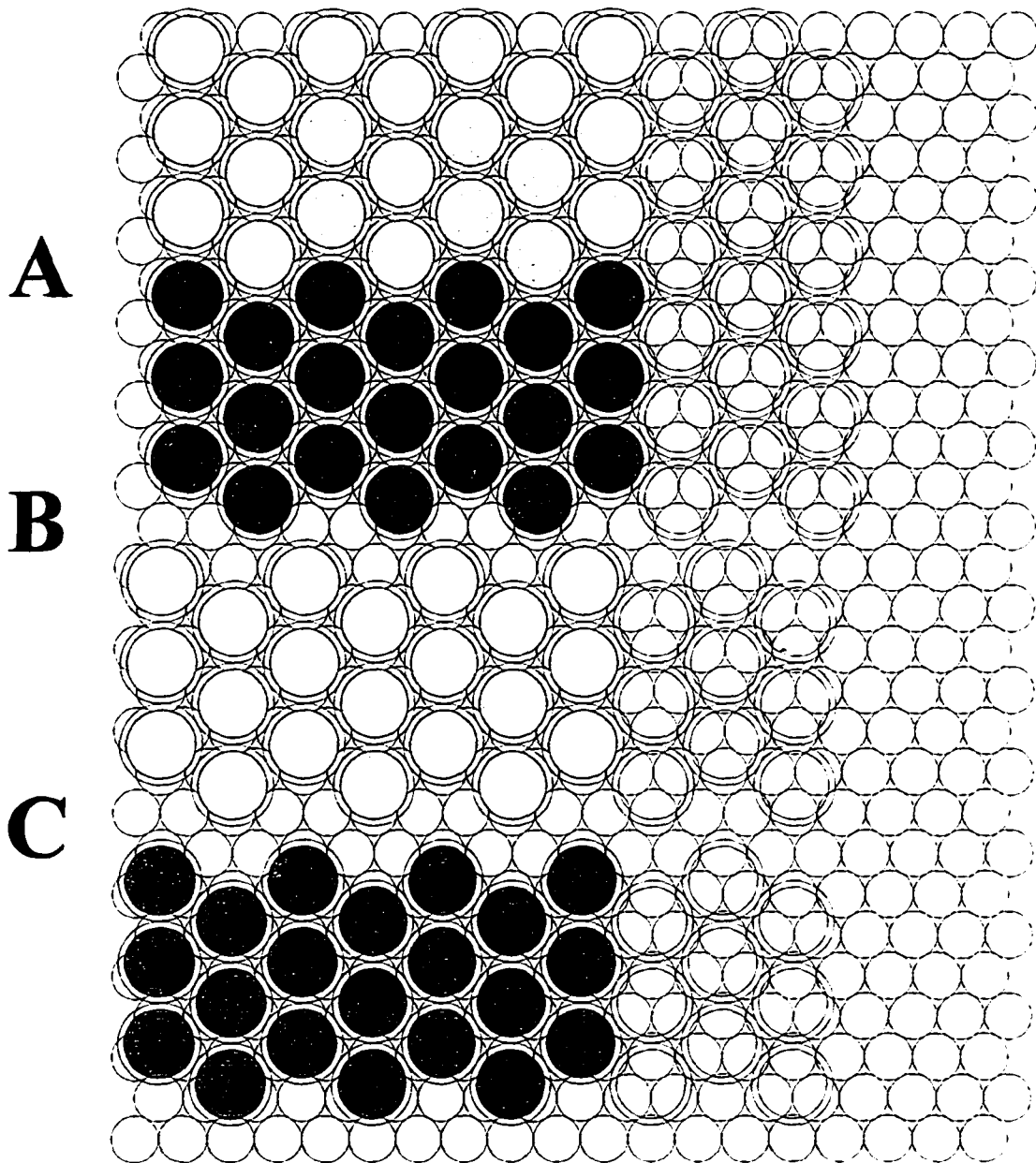


Figure 14 The six possible offsets for the 3-fold hollow adsorption sites. If a thiolate binds at one of the bold face sites, it defines a registry, those sites labeled with the non-bold-face numbers, at which other thiolates may adsorb.



**Figure 15** A. the smallest domain boundary is formed when the merging domains are in the same sites, resulting in no domain boundary 1 out of 6 times. B. a medium sized domain boundary, which is also the most common type of domain boundary happening 1 out of 3 times. C. the largest domain boundary occurs 1 out of 12 times.

the thiolates form preferentially at the highly coordinated step sites, and since most of the narrow steps can support only a few thiolates per step, the type of packing is no longer driven by the three-fold hollows of the terraces, and some are presented in Figure 16. The resulting types of boundaries may be analyzed in a similar manner to produce the exposed area per unit defect length. Another important parameter is the fractional occurrence of a defect,  $p_i$ , which, in the case of steps, is the fraction of all steps that are type I.

The fractional occurrence,  $p_i$ , exposed area per unit defect length,  $\alpha_i/\lambda$ , and the total length of defects per unit area,  $L_d/A$ , can be combined to produce the fraction of the surface which is exposed by a particular type of defect,  $f_i$ , thus the fractional surface exposed by defect type  $i$  is  $f_i = p_i \times \alpha_i/\lambda \times L_d/A$ . A histogram of  $f_i$  as a function of  $\alpha_i/\lambda$ , Figure 17, is useful in that it graphically illustrates that while the smooth surface has fewer defects the defects are larger. Examination of the cumulative fractional area exposed by defects larger than a given defect area, seen as the integral of the histogram in Figure 17, shows that the defects at rough unannealed gold are below about  $25 \text{ nm}^{-1}$  while about half of the exposed area at annealed surfaces occurs at defects with exposed areas greater than  $25 \text{ nm}^{-1}$ . We conclude that these larger defects present at the smooth annealed surfaces lead to an increased electron transfer and generally poor electron barrier properties. As a test of the viability of our models, we have begun a detailed examination of the packing arrangements at the domain boundaries detected in the recent scanning tunneling microscopic images reported by our [87] and other [72] laboratories. Though our examination of such images is not yet complete, the example presented in Figure 18 is supportive of the types of domains predicted by our models. The STM image in Figure 18 shows a domain boundary for a

decanethiolate monolayer on a large sized gold terrace. The structure of the boundary at the terrace is Type 65 (see Appendix for nomenclature), an average probability domain which should occur about one out of every twelve times it has an exposed area per unit defect length that is  $19 \text{ nm}^{-1}$ . These results support the general viability of the domain structures predicted by our models.

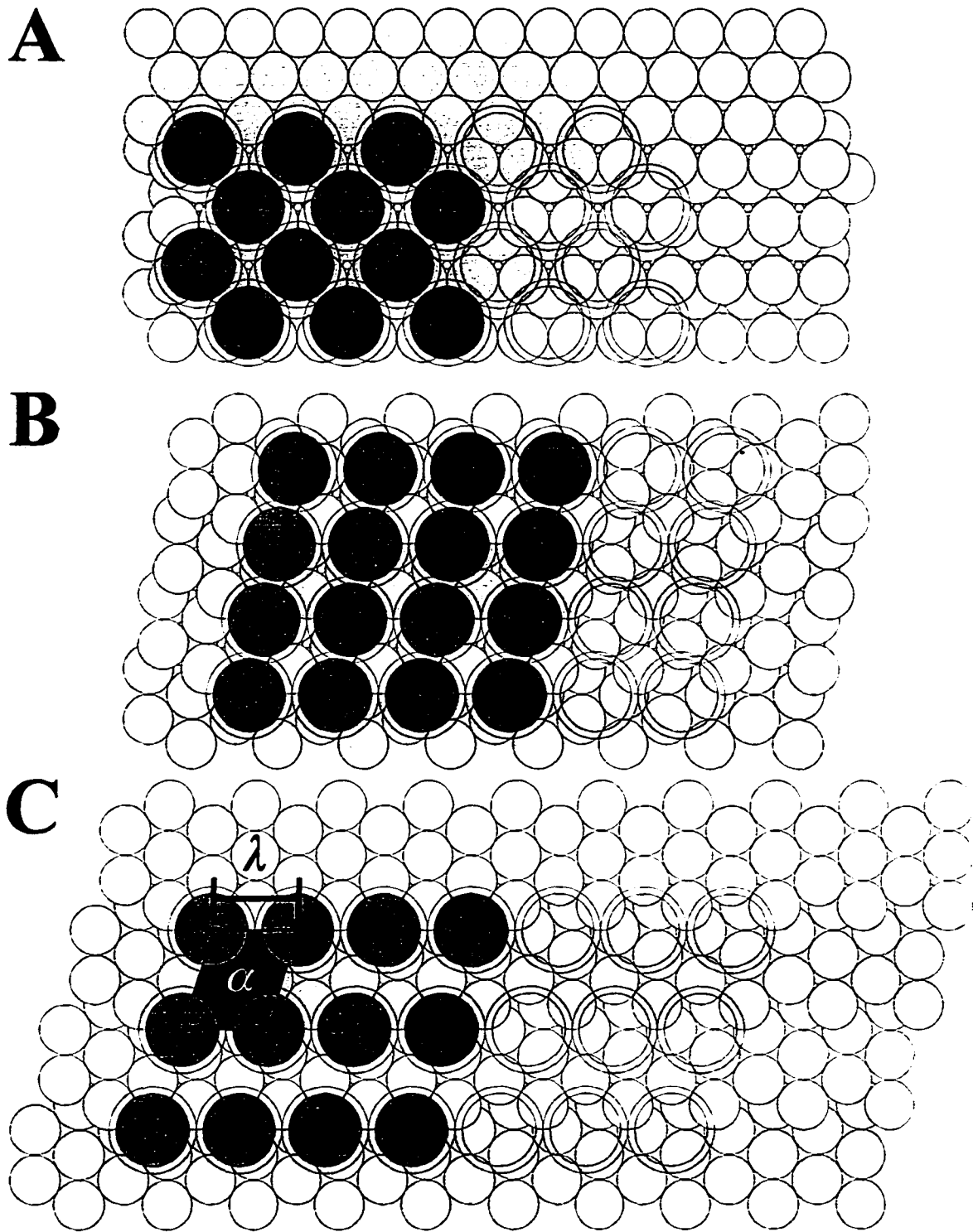


Figure 16    **A.** the smallest of the considered step defects, formed at the second narrowest of the 111 steps.    **B.** an average step defect, formed at the third narrowest of the 110 steps.    **C.** the largest of the considered step defects, formed at a the the widest of the 110 steps considered.

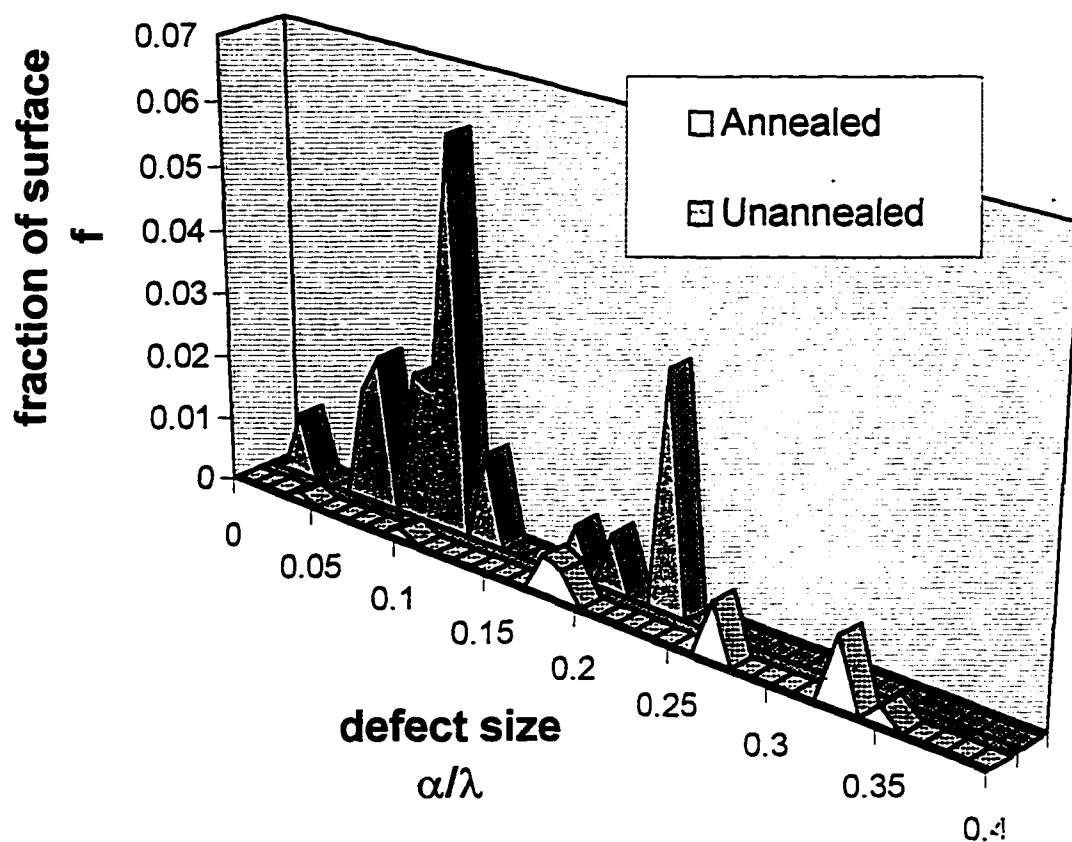


Figure 17

The fractional area exposed by defects as a function of their defect size. Clearly there is more area exposed at the more defective rough unannealed surfaces; however, we suggest that the enhanced electron transfer occurs across the larger defects found only at the smoother annealed surfaces. This plot assumes thiolates pack as hard spheres with 0.50 nm diameters.

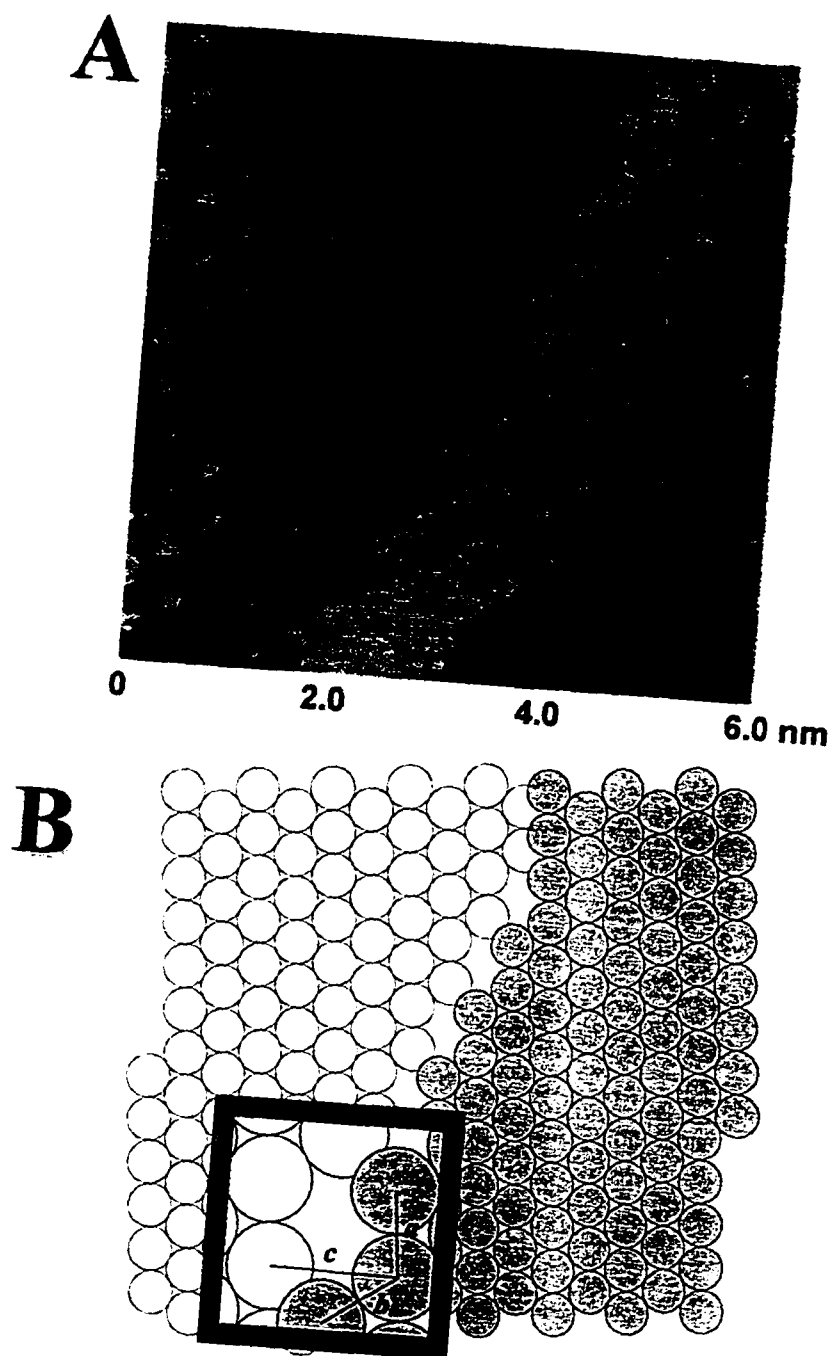


Figure 18 (A) STM image of a domain boundary found at a decanethiolate monolayer. (B) This can be reasonably well approximated by a domain boundary type 3 perpendicular to the Au(NNN) direction (this is further detailed in Figure 45).

## Conclusions

Taken together, the results of our model analysis argue that the counter-intuitive correlation between the effectiveness of alkanethiolate monolayers as barrier films at smooth and rough gold surfaces is in fact a direct consequence of the density and size of defects at the two topographically distinct surfaces. Importantly, it is the difference in growth that results in domain boundaries with larger void volumes at the smoother surfaces. This is not to say that the monolayers at the smoother surfaces have more defects, but rather the void volumes at the smoother surfaces are inherently larger than those at the rougher surfaces, as depicted in Figure 19. Efforts in our laboratory are underway to refine further the details of our model through the inclusion of chain tilts and to assess the structural ordering of the chains in proximity to the boundaries. Perhaps the more interesting and significant issue to be probed is how applicable is such a model is to observations at interfaces used for catalysis and other purposes. Without the resolution gained by STM, these kinds of analysis would not be possible, and empirical techniques would need to push forward with only intuition as a guide.

## Conclusions

The conclusion of this section is that the structural information obtained from SPM technologies offers a valuable insight into interfacial phenomena which is unavailable with other techniques. None-the-less, as with so many tools interpretation is a key aspect to proper application. This demonstrates how a combined approach of STM and electrochemistry can be used to gain insight into an obstacle to technological development. Indeed, if we are to create molecular recognition gates or other molecular devices, an understanding and control of defects at surfaces such as these will be critical, and these model organic interfaces offer an excellent proving ground for these techniques.



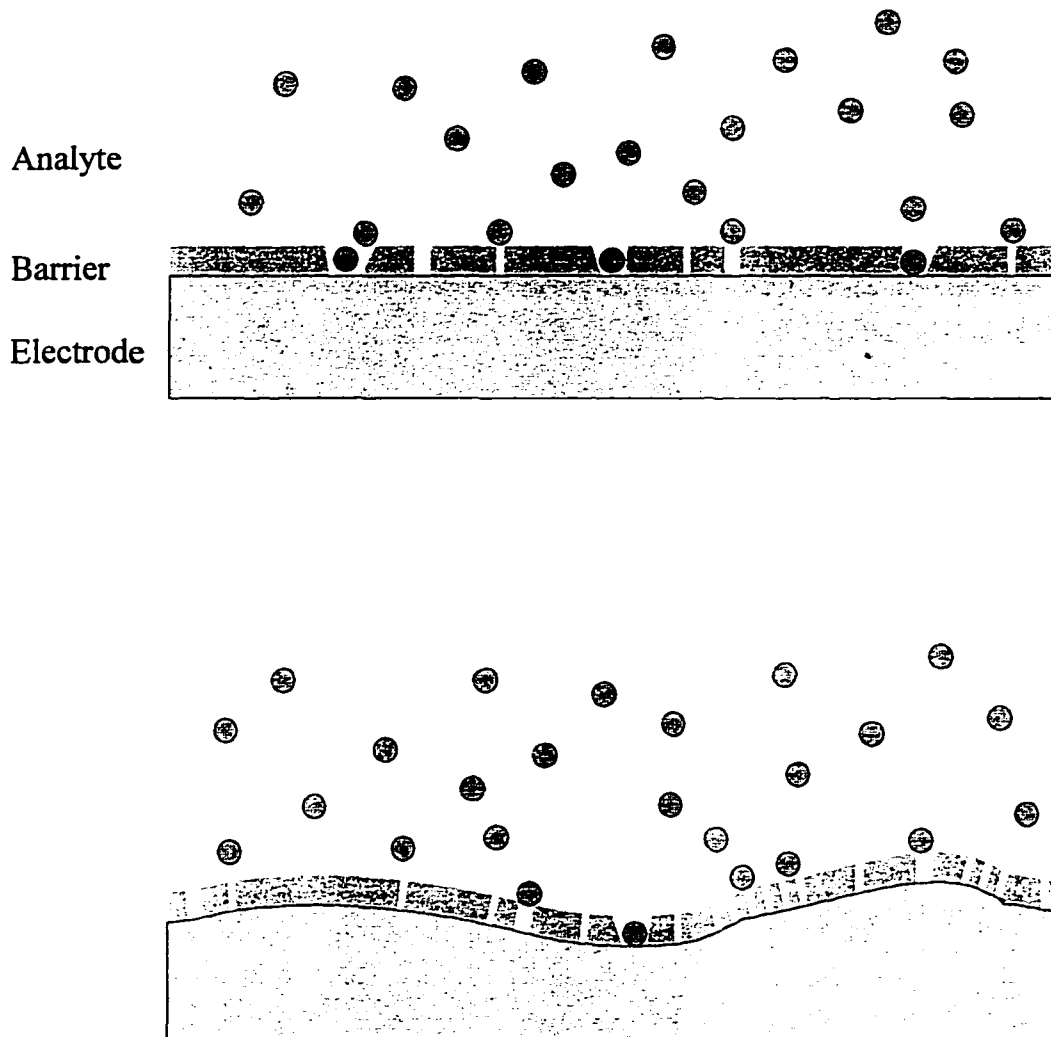


Figure 19 Proposed view of the interfacial barrier to electron transfer. The defects at the smooth substrate, though fewer in number, allow more electron transfer because the broad distribution of sizes includes some defects that are larger than those found at the rough unannealed surfaces.

## **MATERIAL CHARACTERIZATIONS**

As alluded to earlier, the structural information obtained with SFM is subject to errors which arise from the material properties of both the sample and the probe. Although this is an obstacle for structural characterization, it is actually an advantage for interfacial characterization. It is this sensitivity to material properties that makes SFM so powerful as an interfacial characterization tool. This section begins with a brief review of literature related to these material characterizations with an emphasis placed on those studies of alkyl thiolate monolayers. Following this review I present an example study, which uses macroscopic and microscopic characterization of the chain length dependence of SFM measured friction to correlate the monolayer crystallinity with the observed molecular scale friction.

### **SPM Measured Mechanical Properties of Alkyl Thiolate Monolayers**

The nonstructural properties, such as elasticity, friction, adhesion, and other long range interactions, offer a new perspective into microscopy of interfaces in general and organically modified surfaces in specific. Several studies have focused on the measurements of these properties at alkyl thiolate monolayers. While many of these studies are primarily concerned with the fundamental characterization of alkyl thiolate monolayers, others are focused on the extension of these measurements toward all films, and use alkyl thioliates simply as the model system with which to benchmark these technologies. In any case, the result is that a number of SFM studies have been performed at these monolayer interfaces.

The mechanical characterization of alkyl thiolate monolayers at gold has been the focus of many recent papers [109, 110]. Crooks and Houston developed a new SFM design [111] which compensates the deflection of the cantilever as the tip-sample which is effectively a large radii SFM which has a dynamically compensated force feedback thus eliminating certain cantilever induced instabilities common to measuring adhesion with commercial SFM [111]. The more controlled approach and withdraw of the probe at the interface allowed the monitoring of elasticity and adhesion to be measured at thiolated gold [112, 113, 114, 115,

116], which was then compared with the non-thiolated electrode. A dramatic difference was observed in the effect of the monolayer on the elastic-anelastic-plastic deformations that occurred upon contact. The monolayer effectively made the surface resistant to wear by the prevention of the metal-metal contact which results in local welding of the probe and sample, this allowed measurement of the plastic yield stress.

### **Example Study (Chain-Length Dependent Friction)**

The spontaneous adsorption of *n*-alkyl thiolates and  $\omega$ -substituted alkyl thiolates at gold substrates forms well-ordered monolayers that have been utilized as model organic interfaces in a wide range of applications [3, 106]. These adsorbate-substrate combinations have been exploited as tunable barriers in electrochemical charge transfer studies [117, 118, 119], as templates for the examination of adsorbed proteins and cells [120, 121], as coating for molecular recognition sensors [122] and in a variety of additional surface-based applications. This adsorbate-substrate combination also exhibits many of the characteristics that are of merit in model lubrication systems, namely strong headgroup-substrate binding and a densely packed alkyl chain structure.

A number of previous reports describe the results of friction measurements on monomolecular films over macroscopic contact areas [123, 124, 125, 126, 127, 128, 129]. In most cases, these films were deposited on relatively smooth substrates (e.g., mica) to minimize complications from topographic features. Alkyl thiolate monolayers are typically assembled at sputtered or vapor deposited gold films. While these gold films exhibit a predominantly (111) texture, the topography of these substrates generally consists of circular gold crystallites with atomically flat terraces 200 - 300 nm in size [130]. Thus, the examination of the frictional properties of this adsorbate-substrate combination without contributions from substrate topography requires a technique with the ability to probe surface properties at a molecular level.

Scanning force microscopy (SFM) has recently demonstrated a remarkable capability for measuring adhesion [34, 35, 111, 116, 131, 132, 133, 134, 135] and friction forces at nanometer length scales. SFM frictional characterizations of a number of unmodified surfaces

have been reported [36, 37, 39, 136, 137, 138, 139]. Relevant to this work, SFM has also been utilized to measure the friction at surfaces modified with polymers [140, 141], Langmuir-Blodgett (LB) films [142] and surfactant monolayers [143]. In related studies, it has been shown that the microscopic frictional force is sensitive to surface chemistry and several reports have demonstrated chemically sensitive mapping with SFM at micron [144, 145, 146, 147] and sub-micron length scales and this will be detailed below.

We exploit in this paper the versatility of *n*-alkyl thiolate monolayers chemisorbed at gold to prepare films with a range of structural characteristics. Through an in-depth chain length study, we show that the macroscopic structure of these systems greatly influences the microscopic friction. In addition, the molecular scale architecture of these monolayers reveals dislocations in the film structure which demarcate domains that influence friction. The ability of longer chain length alkyl thiolate monolayers to lubricate topographical features is demonstrated and implications of this observation are discussed.

## Experimental Section

### Sample Preparation

Substrates were prepared by the deposition of 300 nm gold films onto freshly cleaved mica. The films were deposited in a cryogenically pumped Edwards 306A vacuum chamber at ambient temperatures at 0.3-0.4 nm/s. The gold-coated substrates were then annealed in an oven at 300°C for 4 hr. The annealed gold-coated substrates were immersed into dilute (0.5-1 mM) alkanethiol-containing ethanolic solutions, a procedure that forms a monolayer chemisorbed at gold as the corresponding thiolate [3, 106]. Ethanol was deoxygenated with high-purity argon immediately before, but not after, solution preparation. Prior to imaging, all of the samples were rinsed extensively with ethanol, and dried under a stream of argon. Ethanol (Quantum, punctilious grade), and most of the *n*-alkanethiols (Aldrich) were used as received. Octadecanethiol (Aldrich) was recrystallized twice from ethanol. Docosanethiol was a gift from A. Ulman (Brooklyn Polytech.).

## Friction Measurements

A MultiMode NanoScope III SFM (Digital Instruments) equipped with 1 and 12  $\mu\text{m}$  scanners was utilized for all measurements. All data were collected in laboratory ambient ( $23 \pm 2^\circ\text{C}$ ) with the sample scanned relative to a stationary tip. Conventional  $\text{Si}_3\text{N}_4$  cantilevers with integrated tips (Digital Instruments) were used after rinsing with methanol. Approximate values of the force constants for the normal bending,  $\sim 0.06 \text{ N/m}$ , of the triangularly shaped cantilevers were calculated as described [148], using physical and material specifications provided by Digital Instruments. The normal force between the tip and sample,  $F_N$ , was estimated from force vs.  $z$ -displacement curves (i.e., force curves, as shown in Figure 5). Values of  $F_N$  represent the *total* normal force, with  $F_N = 0 \text{ nN}$  designated as the point at which the tip “breaks contact” with the surface. Thus,  $F_N$  is the sum of capillary forces, molecular interactions (e.g., hydrogen-bonds, van der Waals, etc.), and applied load.

All of the frictional measurements and images were obtained with the fast scan axis perpendicular to the principal axis of the cantilever while systematically varying  $F_N$ , and correcting for subsequent displacements of the tip. The latter was done to insure the same area of the surface was sampled. Frictional forces,  $f$ , were measured from plots of frictional signal vs. lateral displacement during 50 nm trace/retrace cycles (i.e., friction loops as shown in Figure 6[136]) along a single scan line at  $\sim 1000 \text{ nm/s}$ . The sensitivity of the detector to lateral displacements of the tip was determined from the slopes of 5 nm friction loops at the stationary turnaround points, and torsional force constants of  $\sim 80 \text{ N/m}$  were calculated by approximating the triangularly-shaped cantilever as two parallel beams [148]. Hysteresis in the friction versus normal force was observed in only a few instances when cycling  $F_N$ ; these results were not included in the results herein, as the hysteresis is believed to be the result of monolayer damage.

## SFM Image Acquisition

All images were acquired in the constant force mode at a  $F_N$  of  $\sim 10 \text{ nN}$ . Topographic and lateral force images were collected simultaneously. The instrument was allowed to

equilibrate thermally for ~1 hr after mounting each sample. Vertical displacements were calibrated using the heights of monatomic Au(111) steps (0.236 nm).

### **STM Image Acquisition**

Images were acquired in constant height mode with a Digital Instruments Nanoscope III STM that was equipped with a 0.7  $\mu\text{m}$  scanner. Tunneling currents ( $i$ ) ranged from 50 pA to 5 nA and sample bias voltages ( $V_b$ ) from +1000 to -200 mV. Scan rates varied depending on image size: <30 nm, ~300 nm/s; 50 nm, ~1000 nm/s, and >100 nm, ~2000 nm/s. Tips were fabricated by etching of a tungsten wire (0.010-in diameter) in 1 M KOH. After etching, the tips were rinsed with high purity water and mounted in the scanner. Although only an approximate figure of merit, a tip radius of 10-20 nm was estimated using recently described models [98, 99, 107]. Equilibration times of up to 30 min were generally required to minimize drift. All images were acquired within 1 day of sample removal from the deposition solution. Vertical displacements of the tip were calibrated with respect to the average height of monatomic gold steps at each sample.

## **Results and Discussion**

The following sections describe the results of SFM tribological investigations of  $n$ -alkyl thiolate monolayers chemisorbed at Au(111). First, we demonstrate the ability of alkyl thiolate monolayers to lubricate gold substrate surfaces effectively and present the first quantitative measurements of the frictional force between the chain terminus of these monolayers and an SFM probe tip. We then illustrate the influence of the monolayer alkyl chain length on frictional properties and present macroscopic structural correlations. We finally demonstrate the capability of this adsorbate-substrate combination to modify surface frictional properties in a manner relevant to nanotechnology.

### **Microscopic Friction and Wear**

The ability of a monolayer of octadecanethiolate spontaneously adsorbed at Au(111) (ODT/Au(111)) to reduce microscopic friction is demonstrated in Figure 20, which shows the friction loops at the two surfaces. Curve (a) in Figure 20 is the friction loop at uncoated Au(111), whereas curve (b) is at ODT/Au(111). These data were collected at a scan rate,  $v \sim$

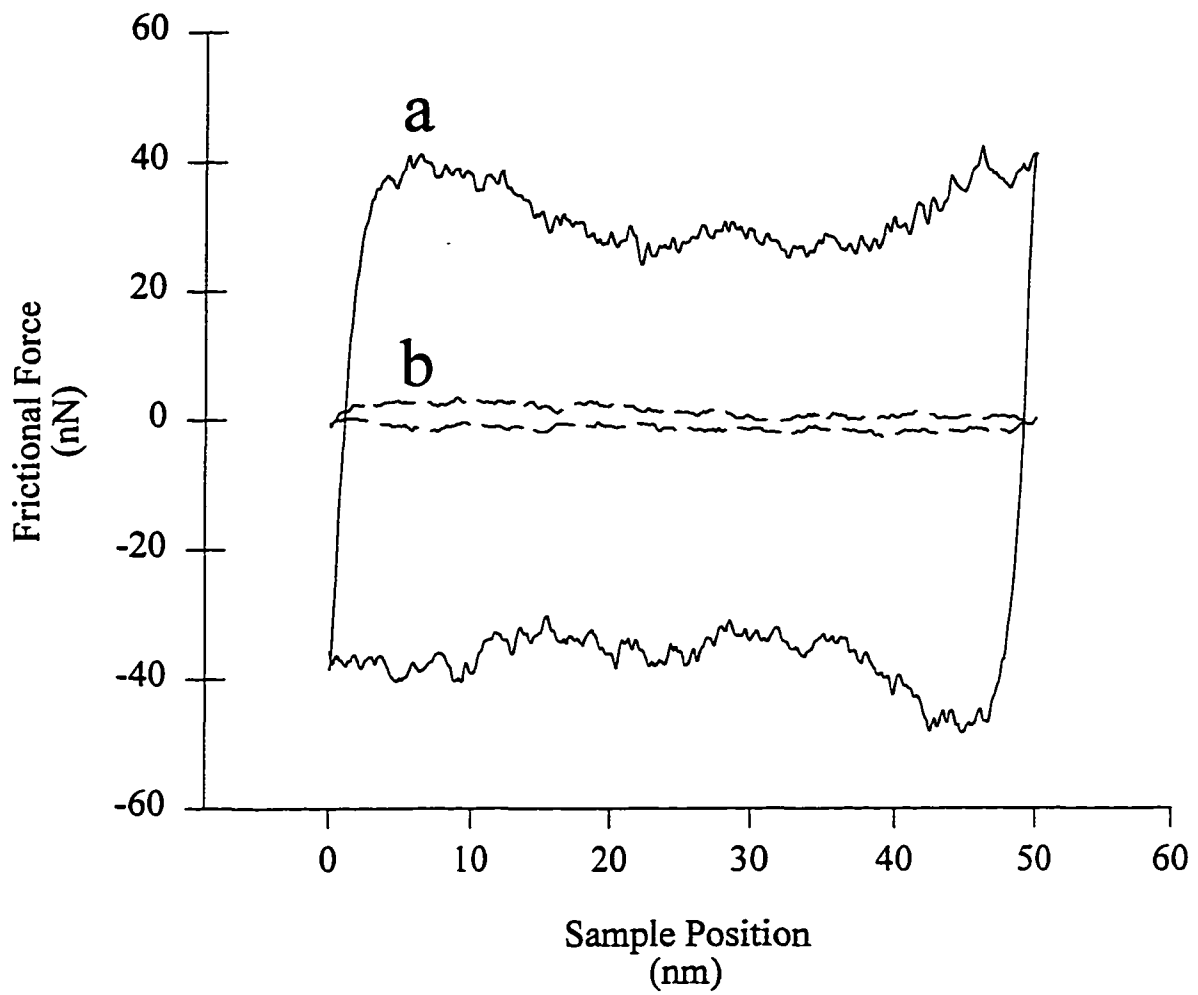


Figure 20 Friction loops for (a) bare Au(111) surface, and (b) an octadecylthiolate modified Au(111) surface.

1  $\mu\text{m/s}$  and a normal force,  $F_N \sim 10 \text{ nN}$ , with the tip positioned on top of large-sized ( $\sim 100 \text{ nm}$  diameter) atomically smooth Au(111) terraces. Measurement of the friction on the tops of the terraces eliminates any topographic contributions of the underlying substrate to the average frictional force [149]. As is apparent, the friction at ODT/Au(111) is considerably less than that at uncoated Au(111). Quantitatively, the friction force ( $f$ ) at uncoated Au(111) is  $\sim 35 \text{ nN}$  and that at ODT/Au(111) is  $\sim 1 \text{ nN}$ . The marked decrease in the microscopic friction at ODT/Au(111) relative to uncoated Au(111) demonstrates the ability of alkyl thiolate monolayers to lubricate at microscopic length scales.

An effective lubricant, in addition to reducing friction, must have the ability to reduce shear induced wear. The topographic images in Figure 21 illustrate the influence of the modification of gold on the wear that results from imaging at high  $F_N$ . Figure 21A is a  $250 \times 250 \text{ nm}$  image of the surface of unmodified Au(111) showing large sized ( $\sim 200 \text{ nm}$ ), circular terraces separated by well-defined monatomic steps. The features in this image remain unchanged while scanning repetitively at  $\sim 25 \text{ nN}$ . Figure 21B shows the same region after five successive scans at  $\sim 80 \text{ nN}$ . A tip induced wear of the surface, as previously observed [107], is clearly evident at the edges of the steps.

In contrast to Figure 21A and B, the images in Figure 21C and D demonstrate that wear can be significantly reduced by modification of the Au(111) surface with an alkyl thiolate monolayer. Figure 21C is a  $350 \times 350 \text{ nm}$  image at a  $F_N$  of  $\sim 10 \text{ nN}$  at ODT/Au(111) whereas Figure 21D is an image of the same area after more than twenty scans at a  $F_N$  of  $\sim 100 \text{ nN}$ . The images are effectively identical leading to two important conclusions concerning the lubrication capability of the chemisorbed monolayer. First, as a result of the strong interactions between the sulfur headgroup and the substrate and the strong cohesive interactions between neighboring polymethylene chains, the ODT monolayer is capable of withstanding a  $F_N$  of  $\sim 100 \text{ nN}$ , a force that corresponds to an effective pressure between the tip and the substrate of  $\sim 2 \text{ GPa}$ . Therefore, the tip slides across the monolayer and does not make contact with the substrate. Second, as a result of the ability of the ODT monolayer to disperse the force of the tip, the underlying Au(111) surface is protected from tip-induced



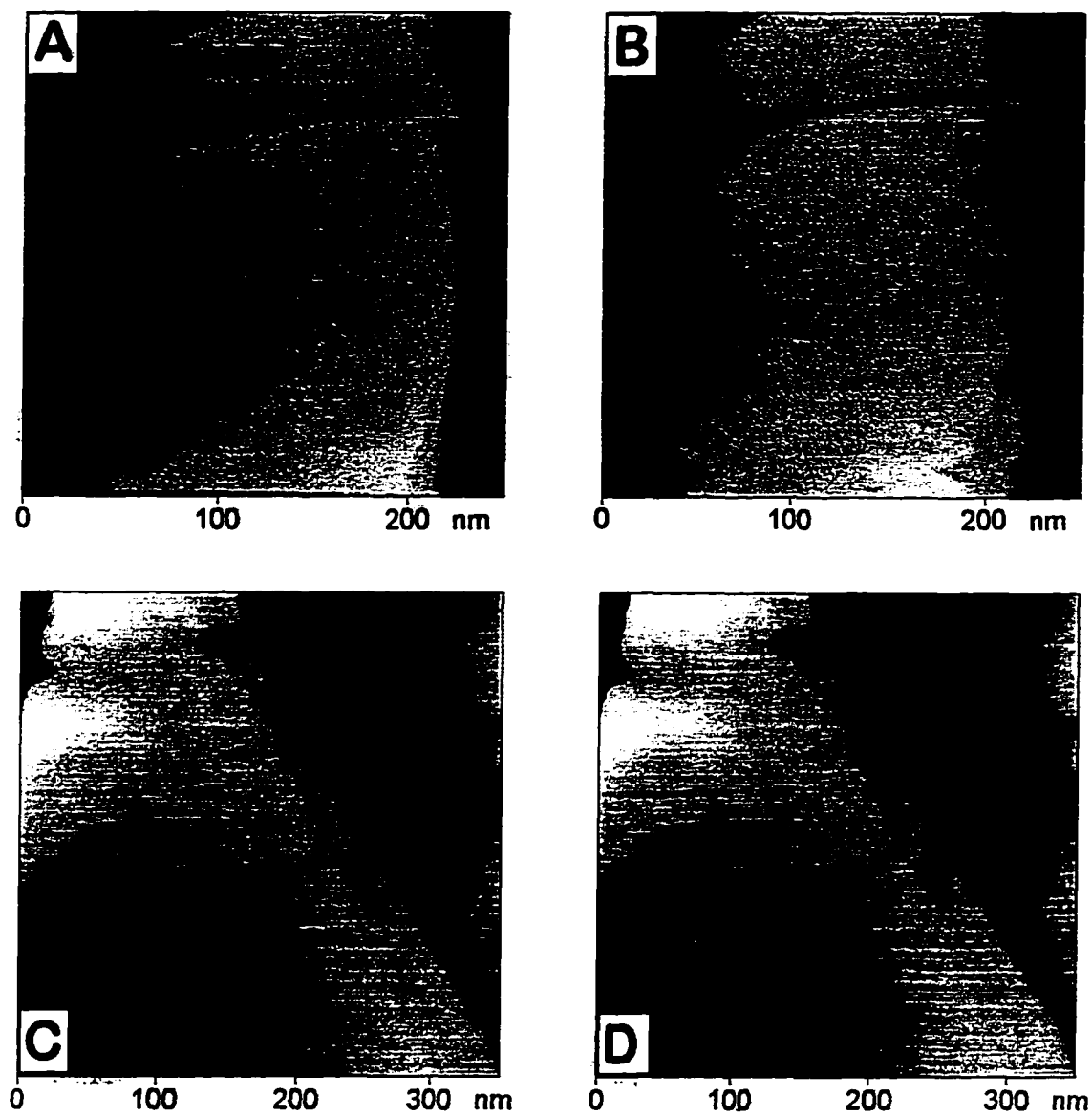


Figure 21 A and B show the topography and friction at a bare Au electrode, while C and D show the corresponding images at an octadecanethiolate monolayer modified gold electrode.

wear. Thus, the ability to reduce both friction (Figure 20) and wear (Figure 21) indicates that alkyl thiolate monolayers chemisorbed to Au(111) serve as effective boundary lubricants.

### **Molecular Friction**

In addition to the understanding of the frictional properties gained at the length scale of Au(111) terraces, insights into the frictional processes of this adsorbate-substrate combination can also be obtained by exploiting the high resolution imaging capability of SFM. Figure 22 presents two examples of frictional responses observed while scanning ODT/Au(111) at molecular length scales. Figure 22A is a  $5 \times 5$  nm lateral force (LF) image at  $F_N = 3$  nN that is characterized by periodic oscillations in the friction force. We have frequently detected these oscillations in LF images without observing the same features in the concurrent topographic image. Such observations indicate that there is minimal crosstalk between the response of the vertical and horizontal position sensitive photodetectors as well as illustrate the higher sensitivity of LF imaging relative to topographic imaging [39]. The spatial arrangement of the oscillation in Figure 22A is hexagonal with a periodicity of 0.5 nm, both of which are consistent with the  $\sqrt{3} \times \sqrt{3}$  overlayer architecture for alkyl thiolate monolayers at Au(111). It follows that the frictional interactions at the tip-sample contact are modulated by the spatial arrangement of the adsorbate.

The periodicity and corrugation of the frictional oscillation in Figure 22A are more clearly illustrated in the cross-section below the image. The shape of this frictional profile is diagnostic of stick-slip behavior [150] at a molecular scale as evident from the 0.52 nm average periodicity [37, 39, 136, 143]. We generally find that the onset of molecular stick-slip occurs at threshold value of  $F_N$  of  $\sim 2$  nN which is consistent with experimental [39] and theoretical [151] observations of atomic stick-slip. The average corrugation amplitude is  $\sim 3$  nN and increases linearly with  $F_N$ . Interestingly, the corrugation amplitude of the stick-slip is greater than the average frictional force measured in friction loops at ODT/Au(111) for all  $F_N$  greater than 2 nN. The periodicity of the stick-slip does not depend on  $F_N$  (2 to 40 nN) and both the periodicity and corrugation are invariant with scan rate (0.5 to 60 Hz). Mechanistically, the molecular stick-slip behavior originates from the interplay of the local frictional forces and the torsional loading of the cantilever. As the two surfaces slide against

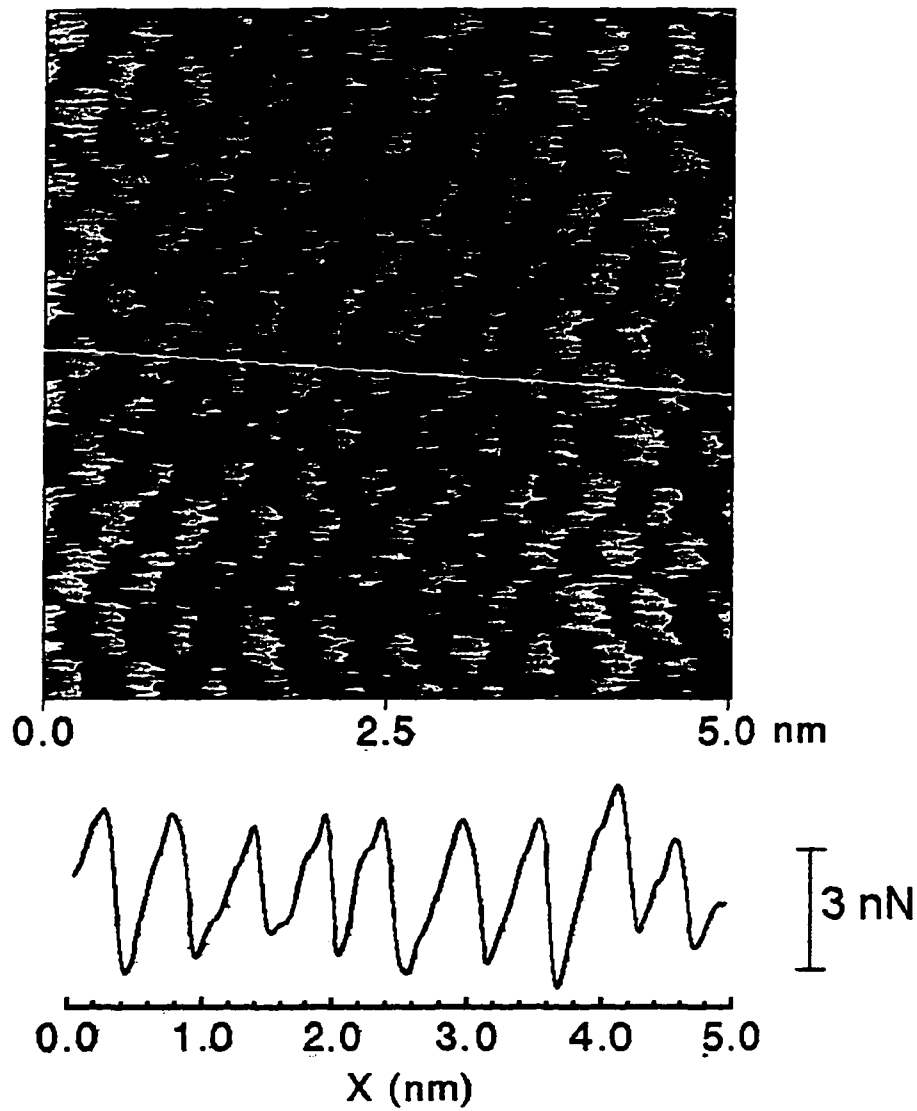


Figure 22

Lateral force image of octadecanethiolate monolayer at gold. This demonstrates molecular periodicity with friction, additionally the line scan in B demonstrates a periodicity one half of the molecular spacing, supporting arguments that the SFM imaging mechanism is a constructive process composed of hundreds of molecules.

each other, the tip “sticks” until the spatial derivative of the lateral force between the tip and monolayer equals the torsional force constant of the cantilever ( $k_t$ ). At this point, the tip “slips” into the next stable position [39]. The modulation in the lateral force is therefore the result of the restricted motion of an adsorbate by the structural barriers posed by neighboring adsorbates. Ultimately, these barriers are overcome by the applied shear stress between the tip and alkyl chain structure of the adsorbate. For an activation-type frictional mechanism, the height of the potential barriers increases linearly with applied pressure. As stated above, we observe a linear increase of the corrugation amplitude with  $F_N$  [152] indicating that the mechanism of molecular scale friction at these systems might be described by an activation model.

Although molecular periodicity is observed in the LF image in Figure 22A, the large contact areas involved in SFM imaging processes make it unlikely that the observed resolution results from interactions of the tip with individual molecules. The tip is probably in contact with a group of molecules simultaneously and it is speculated that the observed resolution is due to the overlay or interference pattern of different images generated by multiple contacts [153].

### Chain Length Dependence

A more detailed picture of the microscopic tribological properties of this adsorbate-substrate combination develops by examining the dependencies of  $f$  as a function of  $F_N$  and alkyl chain length. These data are presented in Figure 23 where the number of methylene groups in the alkyl chain ( $n$ ) ranged from 2 to 17. (The plots for a few of the chain lengths have been omitted for clarity.) The plots in Figure 23 illustrate two important frictional properties of these systems. First,  $f$  increases approximately linearly with  $F_N$ , for each chain length, including those not shown. These dependencies of  $f$  on  $F_N$  can, as will be detailed in the next section, be functionally described by,

$$f = \alpha F_N + f_0$$

where  $\alpha$  and  $f_0$  are the slope and the y-intercept of the plot for each chain length, respectively [154]. This type of dependence is consistent with the Eyring activation model [155, 156] which attributes the deformation of solids to the movement of small molecular domains [124,

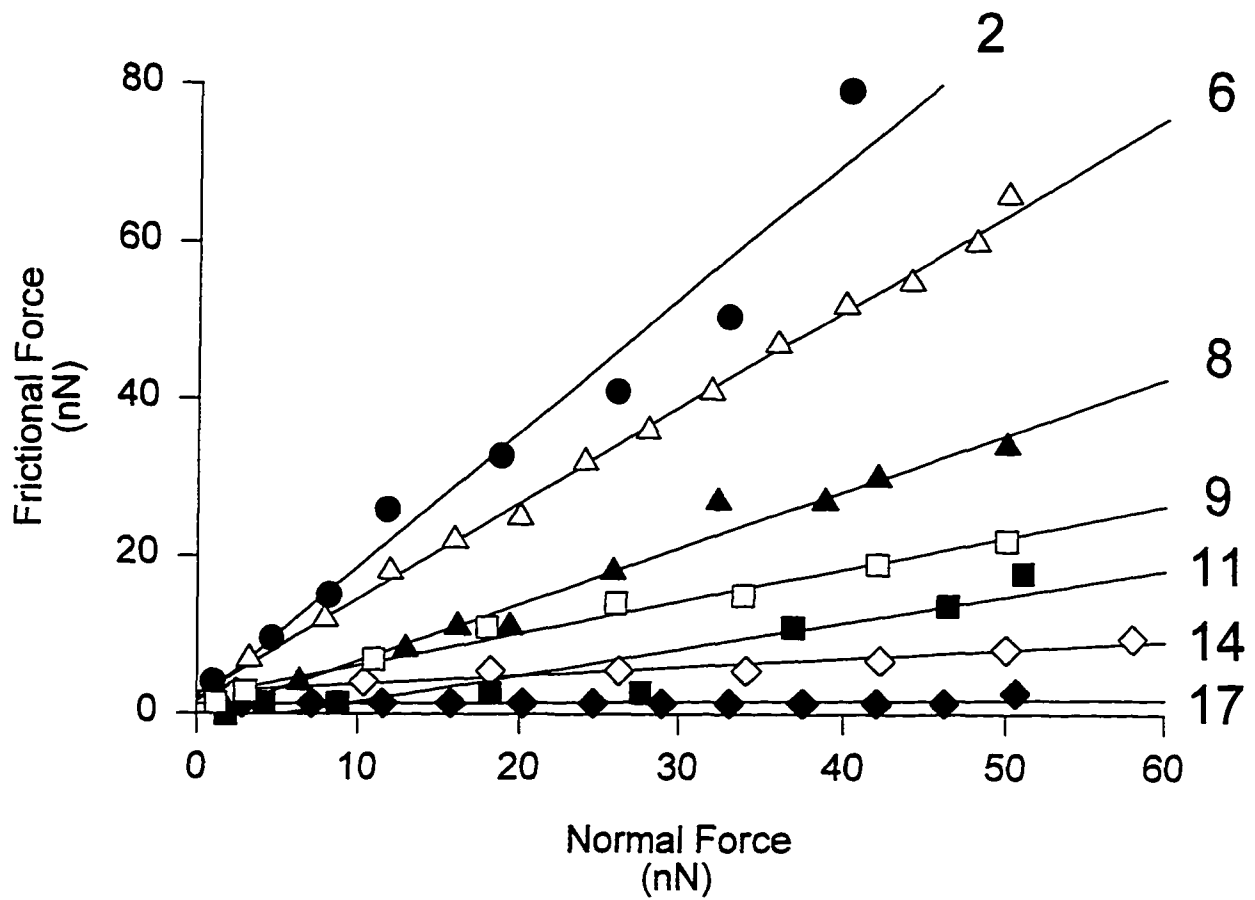


Figure 23 Friction versus Normal force for a series of alkanethiolate monolayers. the number on the plot corresponds to the number of methylene groups in the chain,  $n$ ,  $\text{Au-S}(\text{CH}_2)_n\text{CH}_3$ .

142]. Importantly, this relation successfully describes the experimental [123-127, 142, 143] and theoretical [157] findings for the friction at a variety of monolayer and multilayer systems. Second, the performance of these monolayers structures to function as a lubricant degrades as  $n$  decreases. This degradation is evident from the increase in the slopes of the  $f$  vs.  $F_N$  plots. For example, for  $n = 21$  the frictional force is virtually undetectable over all of the tested values of  $F_N$  which reflects an *effectively* frictionless sliding contact between the tip and sample. However, for shorter chain lengths (e.g.,  $n = 6$ )  $f$  shows a strong dependence on  $F_N$  attaining a considerably high value of  $\sim 60$  nN at  $F_N = 50$  nN. Thus, the length of the alkyl chain governs the quantitative effectiveness of these films as lubricants.

Figure 24 details further the relationship between  $\alpha$  and the number of methylene groups of this adsorbate-substrate system. The  $\alpha$ -values exhibit a bimodal dependence on  $n$ . From  $n = 15$  to 21, the change in  $\alpha$  is comparatively small, with all values less than  $\sim 0.1$ . In contrast, the dependence of  $\alpha$  on  $n$  becomes markedly greater below a  $n$  somewhere between 11 and 14. Furthermore, the transition in the frictional properties as  $n$  decreases results in a value for  $\alpha$  at  $n = 2$  that is about two orders of magnitude larger than those at longer chain-lengths (e.g.,  $n = 17$ ). Interestingly, our microscopic investigations yield values of  $\alpha$  for longer-chain alkyl thiolate monolayers ( $\alpha = 0.012$  to 0.05) that are similar to those measured at LB films ( $\alpha \approx 0.04$ ) [124] and to that predicted in a molecular dynamics simulation of hexadecanethiolate on gold ( $\alpha \approx 0.02$ ) [157]. These data further illustrate, as discussed in more detail in the next section, that the frictional properties of these monolayers have a strong dependence on  $n$ .

### Structural Correlations

Insight into the dependence of  $\alpha$  on the chain length can be gained from the qualitative descriptions of the chain structure of this adsorbate-substrate system. Macroscopic structural characterizations have shown that the architecture of these monolayers is strongly influenced by the length of the alkyl chain [54, 65, 82, 158, 159]. The combined weight of these studies indicates that the chain structure of monolayers prepared from longer chain lengths is *comparatively* well-ordered and more densely packed and that of monolayers from shorter

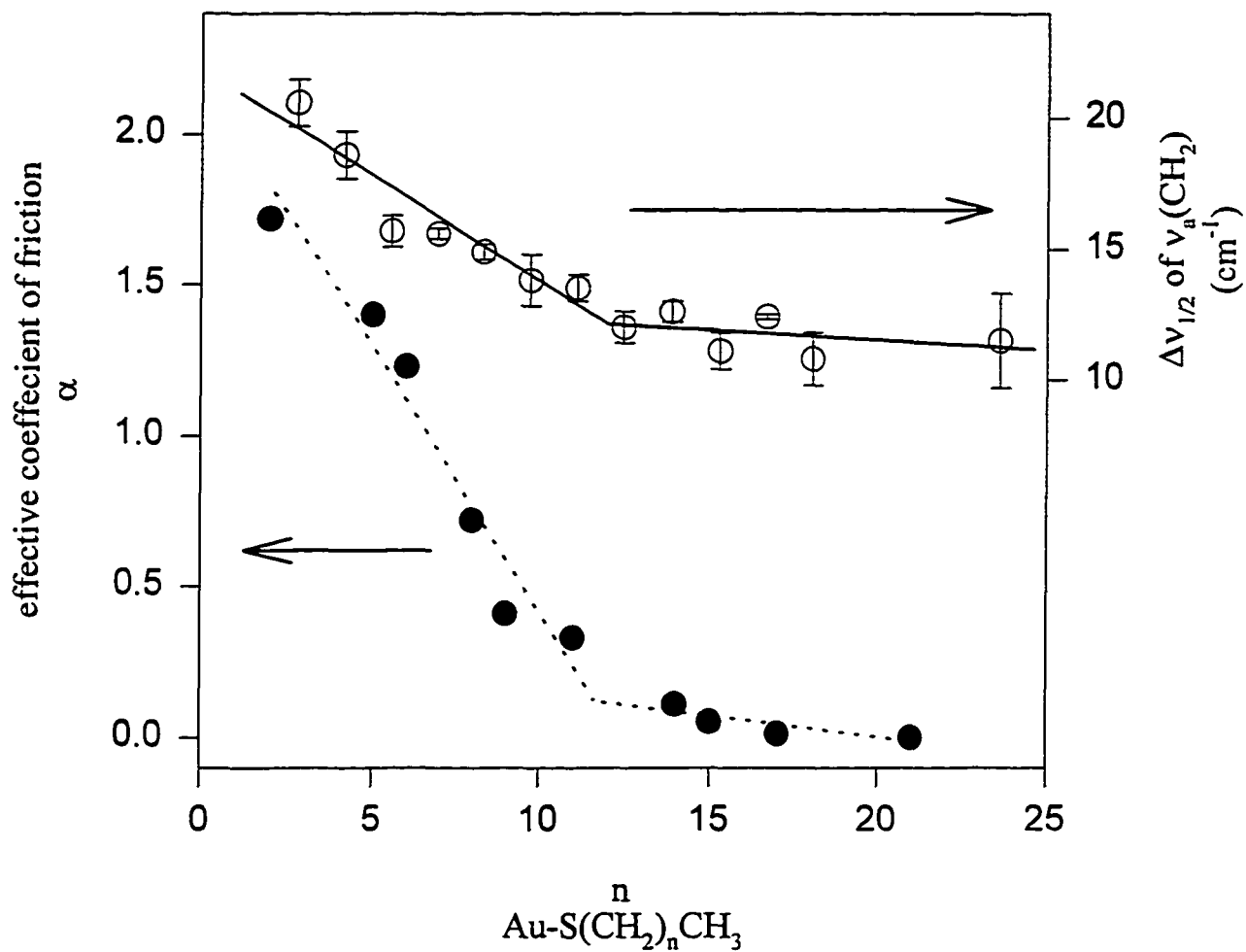


Figure 24  $\Delta\nu_{1/2}$  for  $\nu_a(\text{CH}_2)$  and  $\alpha$  versus the  $n$ . This plot emphasizes the correlation between a macroscopic measure of monolayer crystallinity and the microscopic measurement of friction made with SFM.

chain lengths is more disordered and less densely packed. To assess the influence of chain packing on  $f$ , we have examined the details of the diagnostic features in infrared external reflection spectroscopy (IR-ERS) data of this system. As previously shown, a valuable structural diagnostic from IR-ERS data is the correlation between the packing density and the bandwidth of the asymmetric methylene stretching mode ( $\nu_a(\text{CH}_2)$ ) [160, 161]. Crystalline  $n\text{-C}_{20}\text{H}_{42}$  has a full width at half maximum ( $\Delta\nu_{1/2}$ ) for the  $\nu_a(\text{CH}_2)$  mode of  $11\text{ cm}^{-1}$  as compared with a broader  $\Delta\nu_{1/2}$  of  $18\text{ cm}^{-1}$  for hydrocarbon chains with a lower packing density [160, 161]. Accordingly, Figure 24 contains a plot of  $\Delta\nu_{1/2}$  of the  $\nu_a(\text{CH}_2)$  mode for alkyl thiolate monolayers as a function of chain length [162]. As observed in the plot of  $\alpha$  vs.  $n$  in the same figure,  $\Delta\nu_{1/2}$  exhibits two regions of dependence, with a transition at  $n \approx 13$ . Thus, the longer chain length monolayers ( $n \geq 13$ ) have  $\Delta\nu_{1/2}$  values of  $11$  to  $13\text{ cm}^{-1}$  which are diagnostic of a more densely packed chain structure. For  $n \leq 12$ ,  $\Delta\nu_{1/2}$  begins to increase with decreasing  $n$ , arguing that the packing density of the chain structure decreases [163]. The structural insight from the dependence  $\Delta\nu_{1/2}$  on  $n$  agrees with an interpretation based on the positions of the  $\text{CH}_2$  stretching modes, which are also sensitive to the intermolecular environment of the alkyl chains [54, 164]. Both interpretations are consistent with energetic considerations, whereby the cohesive interactions between the neighboring chains in these monolayers increase by  $\sim 0.8\text{ kcal/mol}$  of  $\text{CH}_2$  which, in part, overcomes thermally induced structural disordering [165]. Importantly, the plot of  $\Delta\nu_{1/2}$  vs.  $n$  virtually mirrors the plot of  $\alpha$  vs.  $n$ . This correlation indicates that the microscopic friction of these monolayer assemblies is highly dependent on the packing density of the alkyl chains.

In the next section we show that both  $\alpha$  and  $f_0$  are dependent on the chemical functionality of the surface of longer chain thiolate monolayers adsorbed at Au(111). While Figure 23 indicates that  $f$  is linear with  $F_N$  for all values of  $n$ , it is clear that  $\alpha$  is also governed by the length and packing of the alkyl chains. In contrast, to the results for functionalized monolayer surfaces (presented below),  $f_0$  for  $n$ -alkyl thiolate monolayers is  $\sim 0.1\text{ nN}$  for all chain lengths indicative of comparatively low surface free energies for methyl terminated systems. Thus, the SFM measured microscopic friction at thiolate monolayers not



only depends on the chemical nature of the interface, as shown in the next section [145] but also on packing density of the chain structure. The next section examines the importance of this conclusion at a mechanistic level.

The conclusions from the above analysis are also consistent with energy dissipative descriptions of friction. When two macroscopic surfaces slide against one another, energy dissipation occurs by the plastic deformation of surface asperities [166]. On a microscopic scale, as is the case when a SFM tip is translated across a surface, energy is dissipated through reorganizational pathways. Recent molecular dynamics studies on the sliding of monomolecular films indicate that the mode of energy dissipation in these types of systems is associated with vibrational energy via an oscillation in the tilt angle of the molecules. The shear induced disorder of the chain structure in the shorter chain alkyl thiolate monolayers therefore dissipates energy through bond rotations and vibrations and is manifested in a higher observed microscopic friction. In addition, we frequently observe wear in the structure of monolayers for  $n \leq 5$  at moderate  $F_N$  (e.g.,  $\sim 50$  nN) indicating that plastic deformation also contributes to the higher friction of these systems. The longer chain, more crystalline films, on the other hand, exhibit a much lower friction indicating that less energy is dissipated during sliding because of their ability maintain order. Furthermore, as shown in Figure 21, these systems do not exhibit wear and retain structural integrity at comparatively large normal forces (e.g.,  $\sim 100$  nN).

In summary, the mechanism of microscopic friction at  $n$ -alkyl thiolate monolayers chemisorbed at Au(111) is consistent with a reorganizational energy dissipation mechanism. The ability of monolayers prepared from longer chain length alkylthiols to maintain molecular scale order during friction measurements leads to lower  $\alpha$  values and friction. The frictional mechanism involves the cooperative motion of domains consisting of a few hundred molecules which are defined by dislocations observed in STM images of this adsorbate/substrate system (Figure 22).

### **Frictional Damping of Topographic Structures**

The data in Figure 20 and Figure 21 clearly show that the more densely packed structures of long chain alkyl thiolate monolayers chemisorbed at gold serve as effective boundary

lubricants on atomically smooth surfaces (i.e., Au(111) terraces). The SFM images in Figure 25 demonstrate the ability of these films to function as lubricants at rougher, more technologically relevant surfaces. Figure 25A and B are respective  $300 \times 300$  nm topographic and lateral force images of unmodified Au(111) substrates. As shown in the topographic image and in earlier reports [130], the surface of these substrates is composed of circular 200 to 300 nm crystallites, that are separated by grain boundaries of varied width. The steps and terraces on each crystallite in Figure 25A appear “unfocused” because of the relatively large contact area between the SFM tip and the sample. On the other hand, Au(111) terraces are easily distinguished as extended regions of constant friction in the lateral force image, Figure 25B. Both steps and the boundaries between crystallites appear as localized regions of increased lateral force that are apparent throughout the image. For example, as the tip moves up a single atomic step that separates two large sized Au(111) terraces, the lateral force increases by  $\sim 13$  nN. This transient change reflects the torsional loading on the cantilever as the tip “trips” up the step [137, 141]. In contrast, movement of the tip across the boundaries between crystallites can induce frictional changes ( $\Delta f$ ) up to  $\sim 35$  nN. Thus, the interaction of the tip with topographic features as small as single atomic steps (0.23 nm in height) can induce a notable increase in the SFM-measured friction.

The images of Figure 25C through H illustrate that the frictional response of topographic structures can be manipulated by modifying the gold substrates with alkyl thiolate monolayers. Figure 25C and D are the corresponding topographic and friction force images of heptanethiolate (HPT,  $n = 6$ ) chemisorbed at Au(111). The  $\Delta f$  values at the atomic steps in Figure 25D are  $\sim 2$  nN which is significant but notably less than that at unmodified gold substrates. For DT/Au(111) ( $n = 9$ ), as shown in Figure 25E and F,  $\Delta f$  is  $\sim 0.5$  nN and for ODT/Au(111), Figure 25G and H,  $\Delta f$  is below our detection capability of  $\sim 0.2$  nN. Qualitatively, these data show that as the length of the alkyl chain increases, the frictional images become increasingly featureless because the contribution of the steps to the average friction decreases. In a more quantitative manner, Table 2 details  $\Delta f$  values at steps for a range of alkyl chain lengths including those in Figure 25. These data were obtained from a number of different samples of each surface using different SFM tips. Although the size and

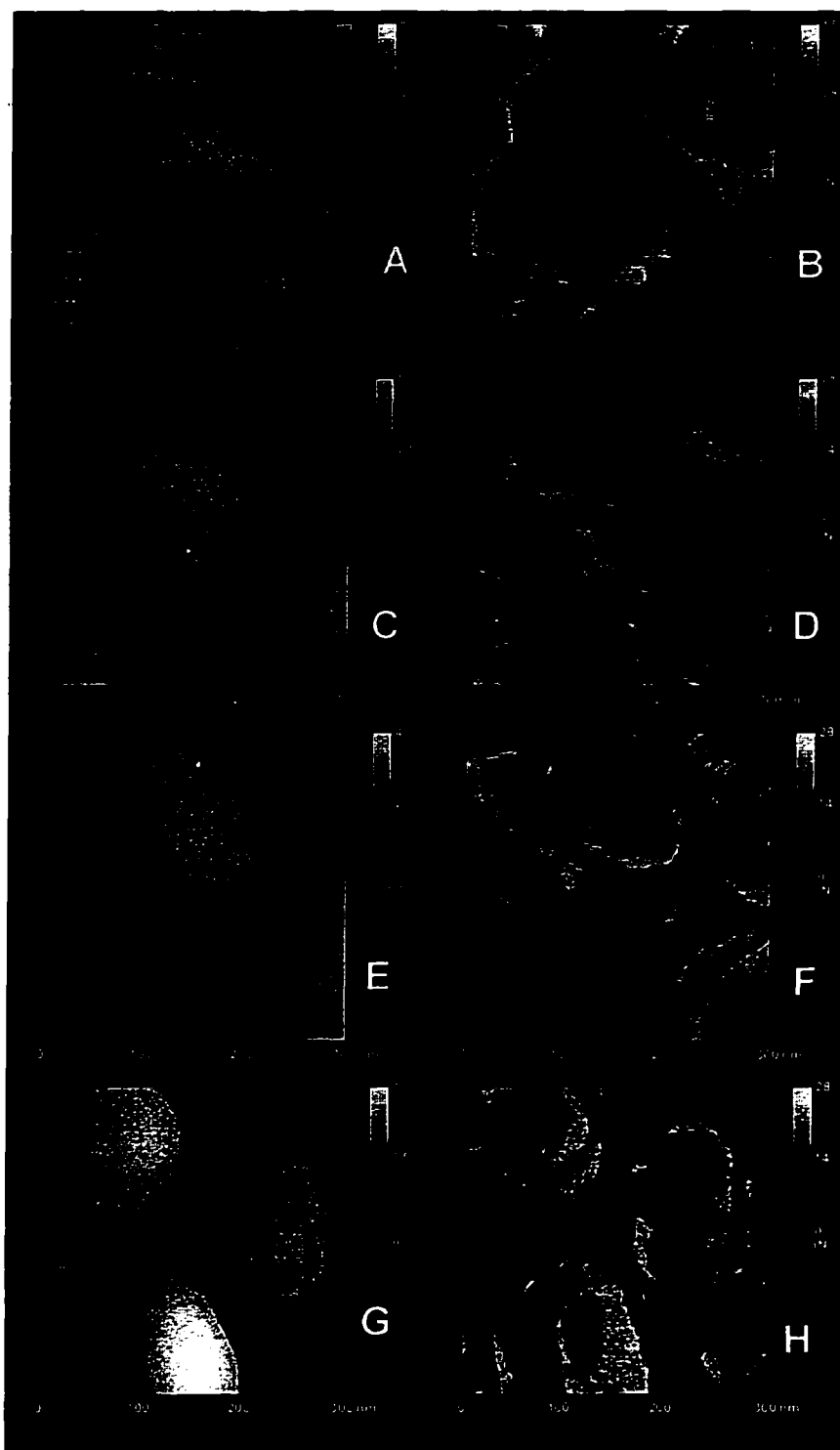


Figure 25 Topography and friction images of (A&B) bare Au, (C&D) heptanethiolate-Au, (E&F) decanethiolate-Au, (G&H) octadecanethiolate-Au. Thus demonstrating the lubricating effect of an organized chemisorbed monolayer

**Table 2** Frictional Signals Observed at Au(111) Monatomic Steps

Surface	$n$	$\Delta f$ at Au(111) steps (nN) <sup>a</sup>
Unmodified Au(111)	0	$22 \pm 12$ (N = 45)
CH <sub>3</sub> (CH <sub>2</sub> ) <sub>2</sub> S-Au(111)	2	$12 \pm 5$ (N = 8)
CH <sub>3</sub> (CH <sub>2</sub> ) <sub>5</sub> S-Au(111)	5	$5 \pm 4$ (N = 15)
CH <sub>3</sub> (CH <sub>2</sub> ) <sub>6</sub> S-Au(111)	6	$4 \pm 2$ (N = 8)
CH <sub>3</sub> (CH <sub>2</sub> ) <sub>9</sub> S-Au(111)	9	$1 \pm 0.5$ (N = 10)
CH <sub>3</sub> (CH <sub>2</sub> ) <sub>17</sub> S-Au(111)	17	0

<sup>a</sup> N equals the number of steps examined.

shape of the SFM tip play a crucial role in “sensing” topographic features, an explanation of the observations in Figure 25 can be developed within the framework of the structural and frictional data in Figure 21. The molecular scale mechanism by which *n*-alkyl thiolate monolayers damp the SFM measured friction at steps can be understood by comparing the length of the alkyl chain with the height of a Au(111) atomic step and the resulting effect on film structure. For example, the thickness of an ODT layer (~2.6 nm) is significantly greater than the height of a Au(111) step. Although a step will induce a slight offset at the ends of the chains below and above the step edge, sufficient chain-chain interplay exists over the remaining portion of the chains to form an ordered structure at the step. Thus, because the densely packed structure for ODT/Au(111) is not interrupted at a step edge, resulting in friction at steps that is unchanged from that at terraces. Stated differently, the longer chain length systems effectively disperses both the normal and frictional force of the tip at the steps which results in a more uniform “flow” of the tip across the terrace edge.

For shorter chain lengths, on the other hand, which are less densely packed at flat terraces, the height of a Au(111) step is a significant fraction of the total chain length. The

offset induces a comparatively more notable weakening of the cohesive interactions at step edges. The end result is that the shearing of the SFM tip-monolayer junction at steps disrupts the structure of short chain length films to the extent that the tip is able to “sense” the presence of the step. This mechanism and the observations in Figure 23 and Figure 24 are consistent with the results presented above and demonstrate the ability of crystalline monolayer films to damp the friction of topographic features.

## Conclusions

We have utilized SFM to examine the molecular scale frictional properties of *n*-alkyl thiolate monolayers chemisorbed at gold for the first time. These films can reduce the friction between an SFM probe and modified Au(111) terraces by a factor of 35 and inhibit tip induced wear which demonstrates their worth as boundary lubricants. In LF images, we have observed a molecular scale stick-slip behavior exhibiting a 0.5 nm periodicity which is characteristic of a  $\sqrt{3} \times \sqrt{3}$  overlayer structure. The versatility of this substrate-adsorbate combination enabled us to perform an extensive chain length study. The microscopic frictional properties of these assemblies can be correlated with results from macroscopic structural characterizations indicating that friction is governed by film structure. The results argue that the ability of longer chain length alkyl thiolate monolayers to retain molecular scale order during shear leads to lower SFM measured friction. The ability of crystalline thiolate monolayers to damp the frictional response of topographic variations has been demonstrated and understood within the framework of the above analysis. The observation of low friction at sharp topographical features has important implications in technologically significant areas such as the magnetic recording industry.

## Conclusions

There are two key conclusions from this section. First, the sensitivity of SPM to these material properties offers scientists access to a wide range of characterization applications. And second, the various material properties of the system must be considered when interpreting the data obtained with SPM. If these techniques are to be applied to the more

complex real-world systems, i.e. polymer films, etc., then more studies will be required. As more materials are characterized by their microscopic frictional, elastic, and adhesive qualities, the value of this technique will dramatically increase. Additionally, if micromechanical devices are to become common elements in the next technological wave, then an understanding and control of their surface properties, especially wear, will be critical to their successful development, these techniques clearly have something to offer in that respect.

## CHEMICAL INTERPRETATIONS

As the derivatives of STM expanded, so did the number of accessible properties. The SFM was rapidly becoming a multi-functional probe microscope. In many studies there were correlations drawn between the friction or adhesion and the surface free energy or chemistry of the sample surface. Currently there are similar efforts under way along the lines of non-contact phase differences that are being suggested that they are a measure of the adhesive interactions between the sample and the probe. Hopefully this will prove fruitful, as this technique is considerably less invasive than the corresponding contact modes. The study which I describe below; however, is a contact SFM study, where the free energy, chemistry, of the surface was tuned by the variation of the terminal groups of alkyl thiolate monolayers at gold. The primary use of the SFM was to monitor changes in the friction as the surface free energy of the surface was changed.

### Material Properties - Chemical Interpretations

Recently there has been a surge for the application of chemically modified probes as the key to attainment of chemical sensitivity, specificity, and discrimination. In the first investigation along those lines, Houston et al.[116], monitored the contact potential difference at a series of end-group functionalized alkyl thiolates. The measurement involved measuring the interaction force at a fixed separation while varying the potential difference. The probe was modified with a methyl terminated alkanethiolate monolayer and the various sample monolayers were terminated with  $-\text{CF}_3$ ,  $-\text{CH}_3$ ,  $-\text{CH}_2\text{OH}$ , and  $-\text{CO}_2\text{H}$  groups. The data conformed to a parabolic potential dependence with attractive forces at both positive and negative potential differences. The notable measurement comes from the potential of zero force. This potential difference is correlated with the dipole moments of the terminal functional groups. This was the first demonstration of chemical discrimination with a chemically modified probe.

Of all the nonstructural properties, friction measurements have by far been the most common in the literature. Initial measurements performed at LB films demonstrated that friction can distinguish regions formed of compositionally different materials [142, 145]. And more recent work [167], characterized the frictional responses of a wide range of end-group derivatized alkyl thiolate monolayers. Frictional force measured with SFM is observed to vary linearly with the applied normal force for many surfaces, and the dependence on thiolate monolayers is no different. The proportionality constant that relates the friction to the normal force is used as a measure of both surface free energy. However, to fully attain *chemical* discrimination, and eventually identification, a need is required to decouple the *material* aspects of the film, elasticity, topography, etc. from those chemical aspects evident in the free energy. Our results presented here represent a significant step toward the characterization of the chemical component of frictional forces, as the same probe was applied to all surfaces, and the monolayers are composed of similar length polymethylene chains. A study subsequent to our own, some initial efforts at separating elasticity were performed [147], which simultaneously monitored friction, elasticity and topography for monolayers of identical length and structure, except for the endgroups. Using a transfer technique known as micro-contact printing thiolates are deposited at the gold forming a microscopic array of chemically dissimilar regions. While the elasticity comparisons presented in that study are only qualitative they show that even with films as similar as these there exist material, i.e., elastic, differences. The separation of the chemistry from the measurements has yet to be achieved. A similar study by Lieber et al [146, 168] demonstrated a correlation between friction, adhesion with the surface chemistry of these monolayers, again at micron scale patterns. In our study presented here, these techniques have been extended to the nanometer regime in a study of spontaneously adsorbed bilayers of alkyl thiolates. The partial bilayers formed as gold-mercaptohexadecanoic acid-stearic acid display domains of bilayer with regions of uncovered monolayer. These structures allow discrimination of the two regions by both topography as well as by friction. with adhesion however it was not until the application to alkyl thiolate monolayers that the chemical aspects could be compared, uncoupled with elasticity. Its success lies in the relative sensitivity of the measurement to the functionality of



the end-group of the monolayer. These studies are part of an effort to learn more about SFM measurement of these properties as well as to gain insight into spontaneously adsorbed alkyl thiolate monolayers. Material properties, such as elasticity, provide information about the film cohesion and order, while other interactional properties, such as friction and adhesion provide information about the interaction of the film with other species. The impetus for these studies in an effort to learn more about alkyl thiolate monolayers, as well as to begin to build a network of understanding about these kinds of measurements with SFM. With regards to the spontaneously adsorbed alkyl thiolate monolayers, these properties have been of these films is critical for an accurate understanding of the electrified interface. Access to material properties of the film as a function of applied potential, electrolyte concentration electrolyte type, or solvent.

Access to these nonstructural properties offers chemical microscopy an unprecedented opportunity. The possibility of nondestructive chemical discrimination, if not identification, at a molecular scale, which is widely applicable to various samples under varied environments. While the actual properties measured do not offer direct access to chemical identification, careful analysis has led to the discrimination of chemically distinct regions. With further characterization these properties may allow actual identification. However, even without chemical identification the measurement of these properties at the molecular-scale regime allows access to surface properties and dynamics

### **Example Study (Functional Group Dependent Friction)**

This study demonstrates the ability to map chemically distinct domains at nanometer length scales using SFM. The basis of this characterization is the dependence of the frictional interactions on the identity of the chemical functional groups at the outermost few angstroms of microscopic contacting areas, i.e., the surface free energies. Such a dependence is confirmed by characterizations of the frictional force between a variety of end-group derivatized alkanethiolate monolayers deposited at both gold-coated sample substrates and gold-coated FFM probe tips. Coupled with this dependence, we show that the composition of chemically distinct domains at partially formed bilayer structures can be mapped at a spatial

resolution of ~10 nm, with the image contrast governed by the surface free energies of the microscopic contacts. Opportunities presented by these findings are briefly discussed.

A wide variety of chemical, biological, and physical processes (e.g., heterogeneous catalysis, recognition, and friction and wear) are governed by interfacial molecular architectures at nanometer length scales [1, 3, 169]. Pathways for manipulating surface structures at this length scale are also emerging, yielding the potential to create complex patterns for molecular-based electronics [170, 171, 172] and high performance chemical sensors [3, 169]. The ability to discriminate [32, 34, 116, 131, 132, 133, 134, 173] and map chemical composition [43, 144, 145, 146, 147, 174, 175, 176, 177, 178, 179, 180, 181, 182] at nanometer-level resolution is therefore of significant fundamental and technological interest.

A number of techniques have exhibited the capability to resolve spatially chemical composition of surfaces at micron length scales, e.g., secondary ion mass spectrometry [147], scanning electron microscopy [177], and friction force microscopy [43, 144, 145, 175, 146, 147, 174]. Near-field scanning optical microscopy offers the potential for imaging surfaces spectroscopically at even higher resolution [181]. As related to the focus of this paper, the use of atomic force microscopy (AFM) [36, 138] for chemical characterization relies on the correlation of the probe-sample interactions, e.g., adhesion [32, 34, 43, 131, 132, 133, 144, 145, 174, 175] or friction [145, 146, 147], with the chemical composition of the contacting surfaces. The full potential of this technique for compositional mapping at high spatial resolution, however, has yet to be realized.

Building upon previous micron-scale mapping studies of Langmuir-Blodgett films [43, 144, 145, 174, 175], we extend herein the capability of AFM, applied in a frictional force mode [36, 138], to resolve spatially the chemical composition at two types of test interfaces. By exploiting the ability of AFM to both image surfaces at nanometer length scales and measure frictional forces [36, 138], we demonstrate chemical mapping with a resolution as high as 10 nm. We also confirm that the contrast of such maps can be systematically altered by the controlled variation of surface functionality at the AFM probe tip [146, 147]. Thus, by modifying the chemical functionality of the probe tip, the frictional force between the

contacting surfaces can be manipulated to vary the “frictional contrast” of the compositional map.

## Experimental Section

### Sample Preparation

Substrates were prepared by the deposition of 300 nm of gold onto heat-resistant glass (Tempax, Berliner Glas). Prior to gold deposition, the Tempax glass was cleaned by immersion into piranha solution (1:3 H<sub>2</sub>O<sub>2</sub>/H<sub>2</sub>SO<sub>4</sub>), followed by successive sonication in deionized H<sub>2</sub>O, ethanol, and methanol. Caution: The H<sub>2</sub>O<sub>2</sub>/H<sub>2</sub>SO<sub>4</sub> solution reacts violently with organic compounds and should be handled with extreme care. Gold was deposited in a cryogenically pumped Edwards 306A vacuum chamber at ambient temperatures using evaporation rates of 0.3-0.4 nm/s. The gold-coated substrates were then annealed in an oven at 300°C for 4 hr., and subsequently under a H<sub>2</sub> flame [183]. Uncoated Si<sub>3</sub>N<sub>4</sub> AFM cantilevers with integrated tips (Digital Instruments) were rinsed with methanol prior to use; tips subsequently modified with an alkanethiolate monolayer were coated with 40 nm of gold immediately after deposition of a 2 nm adhesive layer of chromium.

The annealed gold-coated substrates and the gold-coated AFM tips were chemically modified by their immersion into dilute (~0.5-1 mM) alkanethiol-containing ethanolic solutions, a procedure that forms a monolayer chemisorbed at gold as the corresponding thiolate [3, 106]. By using a selected set of end-group functionalities (see Table 3), surfaces with well-defined differences in free energy were fabricated [158, 184]. Bilayer samples were prepared by immersion of annealed gold-coated substrates into ethanolic solutions of 0.1 mM 16-mercaptohexadecanoic acid and 1.0 mM stearic acid for ~24 hours. Infrared spectroscopic data confirmed the formation of the bilayer structure through the detection of the carbonyl stretching mode diagnostic of head-to-head hydrogen-bonded dimers [185, 186]. Ethanol was deoxygenated with high-purity argon immediately before, but not after, solution preparation. Prior to imaging, all of the samples were rinsed extensively with ethanol, and dried under a stream of argon.

Ethanol (Quantum, punctilious grade), 16-mercaptohexadecan-1-ol (Pharmacia Biosensor AB), and octadecanoic (stearic) acid (Aldrich) were used as received. Octadecanethiol (Aldrich) was recrystallized twice from ethanol. 1-Bromo-21-mercaptoheicosane was a gift from A. Ulman (Brooklyn Polytech.). 16-Mercaptohexadecanoic acid was synthesized as described in the literature [158], and methyl-16-mercaptohexadecanoate was synthesized by dissolving 16-mercaptohexadecanoic acid into methanol and adding a catalytic amount of concentrated hydrochloric acid [185].

### Friction Measurements

A MultiMode NanoScope III AFM (Digital Instruments) equipped with 1 and 12  $\mu\text{m}$  tube scanners was utilized for all measurements. All data were collected with the sample mounted in a small cell under an atmosphere of flowing high purity argon at room temperature ( $23 \pm 2^\circ\text{C}$ ) with the sample scanned relative to a stationary tip.

**Table 3** Frictional parameters for the contacts formed between an uncoated  $\text{Si}_3\text{N}_4$  AFM tip and several different end-group terminated alkanethiolate monolayers ( $\text{Au-S}(\text{CH}_2)_n\text{-X}$ ) chemisorbed at  $\text{Au}(111)^a$ .

End-group <sup>b</sup>	$\cos \theta_a^c$	$\alpha$	$f_0$ (nN)	$f$ (nN) for $F_N = 20$ nN
$-\text{CO}_2\text{H}$ (n=15)	$\sim 1$	0.76	22	$42 \pm 7$
$-\text{CH}_2\text{OH}$ (n=15)	$\sim 1$	0.70	8	$40 \pm 6$
$-\text{CO}_2\text{CH}_3$ (n=15)	0.39	0.34	10	$20 \pm 5$
$-\text{CH}_2\text{Br}$ (n=20)	0.12	0.26	$\sim 0$	$9.4 \pm 2$
$-\text{CH}_3$ (n=17)	-0.37	0.070	$\sim 0$	$1.4 \pm 1$

<sup>a</sup> Values of  $\alpha$  and  $f_0$  are the respective slopes and y-intercepts obtained from linear least-squares fits of the data in Figure 23.

<sup>b</sup> n equals the number of methylene groups in the polymethylene chains.

<sup>c</sup> This column correlates the surface free energies of the different monolayers with the advancing contact angle ( $\theta_a$ ) of water as a probe liquid [ref. 158]. Thus through the Young relation [189], the larger  $\cos \theta_a$ , the greater the surface free energy.

Approximate force constants for normal bending,  $\sim 0.06$  N/m, of triangular  $\text{Si}_3\text{N}_4$  cantilevers were calculated as previously described [148], using physical and material specifications provided by Digital Instruments. The normal force between the tip and sample,  $F_N$ , was estimated from force vs.  $z$ -displacement curves (i.e., force curves). Values of  $F_N$  (i.e., the  $x$ -axis in Figure 26 and Figure 27) represent the total normal force, with  $F_N=0$  nN designated as the point at which the tip “breaks contact” with the surface. Thus,  $F_N$  is the sum of capillary forces, molecular interactions (e.g., hydrogen bonds, van der Waals, etc.), and applied load.

All of the frictional measurements and images were obtained with the fast scan axis perpendicular to the principal axis of the cantilever while systematically varying  $F_N$ , and correcting for subsequent displacements of the tip to insure the same area of the surface was sampled [21]. Frictional forces,  $f$ , were measured from plots of frictional signal vs. lateral displacement during 50 nm trace/retrace cycles (i.e., friction loops [138]) along a single scan line at  $\sim 1000$  nm/s. The sensitivity of the detector to lateral displacements of the tip was determined from the slopes of 5 nm friction loops at the stationary turnaround points [143], and torsional force constants of  $\sim 80$  N/m were calculated by approximating the triangular-shaped cantilever by two parallel beams [148]. Hysteresis in the friction was observed in only a few instances when cycling  $F_N$ ; these scans were not included in the results herein.

The data in Figure 26 were acquired by using the same probe which was cleaned in methanol after examining each surface. Thus, variables like the cantilever force constant and tip structure were fixed. The constancy of the tip composition was verified by repeated measurements of the friction as a function of  $F_N$  at each of the samples. We found, for example, that identical results were obtained for a methyl-terminated sample before and after characterizing a carboxylic acid-terminated sample. Thus, variations in the dependencies of  $f$  on  $F_N$  in Figure 26 can be attributed solely to differences in the composition of the monolayer samples and not to changes in tip composition.

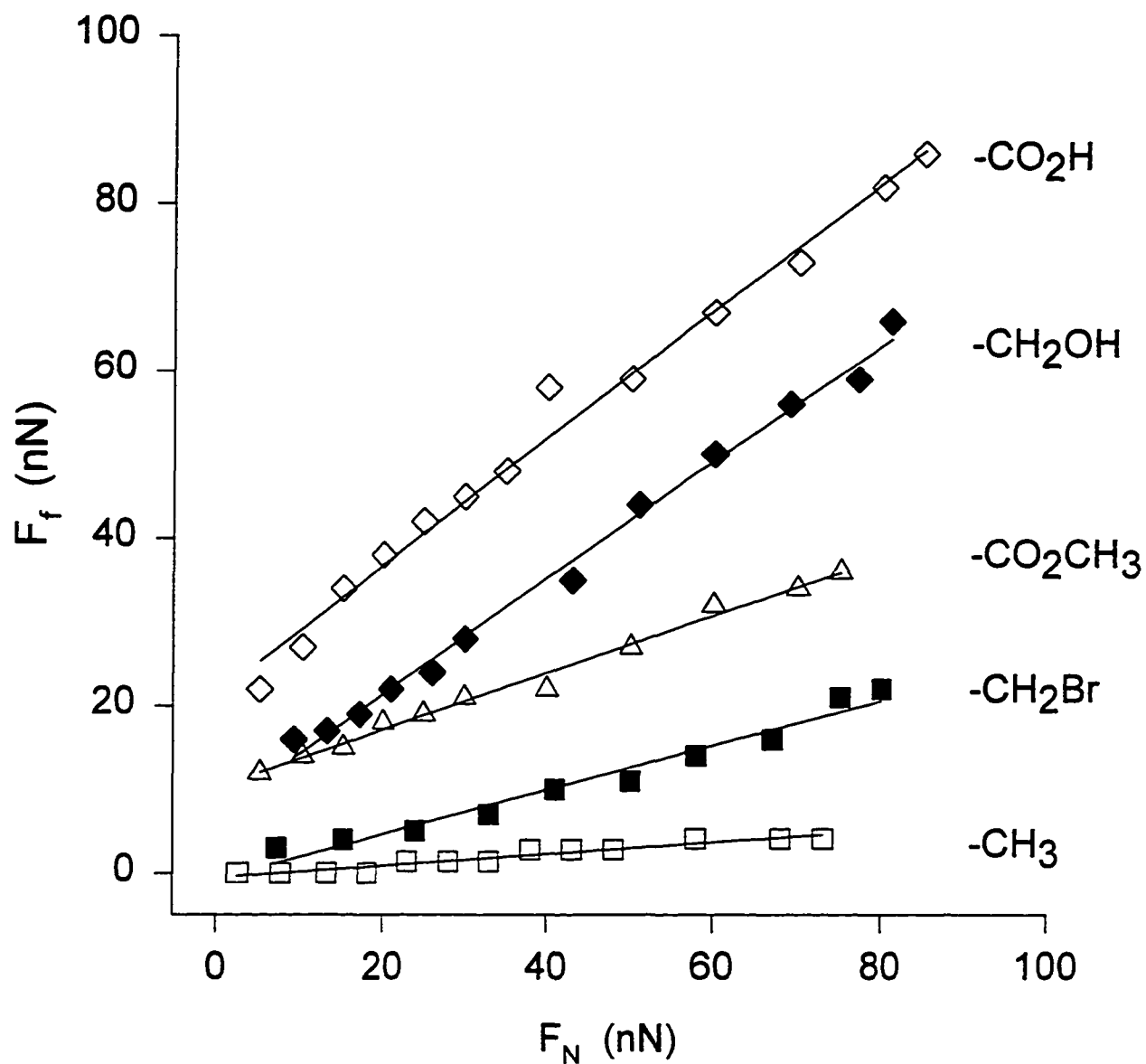


Figure 26 Plots of the frictional force versus normal force for a series of end-group derivatized alkyl thiolate monolayers.

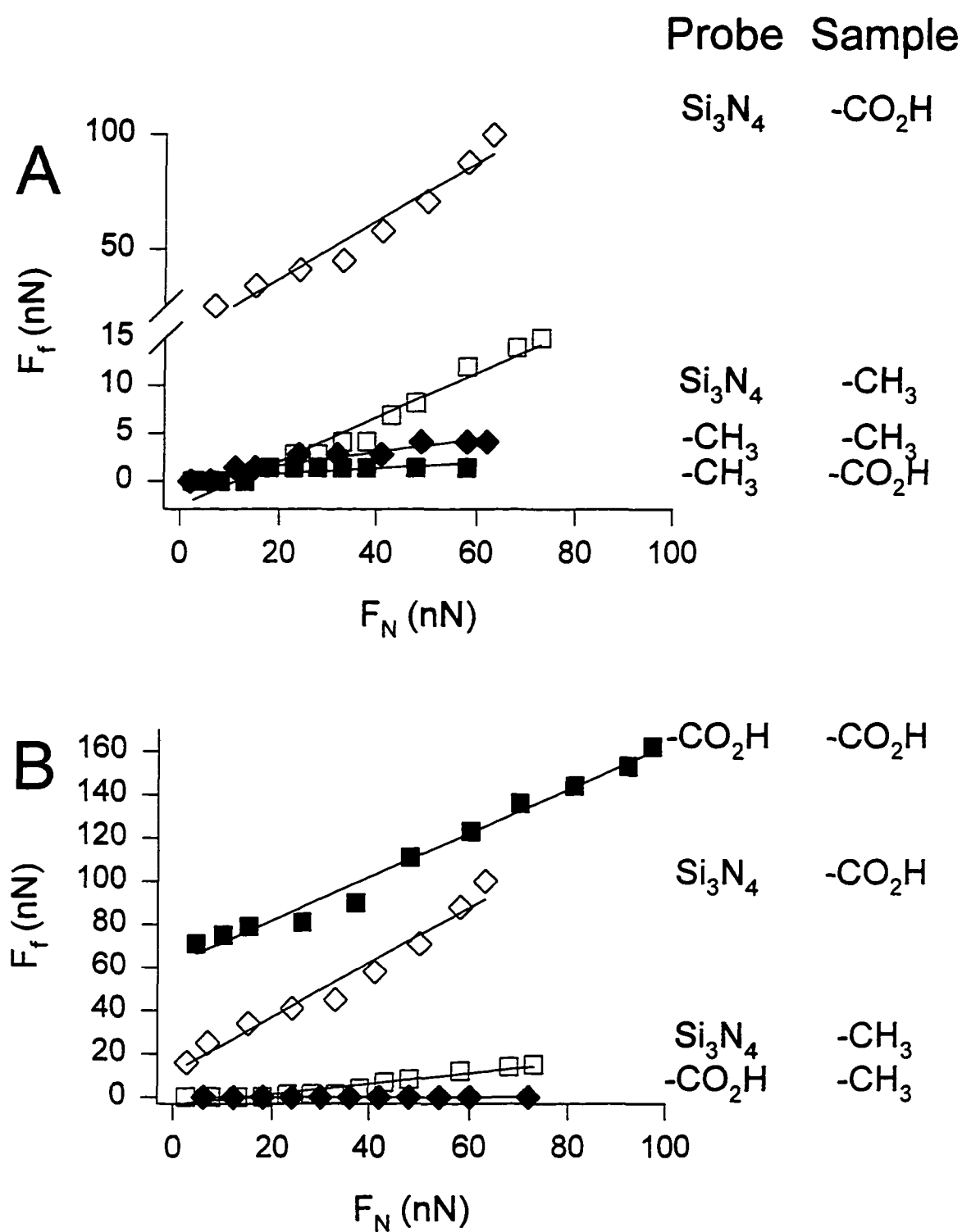


Figure 27

Plots of the frictional force versus normal force for chemically modified probes with methyl and acid terminated alkythiolate monolayers.

### Image Acquisition

All images were acquired in the constant force mode at a  $F_N$  of  $\sim 10$  nN. Topographic and lateral force images were collected concurrently. The instrument was allowed to equilibrate thermally under argon for  $\sim 1$  hr after mounting each sample. Vertical displacements were calibrated using the heights of single atomic steps at Au(111).

### Results and Discussion

The underlying basis for compositional mapping using FFM is the dependence of the frictional interactions at microscopic contact areas on surface free energies [187, 188]. Ideally, the frictional force,  $f$ , of an adhesive contact is a function of the contact load, the area of contact, and surface free energies of the two surfaces [187, 188]. As demonstrated by wettability studies, free energies at smooth surfaces are controlled primarily by the chemical functional groups at the outermost few angstroms of the interface [57, 189]. It follows that a technique which controls the applied load and the area of contact, and provides a determination of  $f$  across an interface can potentially serve as a compositionally sensitive probe for mapping surface functionality [43, 143, 144, 145, 146, 147, 174, 175, 190].

The above assertion is validated by the frictional data in Figure 26. This figure presents  $f$  vs.  $F_N$  plots for the same unmodified tip at several different monolayer-coated substrates. For each sample surface,  $f$  exhibits a linear increase with  $F_N$  that can be described by,

$$f = \alpha F_N + f_0$$

where  $\alpha$  and  $f_0$  are constants that are related to the chemical composition of the interface [125]. This type of linear dependence has been observed for methyl-terminated Langmuir-Blodgett films in several types of frictional characterizations [125, 142, 191] and has been predicted theoretically [157, 192]. The values of  $\alpha$  and  $f_0$  that are obtained from linear least-squares fits of the dependencies of each of the plots are summarized in Table 3. As is evident,  $\alpha$  and  $f_0$  are influenced by the chemical identity of the end-group of the organic monolayer film [193]. Overall, because of the combined effect of these two parameters,  $f$  at



constant  $F_N$  tracks the expected free energy trend of the monolayer-coated surfaces [184]. That is, the higher the surface free energy, as reflected by the contact angle data listed in Table 3, the greater measured friction. These data establish for the first time a clear correlation between AFM measured friction and the free energy of the contacting tip-monolayer interface, providing a basis for compositional mapping.

Figure 27A and Figure 27B are  $f$  vs.  $F_N$  plots illustrating the effect of the chemical modification of the AFM tip on the friction measured at monolayers with either methyl,  $-\text{CH}_3$ , or carboxylic acid,  $-\text{CO}_2\text{H}$ , end groups, i.e., surfaces with vastly different free energies. The tips were also modified with either  $-\text{CO}_2\text{H}$  (Figure 27A) or  $-\text{CH}_3$  (Figure 27B) terminated alkanethiolate monolayers. Frictional data obtained with unmodified  $\text{Si}_3\text{N}_4$  tips are shown for comparison. For all of the tip-sample combinations,  $f$  again exhibits linear dependencies on  $F_N$  which are summarized by the  $\alpha$  and  $f_0$  values in Table 4. For modified tips, the largest  $f$  values are found at the symmetrical acid-acid contact, followed by the symmetrical methyl-methyl contact and lastly, by the asymmetric acid-methyl contacts. The behavior of the unmodified tip is diagnostic of a tip surface with an intermediate surface free energy. The trends evident in these data can be qualitatively explained since frictional force is expected to increase with the work of cohesion ( $W_{co}$ ) in the case of the symmetric contacts and with the work of adhesion ( $W_{ad}$ ) in the case of the asymmetric contact [187, 188]. By definition,  $W_{ad} = \gamma_1 + \gamma_2 - \gamma_{12}$  and  $W_{co} = 2 \gamma_1$ . Based on the  $\gamma$  values of methyl-terminated ( $\gamma_{\text{methyl}}=19 \text{ mJ/m}^2$  [158]) and acid-terminated ( $\gamma_{\text{acid}}\sim 50 \text{ mJ/m}^2$  [194]) alkanethiolate monolayers, the respective  $W_{co}$  values for the symmetric methyl and acid contacts are  $38 \text{ mJ/m}^2$  and  $100 \text{ mJ/m}^2$ . Thus, the trends in our frictional data indicate that  $W_{ad}$  for the asymmetric acid-methyl contact should be  $\sim 38 \text{ mJ/m}^2$  or less. Coupled with the  $\gamma$  values for the methyl and acid-terminated surfaces, the  $W_{ad}$  value yields a lower limit for  $\gamma_{12}$  of  $\sim 31 \text{ mJ/m}^2$ , which is comparable to values found for other highly immiscible systems [195, 196]. Importantly, this analysis further supports that the chemical dependence of friction at these contacts follows predictions from surface free energy considerations.

**Table 4** Values of  $\alpha$  and  $f_0$  for a variety of tip-sample combinations<sup>a</sup>

Tip <sup>b,c</sup>	Sample	$\alpha$	$f_0$ (nN)
Unmodified	-CO <sub>2</sub> H	1.1	10
Unmodified	-CH <sub>3</sub>	0.23	~0
-CO <sub>2</sub> H	-CO <sub>2</sub> H	1.0	62
-CO <sub>2</sub> H	-CH <sub>3</sub>	0	0
-CH <sub>3</sub>	-CO <sub>2</sub> H	0.030	~0
-CH <sub>3</sub>	-CH <sub>3</sub>	0.070	~0

<sup>a</sup> Values of  $\alpha$  and  $f_0$  are the respective slopes and y-intercepts obtained from linear least-squares fits of the data in Figure 27.

<sup>b</sup> Unmodified tips were prepared by washing Si<sub>3</sub>N<sub>4</sub> tips in methanol prior to use.

<sup>c</sup> The designations -CO<sub>2</sub>H and -CH<sub>3</sub> represent the end-groups of the monolayers formed from the corresponding alkanethiols (HO<sub>2</sub>C(CH<sub>2</sub>)<sub>15</sub>SH and CH<sub>3</sub>(CH<sub>2</sub>)<sub>17</sub>SH) that were used to modify the gold-coated sample substrates.

The data in Figure 26 and Figure 27 and Tables 3 and 4 lead to three key conclusions pertaining to compositional imaging. First,  $f$  is strongly affected by the chemical identity of the functional groups at the contacting interface. Second, for a sample composed of both -CH<sub>3</sub> and -CO<sub>2</sub>H end-groups, an acid modified tip (as well as an uncoated tip) should show a much higher frictional imaging contrast (i.e., difference in  $f$ ) relative to a tip modified with a methyl end group. Third, a methyl-modified tip, which exhibits a much smaller difference in  $f$  between the two surfaces, has a slightly larger but clearly detectable  $f$  value at the methyl sample relative to the acid sample. We therefore expect a larger contrast when imaging with either an acid-modified or an unmodified tip, and a much smaller and inverted contrast when imaging with a methyl-modified tip. Our plots also suggest that the two types of end groups can be readily differentiated from each other with a clearly detectable frictional contrast at moderate values of  $F_N$  (e.g., 10-40 nN).

The ability to map interfaces chemically with nanometer-scale resolution as well as to control the contrast of such maps is demonstrated by the combined results shown in Figure 28

and Figure 29. Images using an unmodified tip and a methyl-modified tip are presented. Our test substrates were prepared by exposing an uncoated Au(111) surface to a solution containing both a carboxylic acid-terminated alkanethiol ( $\text{HS}(\text{CH}_2)_{15}\text{CO}_2\text{H}$ ) and stearic acid ( $\text{CH}_3(\text{CH}_2)_{16}\text{CO}_2\text{H}$ ). This process forms a bilayer structure (see inset in Figure 28) via head-to-head hydrogen bonding of the carboxylic acid end groups [185], the extent of which can be altered by manipulating immersion time and concentrations.

Figure 28 contains a set of topographic and frictional force images, with corresponding cross-sectional contours, of two different samples of a spatially segregated, partially formed bilayer structure. As expected, the observed height variations of  $\sim 2$  nm in all topographic images are in reasonable agreement with the height of a single molecular layer of fully extended stearic acid. [197]. Thus, the higher regions in the topographic image arise from the stearic acid layer of the film, i.e., portions of the partial bilayer structure with a methyl terminus, and the lower regions from the underlying thiolate monolayer, i.e., a carboxylic acid terminus. In contrast to the size of the chemically distinct regions previously characterized by friction with SFM [43, 146, 144, 145, 174, 175], the dimensions and separations of the different domains in our test samples are at the nanometer length scale, facilitating an assessment of mapping resolution.

The frictional force images in Figure 28 follow the expected trends evident in the data from Figure 27A and Figure 27B. The image using a hydrophilic, unmodified tip (Figure 28B) shows regions of comparatively high and low frictional forces. Based on the direct correspondence with the topographic profile (Figure 28A), the frictional force differences reflect the contact of a relatively high free energy tip with domains clearly related to two distinct functional groups. That is, the regions of high frictional force arise from contact of the tip with the carboxylic acid functionality at the terminus of the underlying alkanethiolate monolayer and the regions of low frictional force correspond to contact with the terminal methyl group of the top molecular layer of the bilayer structure. Importantly, the dependence of  $f$  on  $F_N$  at the contact between the unmodified tip and the methyl terminated component of the bilayer structure is similar to that observed in Figure 26 for the contact between the

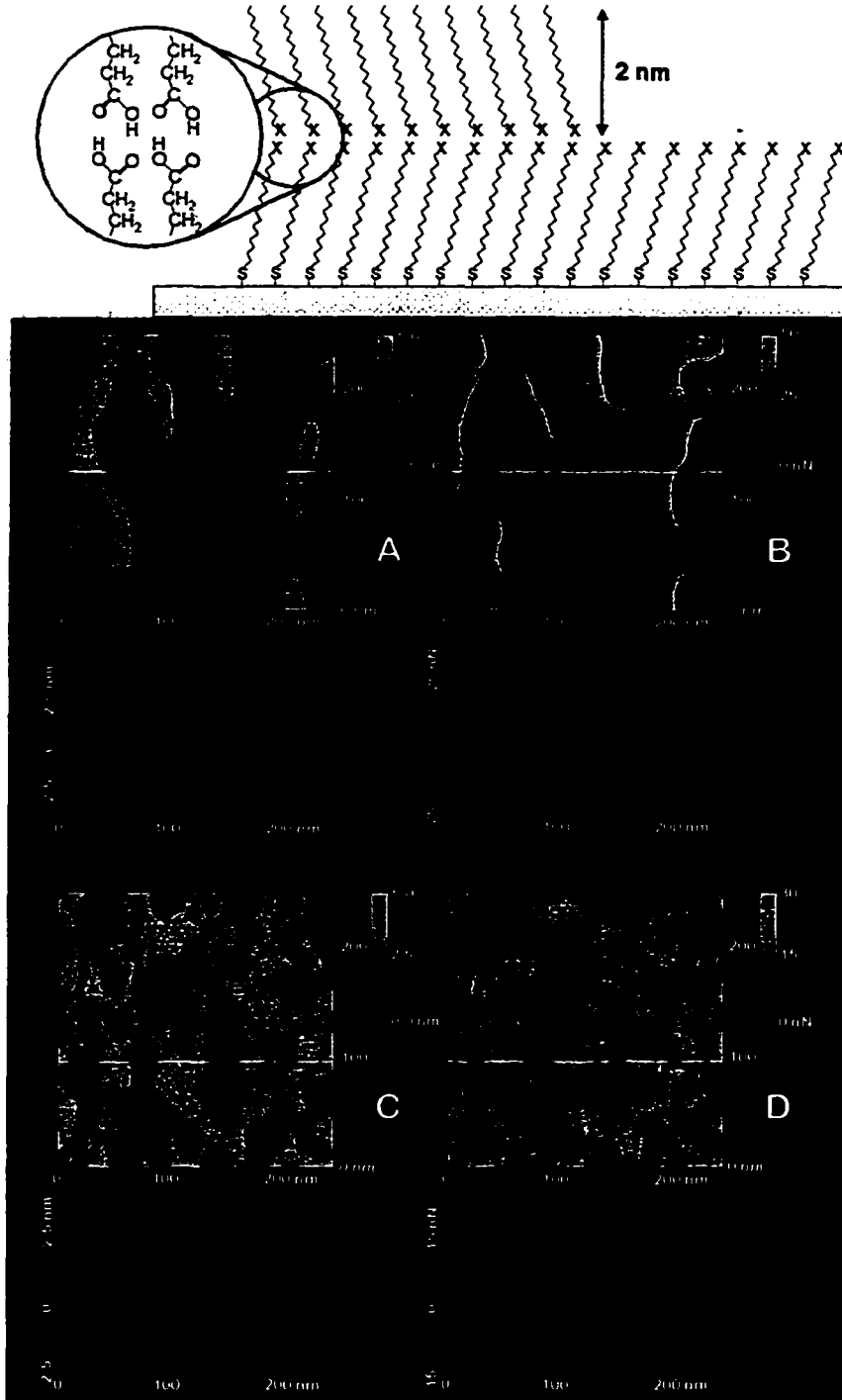


Figure 28

**A and B** show the topography and friction obtained at a mercaptohectadecanoic acid/steric acid bilayer with an unmodified (moderate free energy probe), while **C and D** show the corresponding images obtained with a methylated probe. This demonstrates that the frictional response measured by SFM is critically dependent upon the chemical makeup of the probe.

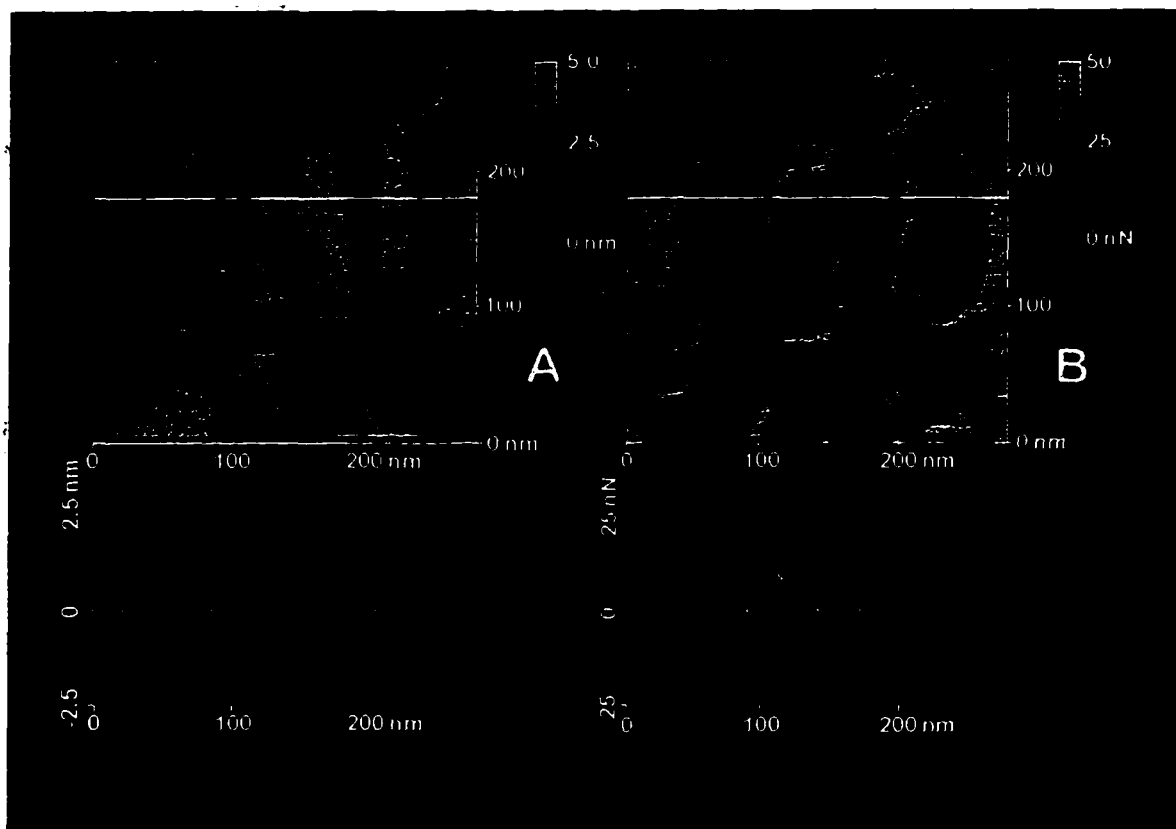


Figure 29

**A** and **B** show the topography and friction obtained at a mercaptohectadecanoic acid/steric acid bilayer which has been machined in such a way as to remove the bilayer and expose the underlying monolayer. Interestingly, it is clearly evident from the frictional image that the bilayer and the monolayer have dramatically different friction behaviors with this probe

uncoated tip and the methyl-terminated monolayer. Thus, the frictional contrast in Figure 28 arises from chemical effects and not from possible packing and hence, elasticity differences [144]. The frictional spikes in the cross-sectional profiles are due to the interaction of the tip with the edge of a bilayer domain [37, 141]. A comparable discussion can be put forth for the image in Figure 28D, which was collected at a similarly prepared sample using a methyl coated tip. In this case, the contrast is diminished and inverted relative to that obtained with the unmodified tip. Thus, regions with a slightly higher frictional force correspond to the methyl terminated layer, whereas those with a lower frictional force arise from the underlying acid terminated alkanethiolate monolayer.

The issue of resolution can be approached in two ways. First, what is the smallest sized domain that can be resolved? Second, what is the minimum distance clearly separating two chemically distinct domains? The FFM images in Figure 28 and Figure 29 provide a basis using both approaches for an assessment of resolution. In Figure 28B, domains of the methyl terminated layer as small as 20 nm in width can be readily distinguished from the surrounding acid-terminated layer. The minimum lateral distance separating one chemically distinct domain from another, as demonstrated by the separation of the cursors in the cross-section of Figure 28B is 10 nm. This separation is well above our pixel width (0.6 nm), validating the asserted resolution.

Additional support for the viability of this chemical mapping approach at nanometer length scales is shown by the images in Figure 29. This figure presents concurrent topographic (Figure 29A) and frictional force (Figure 29B) images of a bilayer sample prepared the same way as that for Figure 28. In this case, however, a complex preselected pattern was drawn into the surface structure by scanning a probe tip repetitively across a bilayered section of the sample a relatively high normal forces (i.e., 80-100 nN). In contrast to the nondestructive situation at lower loads, scanning at these higher loads effectively displaces the more weakly held stearic acid layer in microscopic regions at the surface, leaving voids having a preselected shape in the topmost layer of the bilayer structure. Since the images just prior to application of the high load exhibit a contrast similar to that in Figure 28B, the inversion in the contrast of the frictional image in Figure 29B indicates that this

process effectively converts the unmodified probe tip into a hydrophobic probe tip. Importantly, an analysis of both the topographical and frictional profiles show a resolution of 10 nm. We are currently devising routes for creating samples with small domains that are free of the topographic features of our bilayer samples, which presently limit a more stringent evaluation of the mapping resolution of this technique.

## **Conclusions**

In summary, our results show that the chemical identity of the functional groups at contacting AFM tip/sample interfaces have a profound effect on the resulting frictional force. Since the relative frictional force may be predicted by prior knowledge of the functional group chemistry and assessed at a resolution of ~10 nm, the potential opportunities for the use of chemically modified AFM tips as part of a new form of surface and interfacial chemical analysis spans a wide range of science and technological areas, including biological sequencing, phase segregated polymeric materials and high density data storage devices. We further believe that comparison of the frictional responses in Figure 26 and Figure 27 offers a more direct method for interpretation of frictional images of chemically diverse systems as opposed to recent measurements that correlate adhesion with frictional mapping [146]. Efforts applying this imaging concept to interfacial chemical and electrochemical transformations are underway.

## **Conclusions**

The principle conclusions from this section are that careful interpretation of the material properties may allow the qualitative chemical characterization of interfacial systems. Just as with the material characterizations of the previous section, the development of these techniques requires the characterization of as many different samples as possible. In this way, the full spectrum of responses can be characterized, and a response matrix may be formulated. Additionally, this study demonstrates how SPM can be used in a nanofabrication sense to perform rudimentary steps required for directed synthesis. In this case it has been to expose a reactive site by the removal of a steric barrier, the bilayer, which was inhibiting access of

solution bound species from accessing the terminal groups of the supporting monolayer.

Although these are primitive steps, they point to a direction of future work that will hopefully prove fruitful.



## **REAL TIME *IN SITU* CHARACTERIZATIONS**

The success of the previous two projects, prompted us to examine the temporal evolution of surface reactions. Since SFM is a imaging instrument, it should allow us to monitor the spatial progress of a surface reaction, in situ and in real time. Combined with the extraordinary resolution, this promises to be an exciting set of studies. Since surface reactions often change the chemistry of an interface it was expected that we would be able to monitor changes both in topography, as well as changes in the material properties. We decided upon two surface transformations: a) a chemical reaction, where an ester terminated alkyl thiolate monolayer monitored in situ as it is hydrolyzed from a tall, low free energy, methyl surface to a shorter, high free energy, acid surface; and b) an electrochemical transformations, where a ferrocene terminated alkyl thiolate monolayer is electrochemically transformed from a low free energy, neutral, reduced form, to a high free energy, cationic, oxidized form. Only the electrochemical project will be presented here; however, both have successfully demonstrated the viability of SFM for following chemical reactions in situ and with chemical discrimination.

### **Example Study (Electrochemically Dependent Adhesion)**

This section demonstrates the real time monitoring of the electrochemical transformation of a surface bound redox species using AFM-based adhesion measurements. The measurements were conducted using a monolayer formed by the chemisorption of 11-mercaptoundecyl ferrocenecarboxylate (FcT) at a Au(111) electrode, and a gold-coated probe tip modified with an octadecanethiolate (OT) monolayer. Using this probe tip-sample combination, the one-electron oxidation of the ferrocenyl group of the FcT monolayer results in a decrease in the observed force of adhesion ( $F_{ad}$ ) at the microcontact formed by the two different surfaces. Using surface tension arguments, this change is attributed to the decrease in the effective miscibility at the microcontact as a consequence of the oxidation of the ferrocenyl group to the ferrocenium ion. Issues related to the underlying changes in the interfacial structure that give rise to the differences in  $F_{ad}$  are discussed.

## Introduction

Since its invention in the mid-1980's [5], the atomic force microscope (AFM) has proven invaluable in addressing issues related to the nanoscale topography of a wide variety of interfacial materials [13, 198, 199]. Recent efforts in several laboratories [25, 32, 114, 116, 145, 146, 147, 168, 200, 201, 202, 203], including our own [167], have focused on extending the capabilities of AFM to increase the chemical content gained from the imaging process. Several approaches have been explored, including those based on friction [145, 146, 147, 167, 168] and adhesion [25, 32, 43, 114, 116, 146, 168, 200, 201, 204] measurements. The underlying basis of such measurements is the dependence of both the adhesive and frictional interactions at microscopic contacts on the chemical functional groups at the outermost few angstroms of the two surfaces. Coupled with strategies for the chemical modification of the AFM probe tip, compositional maps of a variety of chemically [146, 147, 167, 168] and biochemically [174, 205, 206, 207] interesting interfaces have been developed, with a spatial resolution as high as 10 nm [167]. Studies using these techniques have also begun to provide new insights into mechanistic issues related to both friction (e.g., lubrication and wear), and adhesion (e.g., antigen-antibody coupling) phenomena.

We demonstrate in this paper the first application of AFM-based adhesion measurements to the real time monitoring of the electrochemical transformation of a surface-bound redox species. These measurements were conducted using a ferrocene-terminated alkanethiolate monolayer chemisorbed at a Au(111) substrate and a probe tip modified with a methyl-terminated alkanethiolate monolayer as our tip-sample combination. With this tip-sample combination, we show that changes in the force of adhesion ( $F_{ad}$ ) can be correlated with the redox transformation of the ferrocenyl group. Issues related to the interpretation of these findings in terms of the underlying basis for the observed adhesion changes are examined and discussed.

## Experimental Section

Sample substrates were prepared by the deposition of 300 nm of gold onto heat-resistant glass (Tempax, Berliner Glas). The probe tips were prepared by the deposition of an

adhesive ~2 nm film of chromium followed by ~20 nm of gold onto silicon nitride cantilevers (Digital Instruments). The probe tips are characterized by a force constant of ~0.06 N/m and a radius of curvature before gold deposition of ~30 nm. The films were deposited in a cryogenically pumped Edwards 306A vacuum chamber at 0.05-0.1 nm/s for chromium and 0.3-0.4 nm/s for gold. Following gold deposition, the sample substrates were oven-annealed at 300 °C for 5 h and then further annealed under a H<sub>2</sub> flame [183]. Details of these procedures have appeared elsewhere [87].

After preparation, both the sample substrates and the probe tips were modified by immersion into dilute (0.1 mM) alkanethiol-containing ethanolic solutions for ~12 h. The probe tip was immersed in an ethanolic solution of octadecanethiol (OT, Aldrich), which had been recrystallized twice from ethanol. The sample substrate was immersed in an ethanolic solution of 11-mercaptoundecyl ferrocenecarboxylate (FcT), which was synthesized as previously reported [208]. Ethanol (Quantum, punctilious grade) was deoxygenated with ultra-high purity (UHP) argon immediately before solution preparation. Prior to imaging, both the samples and the probe tips were rinsed extensively with ethanol and dried under a stream of UHP argon.

A Nanoscope III scanning probe microscope (Digital Instruments) equipped with an in situ cell was used in combination with a CV-27 potentiostat (Bioanalytical Systems) to obtain force curves as the potential applied to the ferrocenyl-modified samples was scanned in a cyclic voltammetric experiment. The electrochemical measurements were carried out using a three-electrode arrangement. To remove any long range coulombic contributions to the measurements, the sample and probe tip were shorted together with a passivated, spring-loaded clip; thus, the sample and probe tip functioned as a single working electrode. A platinum coil served as a counter electrode. An annealed (H<sub>2</sub>-flame) platinum wire acted as a pseudo-reference electrode; all voltages are given with respect to this reference, which is ~+0.6 V with respect to saturated calomel electrode, as estimated from a comparison of positions of the waves for the redox of the FcT monolayer in Figure 30 with earlier reports [208]. The supporting electrolyte was 1.0 M HClO<sub>4</sub>(aq).

Measurements were accomplished by locating a large, atomically flat crystallite on the sample; the sample stage was then positioned to center the probe tip over the crystallite. Adhesion force curves (i.e., probe tip displacement vs. the vertical displacement of the sample stage) were then collected at a vertical displacement rate for the sample stage of 10  $\mu\text{m/s}$  (i.e., 500 nm approach/retract cycles at 10 Hz) as  $E_{\text{appl}}$  was scanned. Each retraction curve was subsequently analyzed to convert the probe tip displacement to  $F_{\text{ad}}$  [28]. The accuracy for each determination of  $F_{\text{ad}}$  was  $\pm 0.1$  nN, while the reproducibility of repetitive measurements at the same value of  $E_{\text{appl}}$  was  $\pm 0.5$  nN. Generally, a few potential cycles were collected to define the upper and lower limits of  $E_{\text{appl}}$  because of the day-to-day variability in the pseudo-reference electrode. Overall, the set-up times (i.e., time required to mount the sample and fill the AFM electrochemical cell with electrolytic solution, allow for instrumental thermal equilibration, and determine potential scan limits) were typically a few hours.

## Results and Discussion

Figure 30 presents the cyclic voltammetric current-potential (i-E) curve for the oxidation and reduction of a gold-bound FcT monolayer mounted in the electrochemical cell of the AFM. This curve was obtained after four cycles of applied potential ( $E_{\text{appl}}$ ) at 10 mV/s and a potential window between -0.47 V and +0.25 V. As observed previously [208], the i-E curve has an asymmetric shape on both the anodic and cathodic scans [209]. The separation of the cathodic and anodic peak potentials is  $\sim 10$  mV, which is consistent with the expectation for the electrochemical transformation of an immobilized redox species [210]. We note that the repetitive cycling between these limits of  $E_{\text{appl}}$  results in the slow degradation of the electroactivity of the FcT monolayer through the well-established decomposition of ferrocenium ions in solutions of even mild nucleophiles like perchlorate ion [211].

A series of force curves were also obtained during the cyclic voltammetric scan in Figure 30 at a collection frequency of 0.97 Hz. Coupled with the 10 mV/s scan rate, the

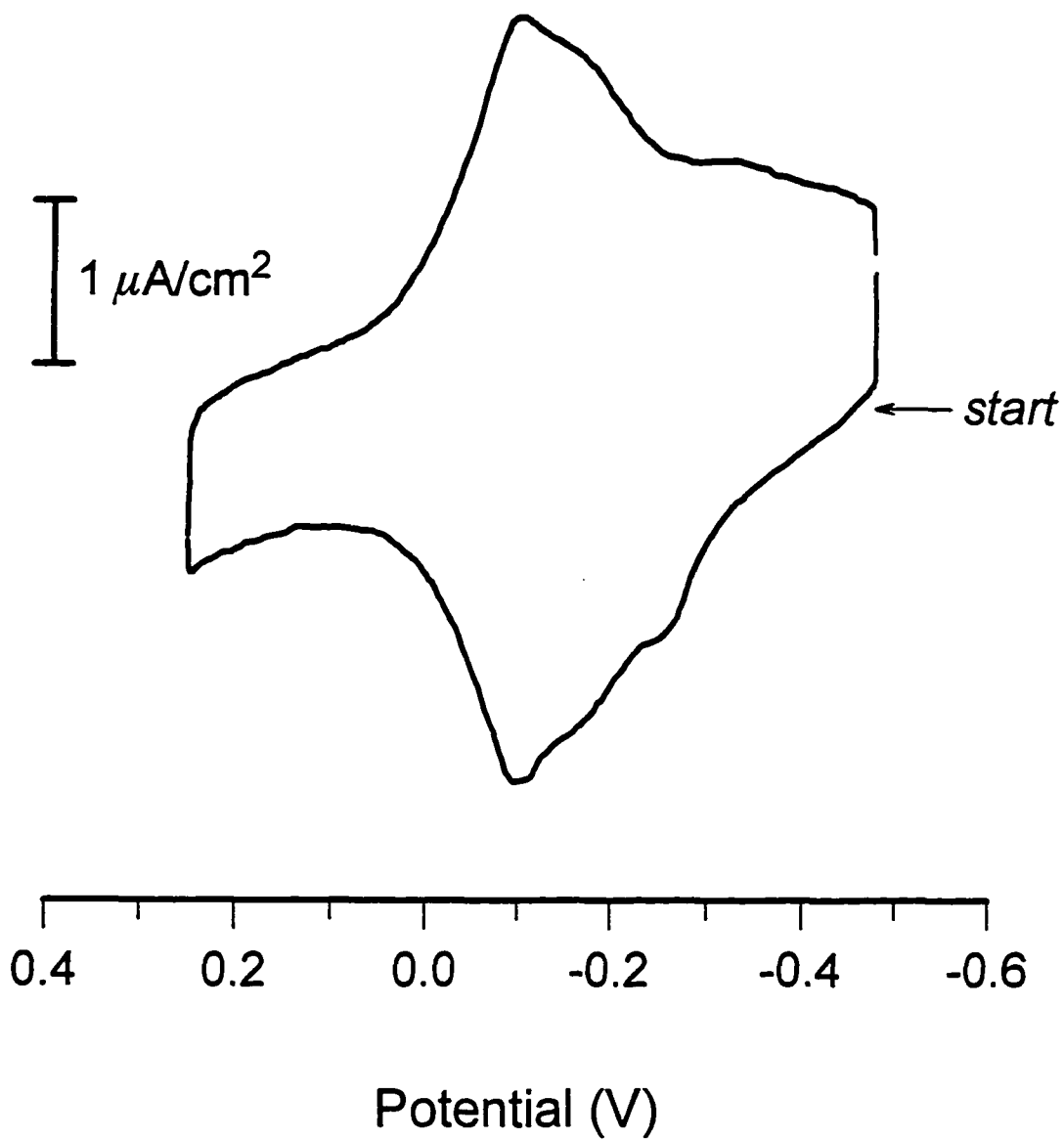


Figure 30 Cyclic voltammogram for a ferrocene monolayer in the SFM in situ cell, at a scan rate of 10 mV/s with a Pt counter electrode and a Pt reference electrode in 1M HClO<sub>4</sub>.

collection frequency yielded 150 force curves for the full potential cycle. A representative set of these data is presented in Figure 31. The series of force curves on the left-side of the Figure were obtained on the anodic scan at -0.47, -0.37, -0.13, -0.09, -0.04, +0.11, and +0.20 V; whereas those on the right-side were collected during the subsequent cathodic scan at +0.20, +0.11, -0.04, -0.09, -0.13, -0.37, and -0.47 V. At the early stages of the anodic scan, the force curves (i.e., the force curves at -0.47 and -0.37 V) remain effectively unchanged. The lack of change is consistent with the lack of a detectable oxidative conversion of the ferrocenyl group at these values of  $E_{\text{appl}}$  (see Figure 30). As the anodic scan continues, however, a notable decrease in the translation distance of the sample stage was required to rupture the contact between the probe tip and sample surface is observed (i.e., the force curves at -0.13, -0.09, and -0.04 V). These decreases indicate that  $F_{\text{ad}}$  decreases as the reduced form of the ferrocenyl group is gradually converted to its oxidized form. Near the end of the anodic scan, the decrease reaches a limiting value (i.e., the force curves at +0.11 and +0.20 V), representative of the exhaustive conversion of the ferrocenyl group to its ferrocenium form.

Upon the reversal of the scan direction, the changes in the force curves on the right-side of Figure 31 qualitatively follow the dependence for the anodic scan. That is, the force curves for the cathodic scan exhibit a notable change only after  $E_{\text{appl}}$  reaches a value sufficient to induce the reduction of the oxidized ferrocenium ion. Furthermore, the force curves near the end of the anodic scan approach those observed at the beginning of the cathodic scan.

A more detailed summary of the dependence of  $F_{\text{ad}}$  on  $E_{\text{appl}}$  is shown in Figure 32a. This Figure is a plot of  $F_{\text{ad}}$  for all of the force curves taken during the voltammetric scan. Thus,  $F_{\text{ad}}$  cycles from an average of 7.6 nN at the beginning of the anodic scan, decreases to ~1.2 nN near the end of the anodic and the beginning of the cathodic scan, and returns to an average of 6.4 nN at the completion of the cathodic scan. The following examines these data in more detail

The correspondence of the changes in  $F_{\text{ad}}$  and the redox conversion of the FcT monolayer is more firmly established by a comparison of the data in Figure 32b with that in Figure 32a. Figure 32b is a plot of the fractional surface concentration ( $\phi$ ) of the reduced

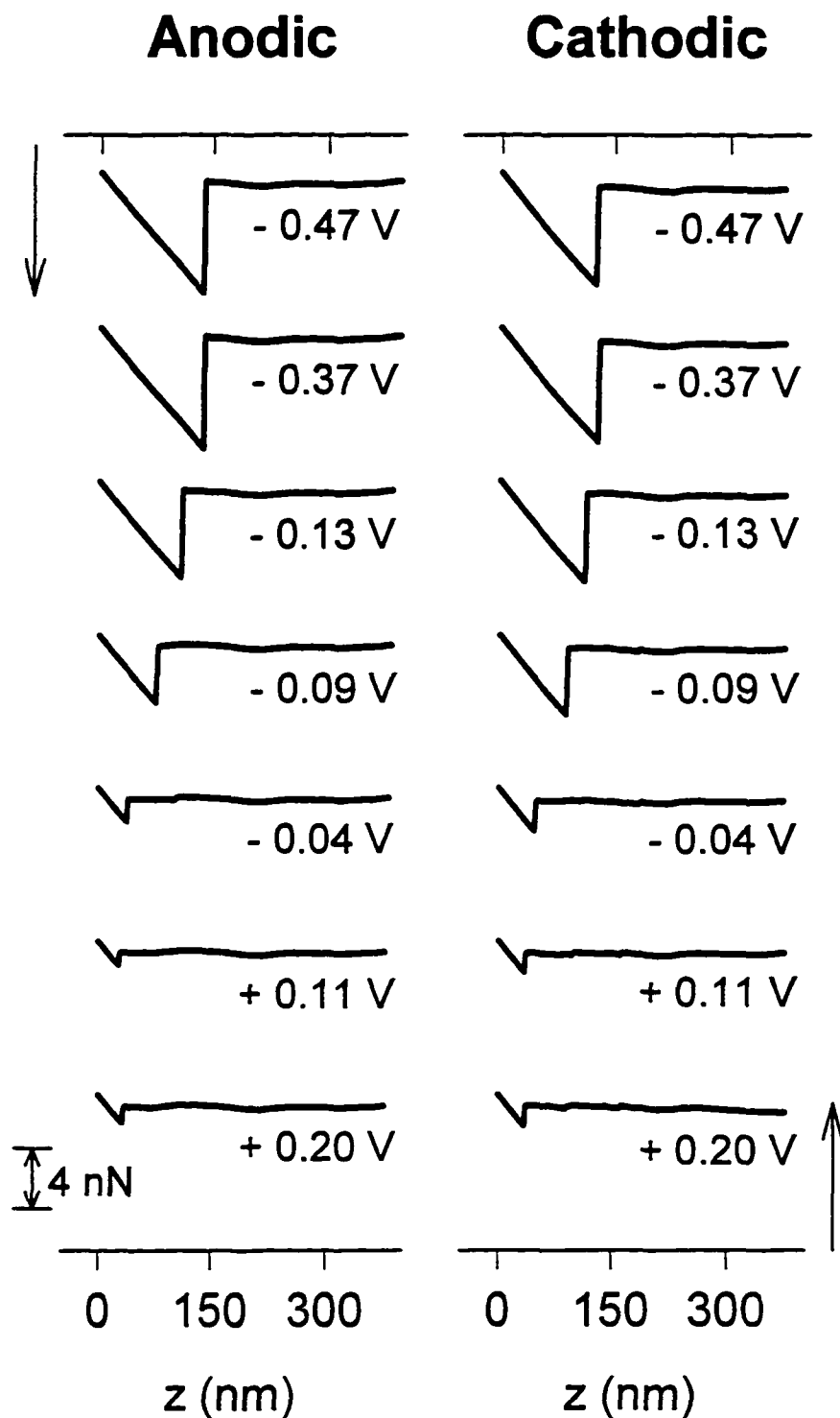


Figure 31 Force curves taken with an octadecanethiolate modified probe at a ferrocene monolayer insitu as the potential was swept through a cyclic voltammogram.

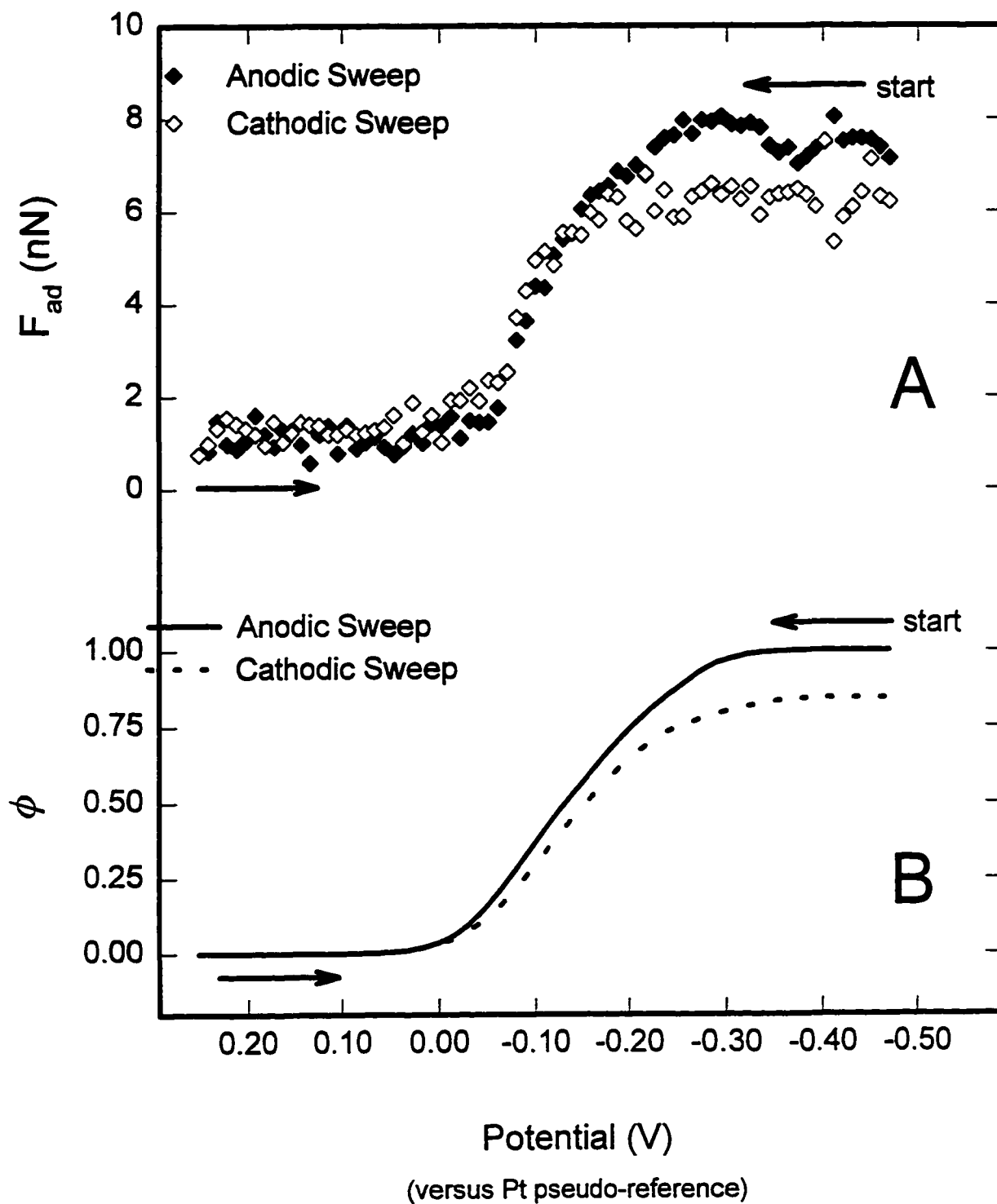


Figure 32

A comparative plot of both the electrochemical charge and the adhesive force as functions of potential. This demonstrates a clear correlation between the electrochemical state of the monolayer and the adhesion measured by the SFM.



form of the ferrocenyl group as a function of  $E_{app}$  for both the anodic and cathodic scans. This curve was calculated, after estimating the charging current contribution by a baseline approximation for both scans, by integrating incrementally the areas under both components of the  $i$ - $E$  curve in Figure 30. A comparison of the data in Figure 32a and Figure 32b yields three interesting observations. First, and most importantly, the general similarities of the sigmoidally shaped curves for  $\phi$  and  $F_{ad}$  confirm that the change in  $F_{ad}$  is a consequence of the redox transformation of the ferrocenyl group. Indeed, scans over the same potential range using a sample modified with OT do not show a detectable change in  $F_{ad}$ . Second, a decrease in  $F_{ad}$  is detected only after the conversion of  $\sim 10$ - $20\%$  of the ferrocenyl group between its two forms. This finding offers a rough estimate for the detection capability of AFM-based adhesion measurements for redox transformations in the FcT monolayer. Third, there is a small, but definite hysteresis in  $F_{ad}$  because of the voltammetric scan. Although a contribution from a structural reordering at the FcT interface may be possible, we presently ascribe the decrease largely to the aforementioned compositional instability of the ferrocenyl group upon its oxidation. This assertion is supported by decrease in  $\phi$  after completion of the voltammetric scan, and by similar correlations of data collected for samples subjected to a few more voltammetric cycles. Interestingly, a collection of such data shows a clear tendency for a continual decrease in  $F_{ad}$  at the end of the complete cycle. Investigations to establish a more detailed description of the long term tendency are planned.

The most prominent feature of Figure 32a is the dramatic difference in  $F_{ad}$  at the two potential limits. We attribute this observation to miscibility differences between the methyl terminated probe-tip and the two different states of the ferrocenyl monolayer. This assertion follows from our earlier treatment of the differences in the frictional force observed for a series of probe tip-sample combinations [167]. The basis of our treatment rests with an analysis of the work of cohesion ( $W_{co}$ ) for symmetric contacts (i.e., a contact formed by a probe tip and sample substrate modified with methyl-terminated alkanethiolate monolayers) and the work of adhesion ( $W_{ad}$ ) for asymmetric contacts (i.e., a contact formed by a probe tip modified with a methyl-terminated alkanethiolate monolayer and a sample modified with a carboxylic acid-terminated alkanethiolate monolayer (or vice versa)). Thus, the smaller frictional force found

at the asymmetric methyl-carboxylic acid contact with respect to the symmetric methyl-methyl contact [167] is a result of  $W_{co} > W_{ad}$ . In other words, since  $W_{ad} = \gamma_1 + \gamma_2 - \gamma_{12}$  and  $W_{co} = 2\gamma_1$ , ( $\gamma_1$  is the surface tension for one of the two contacting surfaces,  $\gamma_2$  is the surface tension of the other of the two contacting surfaces, and  $\gamma_{12}$  is the interfacial surface tension), the values of  $\gamma_{12}$  required to fit  $W_{co} > W_{ad}$  are consistent with those found for a wide range of highly immiscible fluids [195, 196]. The results of AFM-based adhesion measurements at these types of probe tip-sample combinations [146, 168] support our analysis.

The above treatment can be extended to explain the trend for  $F_{ad}$  in Figure 32a. In this case, however, the two sets of contacts are formed by two different asymmetric probe tip-sample combinations. As discussed, Figure 32 shows that  $F_{ad}$  is greater when the ferrocenyl group is in its fully reduced form than when in its fully oxidized form. In this case, one can readily assert that the surface tension for the cationic (i.e., oxidized) form of the ferrocenyl group will be greater than that for its neutral (i.e., reduced) form, an assertion supported by a recent exploration of the electrowetting of a monolayer formed at gold from 15-(ferrocenylcarbonyl)pentadecanethiol [212]. This study found that the advancing contact angle ( $\theta_a$ ) for water decreased from  $71^\circ$  to  $43^\circ$  upon the oxidation of the ferrocenyl group; comparatively, a study of the electrowetting of a monolayer formed from OT reported a change in  $\theta_a$  of only a few degrees ( $115^\circ$  to  $113^\circ$ ) over the same range of  $E_{app}$  [213]. The oxidation of the ferrocenyl group therefore results in a surface that is notably more hydrophilic after its transformation. As a consequence, the increased difference in  $\gamma_1$  and  $\gamma_2$  at the microscopic contact causes a decrease in miscibility, leading to a decrease in  $F_{ad}$ . This analysis also suggests that the bound product of the degradation of the ferrocenyl group is more hydrophilic than the reduced form of the ferrocenyl group and perhaps more hydrophobic than the oxidized ferrocenium ion.

The above analysis provides an explanation for the change in  $F_{ad}$  that results from the redox conversion of the FcT monolayer from an energetics perspective. It is at present, however, unclear whether the change can be ascribed to the surface tension differences because of the transformation of the ferrocenyl group, to the incorporation of a perchlorate counter ion and water into the surface structure, or to a combination of both [214]. We

suspect that both pathways play a role since the oxidation of the ferrocenyl group increases its polarity [212] and ferrocenium ion forms a strong ion pair with perchlorate ion [215]. The unraveling of the importance of the two pathways awaits a study of the dependence of  $F_{ad}$  using different supporting electrolytes (e.g.,  $PF_6^-$ ).

## Conclusions

We have shown that adhesion-based AFM measurements can be used to follow the electrochemical conversion of an electroactive organic monolayer film chemisorbed on a gold substrate. The results indicate that the value of  $F_{ad}$  at the microcontact formed between a methyl-modified probe tip and a ferrocenyl-modified Au(111) electrode decreases as the ferrocenyl group is converted by a one-electron reaction from its reduced to its oxidized form. This decrease is consistent with an increase in the interfacial surface tension at the microcontact, inducing a decrease in miscibility and therefore a decrease in  $F_{ad}$ . Experiments to determine whether the change in  $F_{ad}$  reflects the surface tension differences that are induced by the transformation of the ferrocenyl group, the uptake of perchlorate counter ions and water at the interface, or a combination of both are planned. We are also exploring the use of redox transformable probe tips to AFM-based compositional mapping strategies as well as attempting to determine why preliminary experiments using frictional force microscopic measurements did not show a detectable change upon the redox transformation of the ferrocenyl group.

The conclusions from this section are that these techniques can be used to monitor the progress of electrochemical reactions in situ. The future prospects for this research are bright, and additional possibilities for electrochemically switchable cantilevers appear quite promising. It seems that the applicability of these techniques covers an ever increasing range. The molecular scale monitoring of chemical and electrochemical processes with chemical discrimination is a powerful tool, which if properly developed might usher in a new era of device characterization and fabrication.

## GENERAL CONCLUSIONS

The single most significant conclusion from these investigations is that SPM is a powerful and versatile tool which will undoubtedly play a crucial role in the development of the next technological era. More directly however, there are some specific conclusions drawn from each of the four projects presented herein.

Although the first project is titled *structural characterizations*, the conclusions deal more with the use of structural information to understand the more complex dynamics of electrochemical interfaces. While molecular-scale defects are critically important to the next wave of nanotechnology, they are also exceedingly important to virtually every technological field at present from microelectronics to electrocatalysis. Without SPM techniques the exact structure of these small defects would remain hidden and speculative open only to indirect probes which often average effects over macroscopic areas. Our group, has been and still is interested in the control and characterization of molecular-sized architectures, and in an effort to use these SAMs as test interfaces at which to construct these architectures, we were faced with the enigma that the smoother and more defect free we made the substrate the more defective these monolayers behaved, electrochemically. The structural information produced by SPM guided the creation and development of models which eventually offered an explanation to this counter-intuitive enigma. We concluded that although there are more defects present at the rougher substrates, they are generally smaller than those found at the smooth substrates, and that it is these few larger defects which cause the monolayers formed at the smoother substrates to have such comparatively poor barrier properties. This is just one example of how structural information gleaned from SPM can assist in understanding complex interfacial properties, like heterogeneous electron transfer.

In order that SPM be as widely applicable to the diverse complicated systems found in technology today as well as in the future, we must develop a theory which allows SPM responses to be translated into compositional, and perhaps even compositionally identifying, information. Unfortunately as is the case with many probes, the SPM responses do not produce a one-to-one mapping to specific materials, and thus we may expect an semi-

empirical theory at best which is full of assumptions and conditions. In the mean time our course of action has been to examine as many different test materials as possible, in an effort to at least construct a sample-SPM response matrix. When performed in a systematic way this may offer access into the kinds of information which may be gleaned from material measurements made with SPM. Both the *material characterization* and *chemical interpretation* projects are concerned with these kinds of systematic investigations at the familiar alkyl thiolate SAM test-structures. In the material characterization project we systematically varied the length of the molecule. We observed that the frictional response of the SPM is dramatically affected by the chainlength of the monolayer precursor, and we concluded, from a comparison with infrared data, that this effect is correlated with how ordered the monolayers are, which is related to inter-chain as well as intra-chain interactions. Based upon the transition which occurs at medium chainlength thiolates, it seems that there are at least two modes of frictional dissipation, one which involves a more or less simple compression of the well packed long chain-length molecules, and another that involves the reorganizational ordering of the semi-random short chain-length molecules.

These results are critical if we are to attempt to make chemical interpretations of the surface composition based upon SPM responses. Since frictional response is based upon the interaction of a probe with a sample its measurement is expected to depend upon the chemical functional groups present at the two surfaces. This project again took a structured approach by examining a wide range of end-group derivatized thiolate monolayers of similar chain-lengths, thus most of the variation in SPM response is expected to arise from the interactions between the chemistry on the probe and the chemistry of the different surface bound end-groups. These results compared qualitatively with values predicted from free energy arguments. Both for unmodified as well as for modified probes. However, it must be stressed that the applicability of these kinds of interpretations are highly dependent upon the material properties of the sample. As seen in the material characterization project, variation of the chain-length easily changes the SPM response by more than any free energy explanation can account for.

In an additional effort associated with the chemical characterization, the SFM probe was used as a nano-patterning device. Although this was by no means the smallest or most precisely controlled patterning device, it had the effect of producing a chemically significant result. The pattern was chemically inhomogeneous, in fact it could perhaps even be used as a reactive site, thus allowing for directed synthesis. A small portion of a molecular assembly may be made accessible to solution bound reactants while the rest, unprocessed by the SPM, remain unreacted. Our experiments demonstrated that SFM may be used to create and then characterize chemically inhomogeneous nano-patterns.

Finally the real-time monitoring of electrochemical transformations are a culmination of these works, in that it takes the step to systems that are dynamically evolving, and applies the SPM probe to monitor that evolution, it was shown that the behavior was consistent with that seen in the chemical interpretation section, although the system is clearly more complicated and less well controlled as the previous projects. But that's the point, the applications of SPM should begin with the formulation of a SPM response matrix for a full range of chemically disparate surfaces under a similarly disparate set of environments so that the techniques may be applied to the complicated unknown world to be used in a critically analytical function to further understand these complex systems.

In conclusion, this dissertation demonstrates that application of SPM to the creation and characterization of molecular sized architectures is both possible and should soon to be a crucial component of the next step of technological advancement. The step to the nanotechnological realm will not be made without the SPM, and the work presented above is a small but clear step in the direction that will eventually lead to such goals.

## FUTURE DIRECTIONS

Although the results of the projects included in this dissertation represent a step in the right direction, their completion has left many questions yet to be answered, as well as many future research opportunities open to investigation. One clear project would be the systematic examination of a broad array of interfaces with a wide range of different probes. This may be accelerated by the development of micro electrode arrays in which each array element is individually addressable, this opens up the opportunity to examine a large number of different samples under very similar environmental conditions, and with the same probe. Additionally, ongoing efforts at other laboratories are attempting to refine parallel arrays of probes, simultaneously characterizing different locations on a sample. The combination of sample array with these parallel probes could dramatically accelerate the development of SPM as a material/chemical characterizational tool. Another possibility, which has been attempted in our laboratory, is to electrochemically control the SFM probe itself. This might allow the user to modulate the chemistry of the probe, and thus access interactional information that is different from the non-electrified probe. Thus a molecular region may be characterized with a single probe with a fixed environment, morphology, etc., which has two different chemistries. I have only concentrated on friction, adhesion, and in passing on elasticity; however, non-contact methods which correlate the probe oscillation phase with respect to the drive signal, have proved highly sensitive to surface composition. The possible future applications of this newer contrast mechanism will no doubt be promising.

The use of bilayer substrates which contain masked reactive groups may provide useful in the creation of nanometer-scale arrays of specific molecules. By using the SPM to create 0- or 1-dimensional reactive patterns, it is conceivable that molecular arrays and otherwise untenable molecular synthesis may be performed by a directed synthesis route at the surface with the probe acting as a kind of catalyst. What is clear is that SPM technologies are going to be critical to future developments, as well as current characterizations, and that there is a wide open field of research opportunities which appear promising and lucrative. As we examine the world around us, it becomes apparent that many of the dominant interactions

occur at or across interfaces. The development of tools that can characterize and control interfacial processes at or even near a molecular-scale is clearly an important venture, and one which I intend to pursue.



## APPENDIX: COMPREHENSIVE LISTING OF DEFECT MODELS

This appendix is a compendium of all the defects considered for the conclusions in the counter-intuitive section. They are included both for completeness, and to clarify the kinds of defects considered. As a reference, it is often clearer to have a complete set of visual models to compare. In this way, the measurements and the conclusions based upon them may be made more readily apparent. The organization of these figures follows along with the development of the models, beginning with models for the substrates, followed by models for the adsorbate packing at those modeled substrates, and concluding with a tabular listing of all the defects considered and their characteristic sizes and fractional coverages. A short guide is included, along with detailed descriptions in the captions of each figure.

The substrate models are basically concentrated on the rough unannealed samples, because the annealed substrate is simply a plane of Au(111) free of topography. Thus, the first few figures depict the progression of the rough unannealed substrate from the real images, Figure 33; to the top of a sphere; to a stepped sphere Figure 34; to stepped sphere with 12 principle step directions Figure 35 and Figure 36. Since these are steps with atomic dimensions it is necessary to consider the discrete step widths, ( we limited the model to the first four steps along each direction) Figure 37, Figure 38, Figure 39, and Table 5. These step widths allowed for a close approximation to the top of a sphere Figure 40. With all of the steps determined, we were able to calculate how much of each step was present per unit area of the hill Figure 41. From a histogram of step widths it becomes apparent that by far most of the steps are quite narrow, too narrow in fact to fit more than two thioliates perpendicular to the step Figure 42. many of each step.

The adsorbate models begin with the easier flat hexagonal Au(111), once one thiolate adsorbs at a three-fold hollow it defines a registry with respect to which all other thioliates will adsorb Figure 43. As the domains grow into each other domain boundaries may conceivably form along any direction at all, our model is limited to the Au nearest neighbor and next

nearest neighbor directions Figure 44. The next set of figures depict the placements of thiolates at the 12 possible domain boundaries along these two directions Figure 45, Figure 46, Figure 47, and Figure 48. The inhomogeneity of thiolate binding sites at the rough stepped surface, leads to a different approach for the adsorbate patterns Figure 49, Figure 50, and Figure 51. Basically the thiolates are placed as tightly as possible without violating the van der Waals diameters of the methylene chains, while still placing the Au-S bond in three-fold hollows, typically along the step edge (five-fold hollows). Finally, Table 6 shows a comparison of the defects at the steps and the terraces 23. The key parameters are  $f_i$  and  $a/l_i$ . As they represent the fractional area exposed by the defects with size (exposed area per unit defect length) respectively.

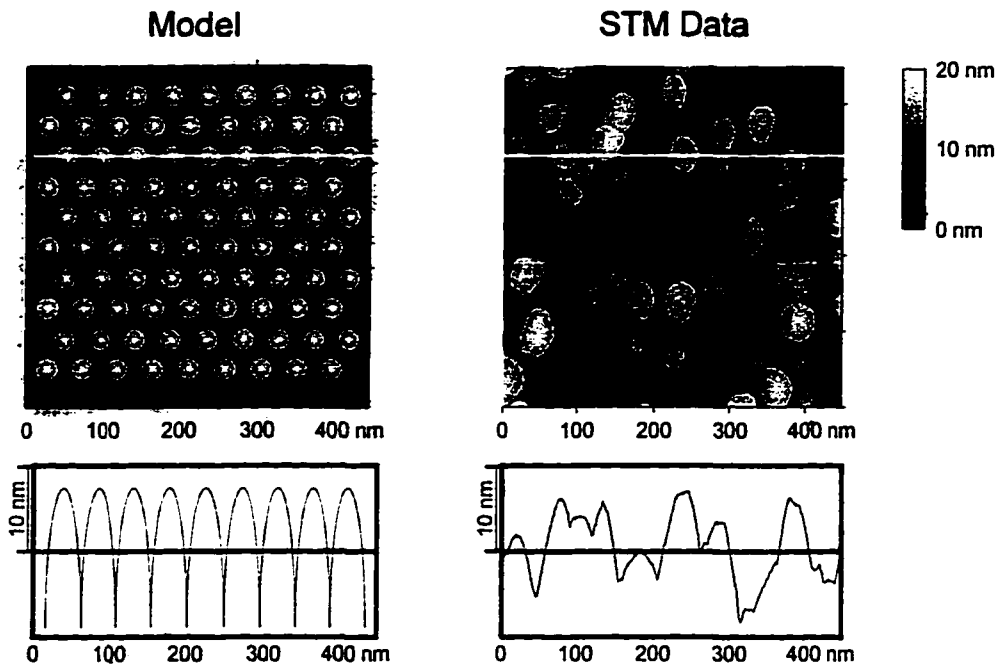


Figure 33

The rough hilly topography of the unannealed gold substrates can be approximated with an array of hills as shown in this figure. Following examination of numerous images, an average hill height and radius were computed to be 18 and 36 nm, respectively

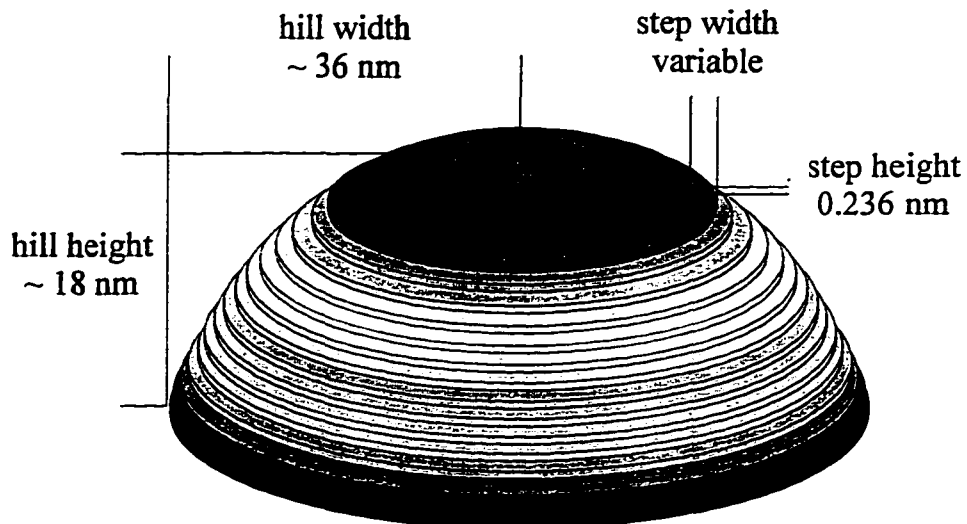


Figure 34

In order to fit these dimensions (18 and 36 nm) we used the top 18 nm of 45 nm radius spheres. However; since these hills are made up of gold atoms, these 18 nm high hills are composed of 77 Au(111) steps (each with heights of 0.236 nm).

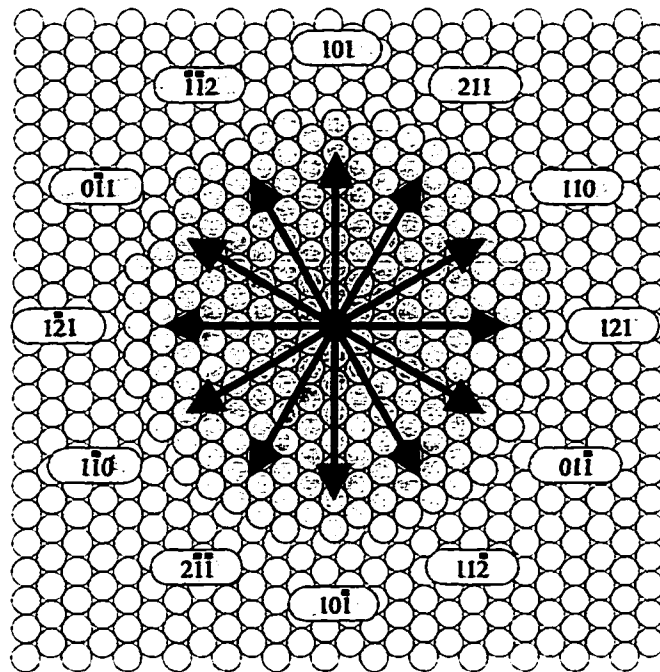


Figure 35

In an effort to refine the model, the circular steps were faceted 12 of low index directions. This results from the relative size of the hills with respect to the constituent atoms. In addition by limiting the allowed steps to these 12 directions the model is more tractable.

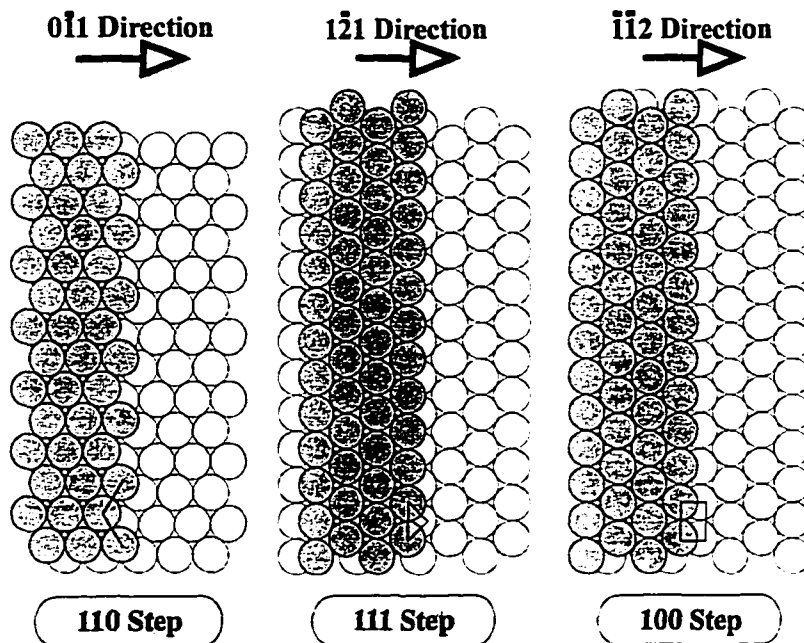


Figure 36

Fortunately, these 12 directions produce basically three kinds of steps.

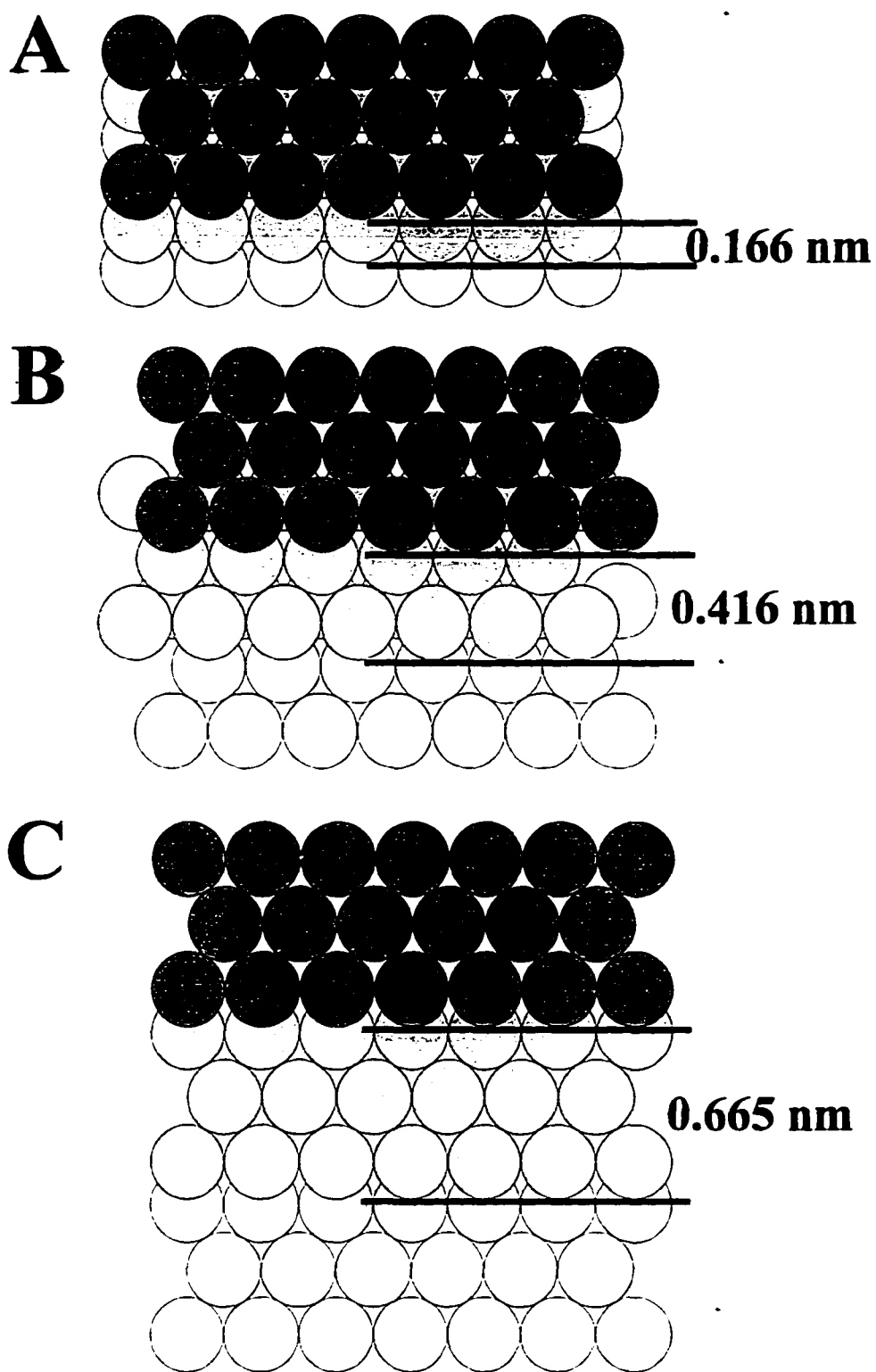


Figure 37

The step widths are not arbitrary. There are certain discrete values allowed by the crystalline packing of the Au lattice. This figure illustrates the first three steps in the 100 direction. A. is actually the 100 face, while B. is the 200 face and C. is the 300 face.

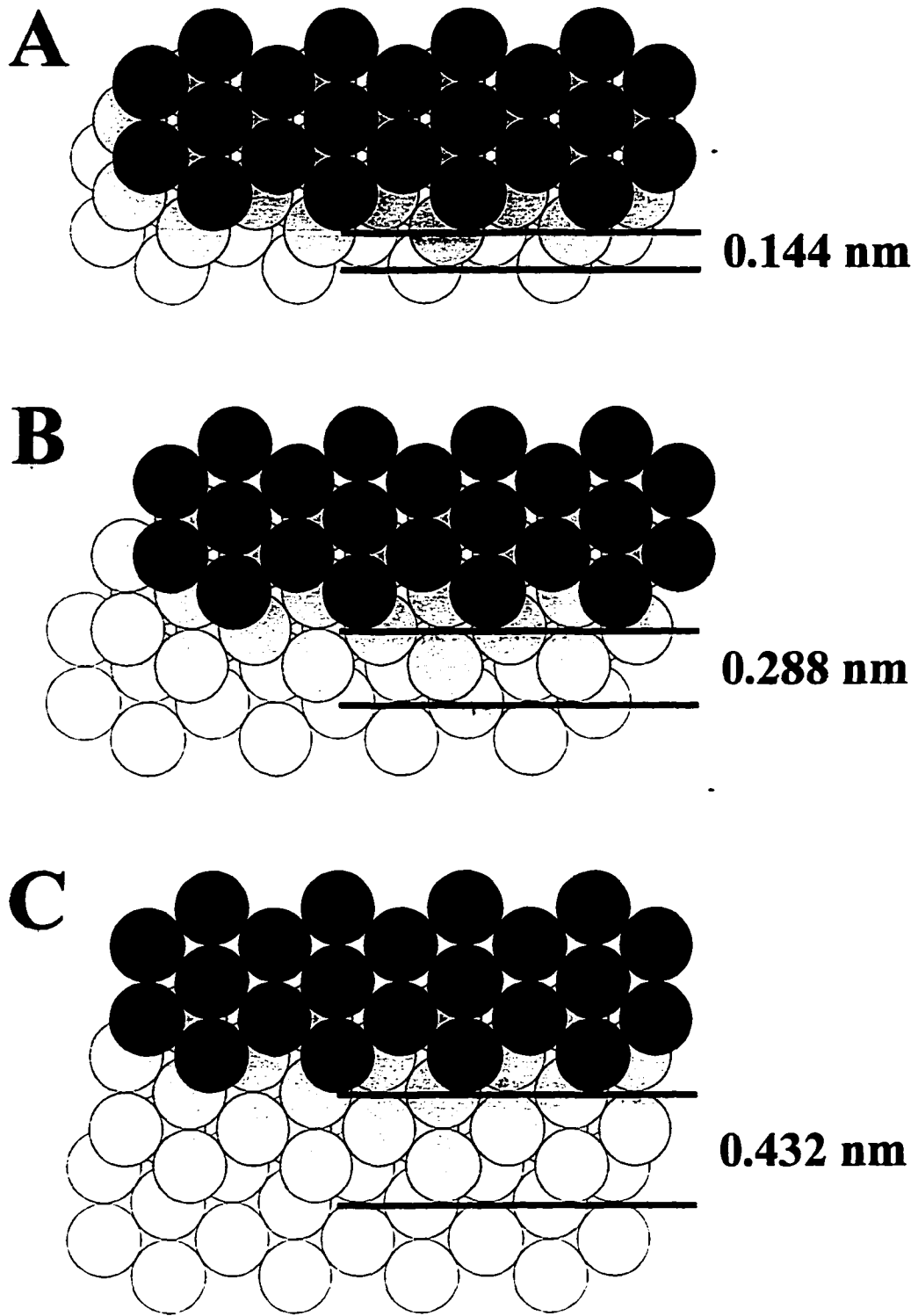


Figure 38

110 steps: A. is actually the 110 face.

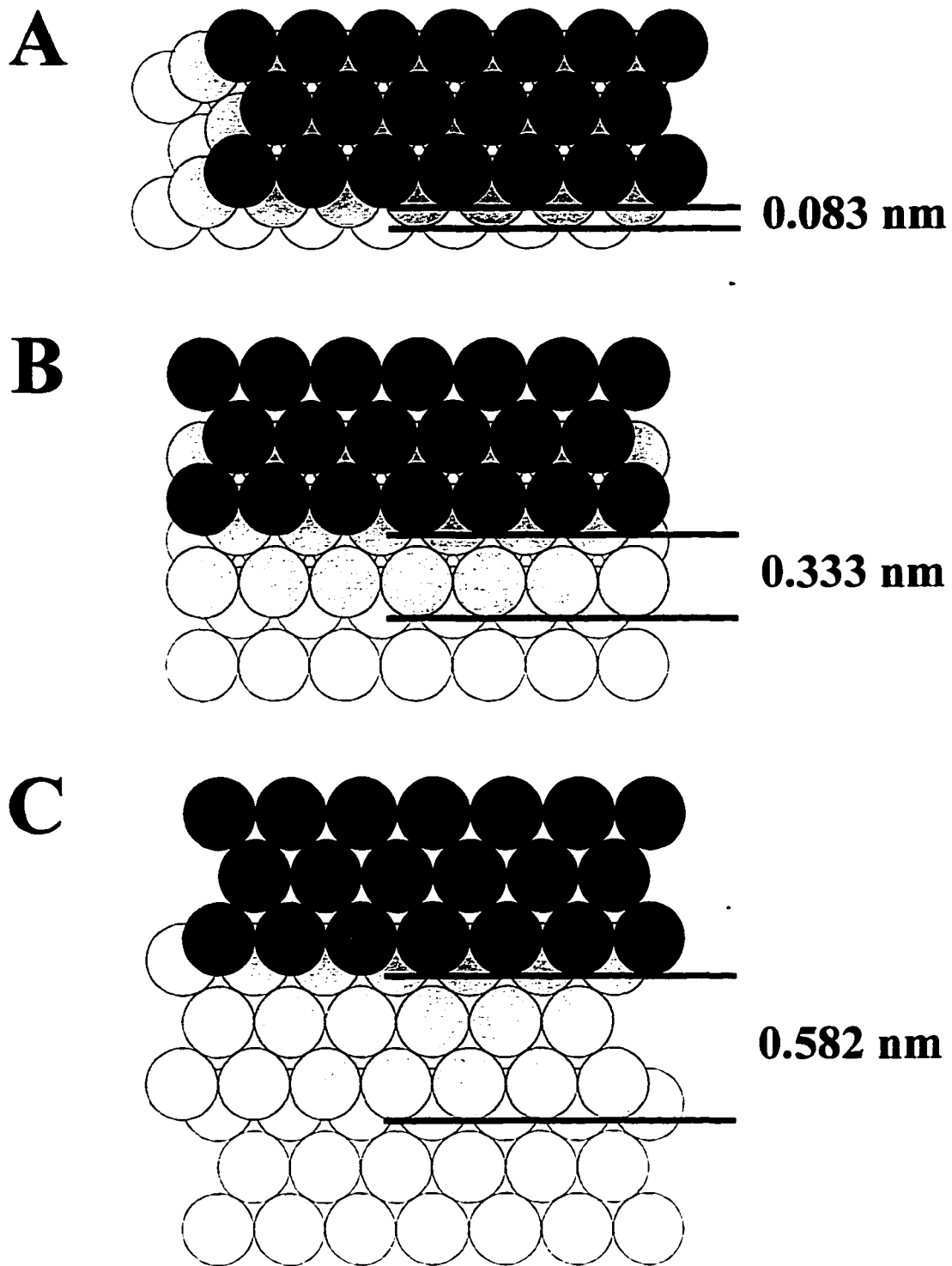


Figure 39

111 steps: A. is actually the 111 face.

Table 5 Step widths that were used for this model.

Step Direction Step Type	111	110	100
1	0.083 nm	0.144 nm	0.166 nm
2	0.333 nm	0.288 nm	0.416 nm
3	0.582 nm	0.432 nm	0.665 nm
4	0.831 nm	0.576 nm	0.915 nm
5		0.720 nm	

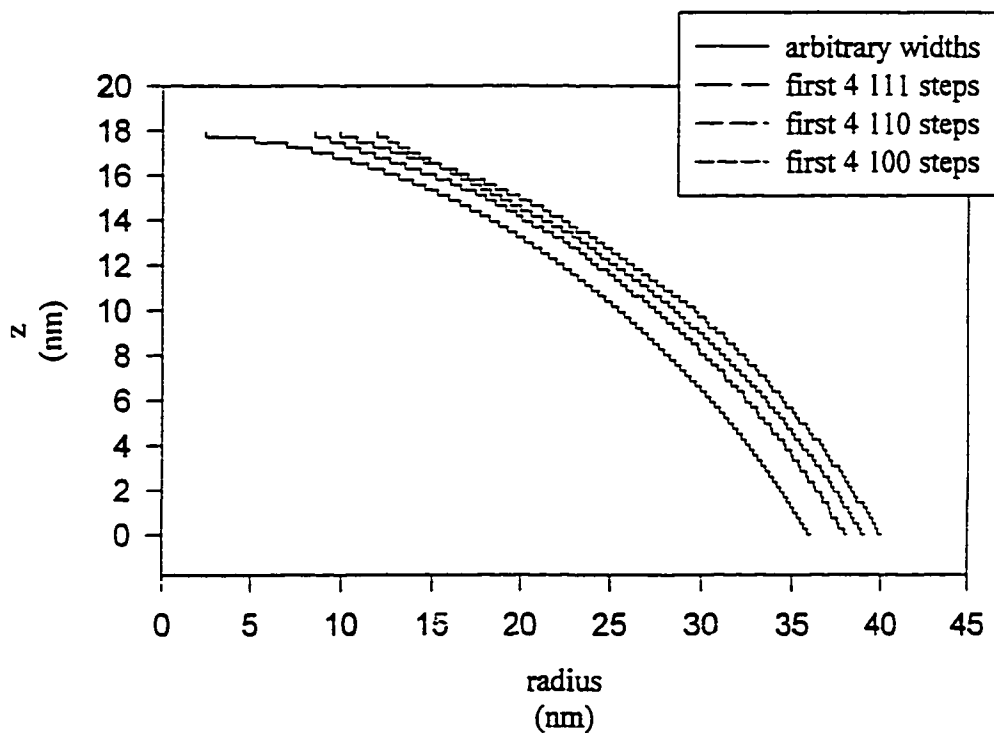


Figure 40 Using the first four steps in each of the three directions we can effectively model the lower portion of the hill ( which is the portion with the longest steps).



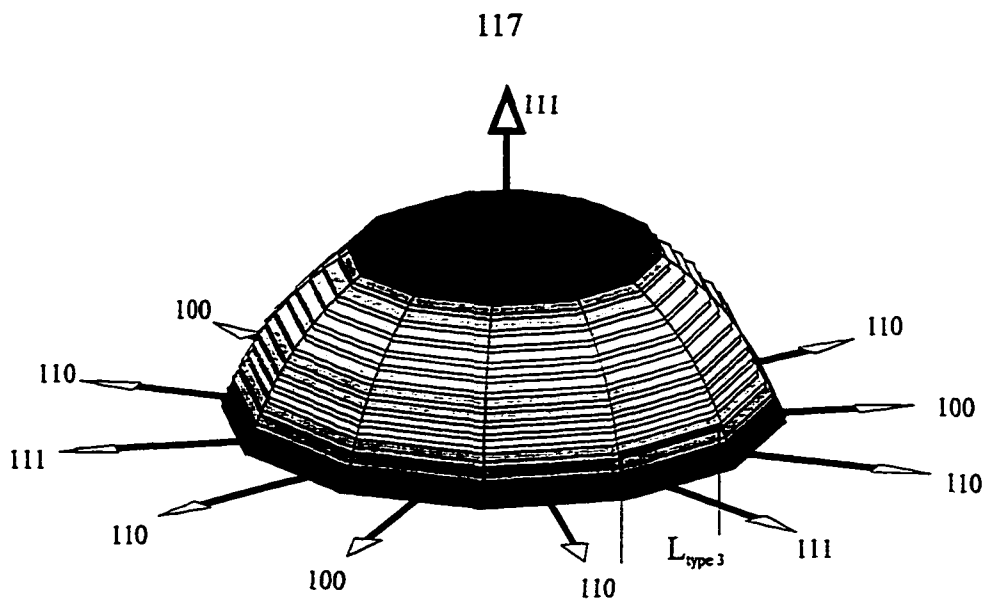


Figure 41 With the hill models, the  $L_d/A$  values are calculated by dividing the hill into the 12 sections, and fitting each direction to the first four narrow steps along each direction. These are shown in the previous figures 35 and 40. At this point, the structure of the hill is fixed, and the lengths of each step may be computed. For example there are 122733 Å of steps per hill, and of those there are 30683 Å steps are along the 111 direction, and 4388 Å of those are the type 3 steps shown in Figure 39B.

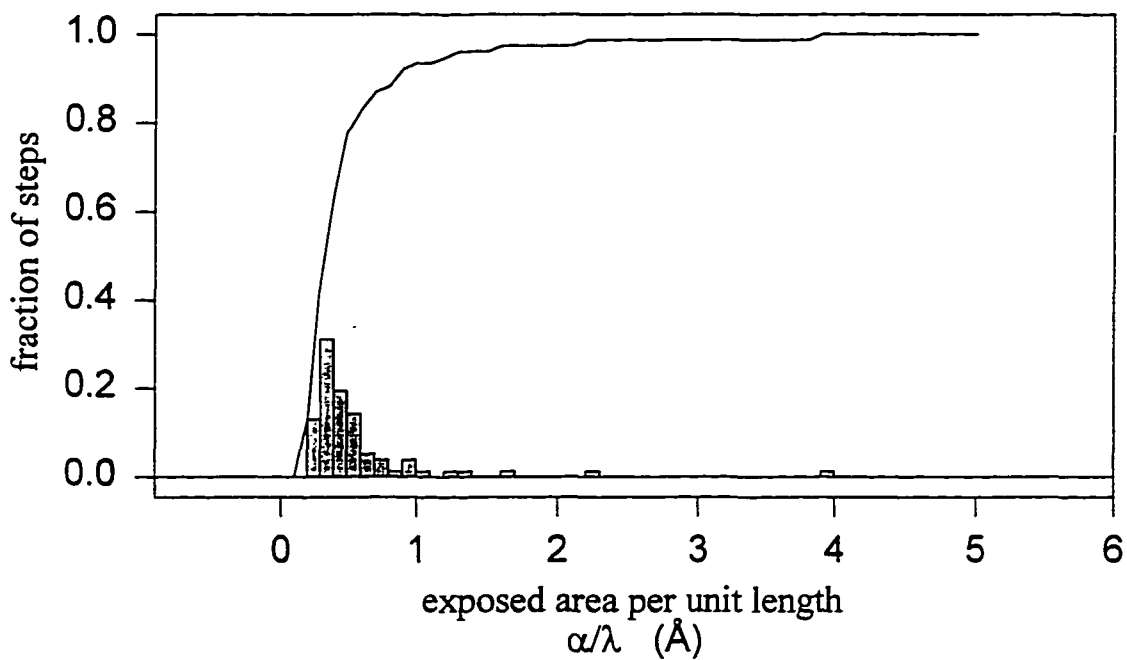


Figure 42 The histogram and its corresponding cumulative plot show that fully 90 % of the steps are less than 1 nm wide

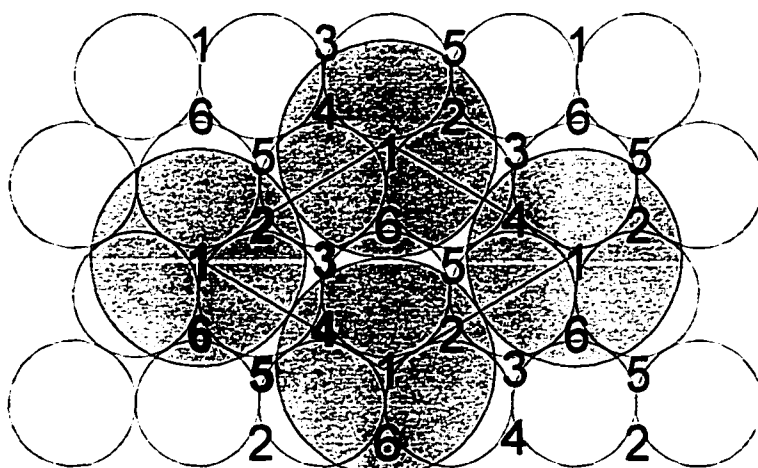


Figure 43

Once one thiolate adsorbs in one of the three-fold hollow sites, it defines a registry with respect to which all other thiolates adsorb.

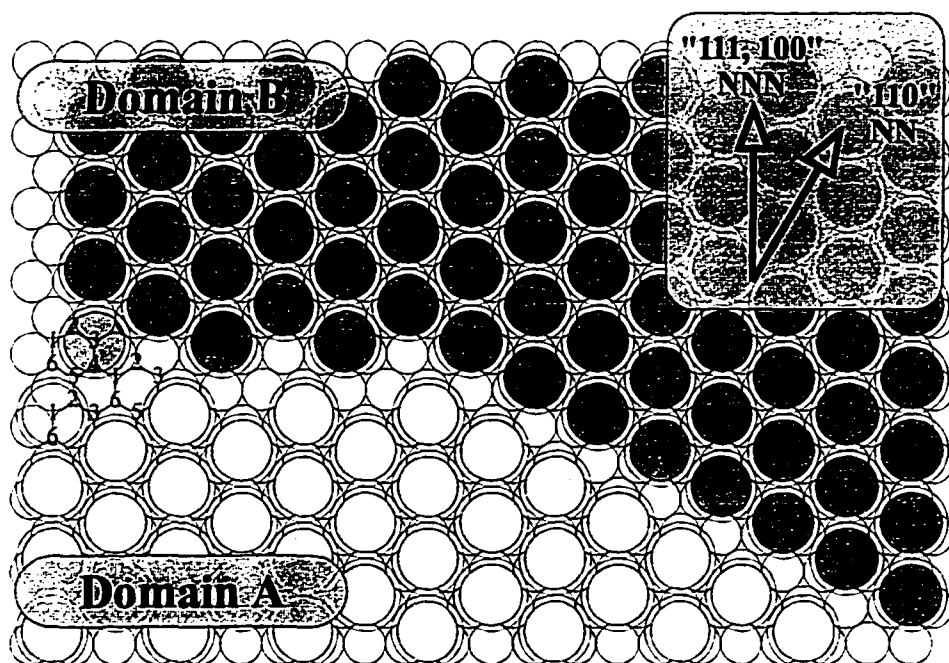


Figure 44

Experimentally it is common to observe domain boundaries which are at  $60^\circ$  (and occasionally  $30^\circ$ ) with respect to each other. This leads to the simplification of our model by considering only domain boundaries that occur along the Au nearest neighbor (NN) and next nearest neighbor (NNN) directions. The large circles correspond to the nearest neighbor spacing, and the inner circle corresponds to the van der Waals diameter of a polymethylene chain. These domain boundaries are type 1-3, as it occurs when domain type 1 grows into a domain of type 3.

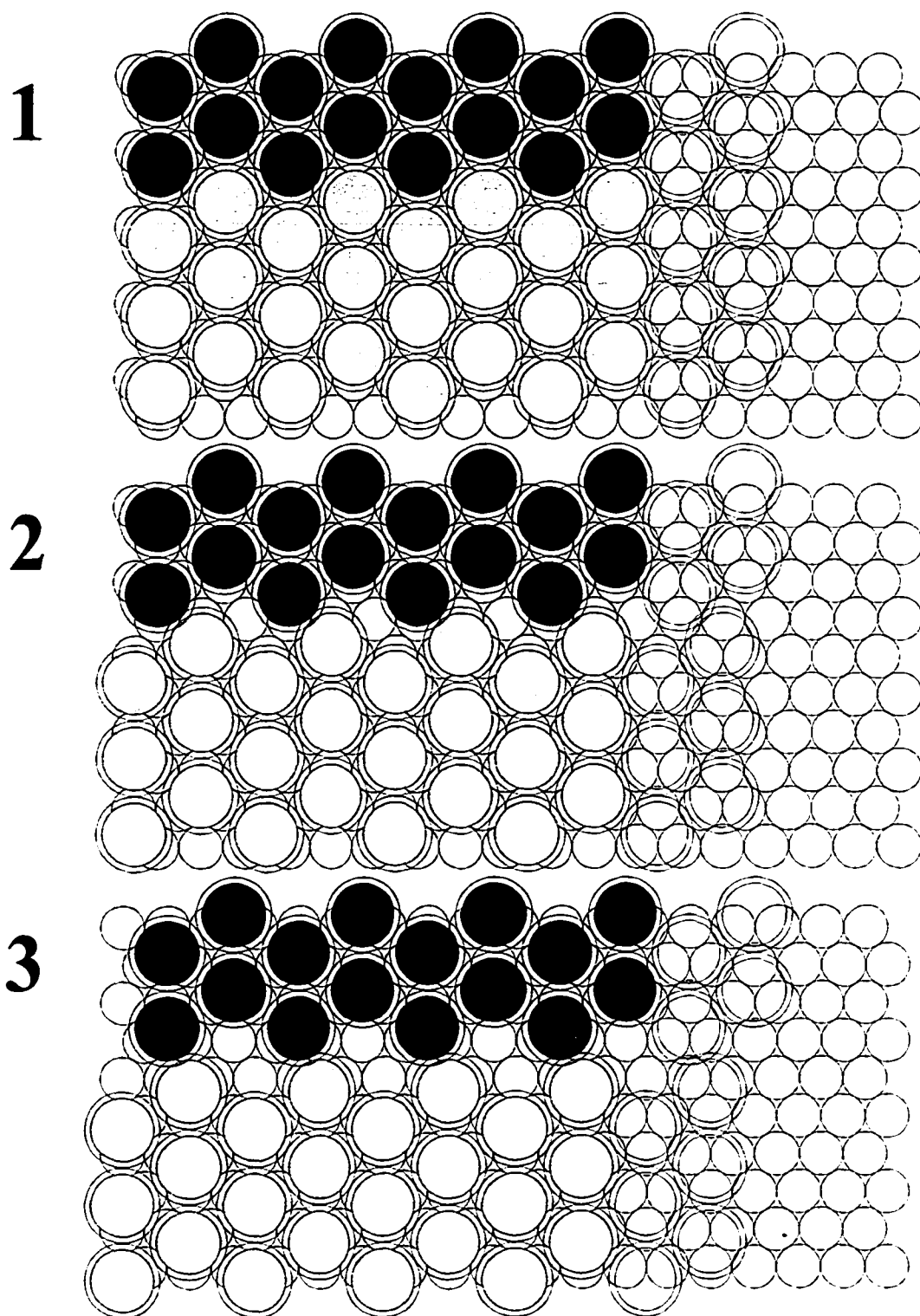


Figure 45

Domain boundaries perpendicular to the Au(NNN) direction.

1. no domain boundary at all (1-1, 2-2, 3-3, 4-4, 5-5, 6-6);
2. smallest *real* domain boundary (1-2, 1-4, 3-2, 3-6, 5-4, 5-6);
3. next smallest (2-1, 2-3, 4-1, 4-5, 6-3, 6-5)

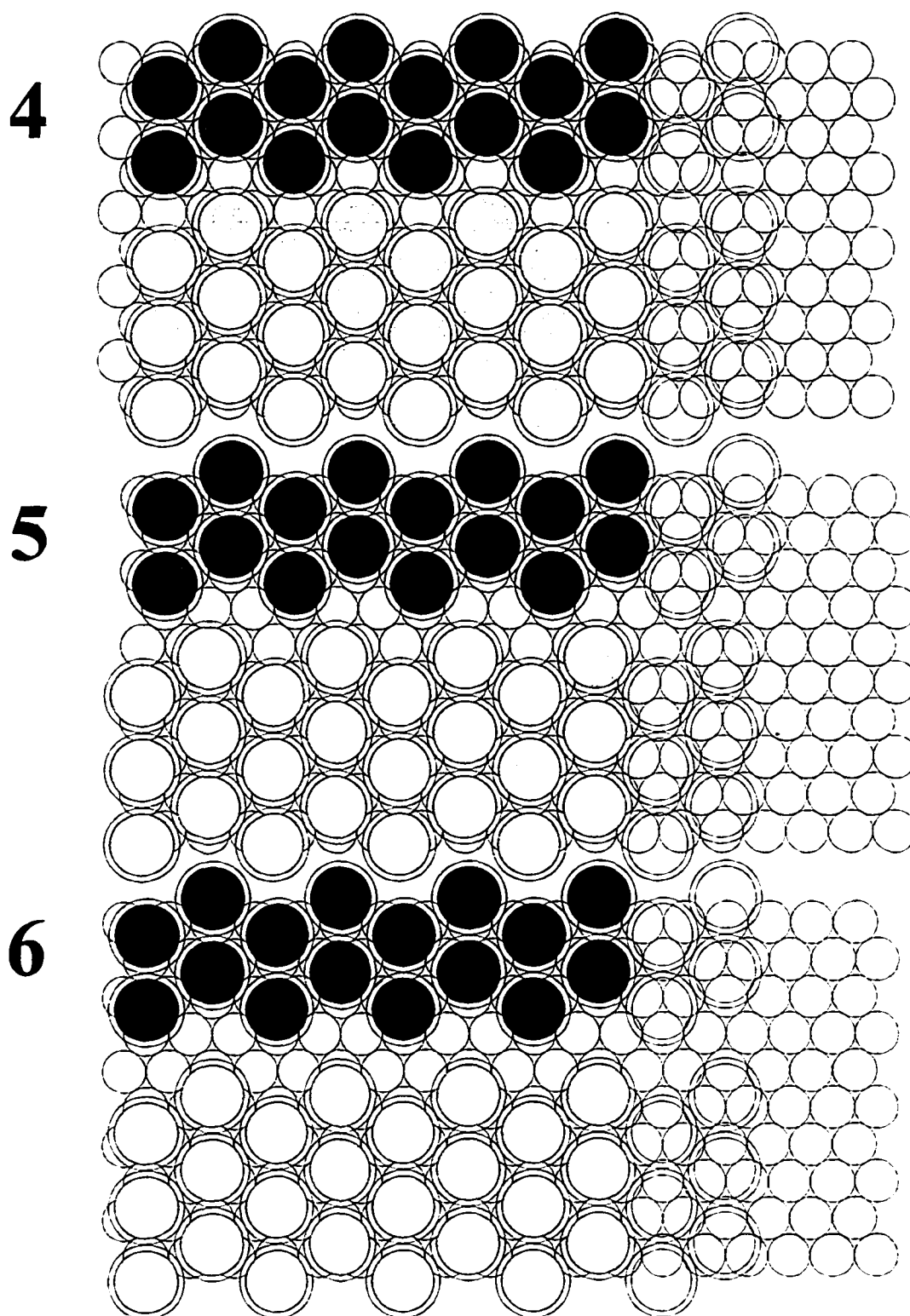


Figure 46

Domain boundaries perpendicular to the Au(NNN) direction.  
**4.** average domain boundary (2-5, 4-3, 6-1); **5.** most common  
 (1-3, 1-5, 2-4, 2-6, 3-1, 3-5, 4-2, 4-6, 5-1, 5-3, 6-2, 6-4);  
**6.** largest (2-1, 2-3, 4-1, 4-5, 6-3, 6-5)

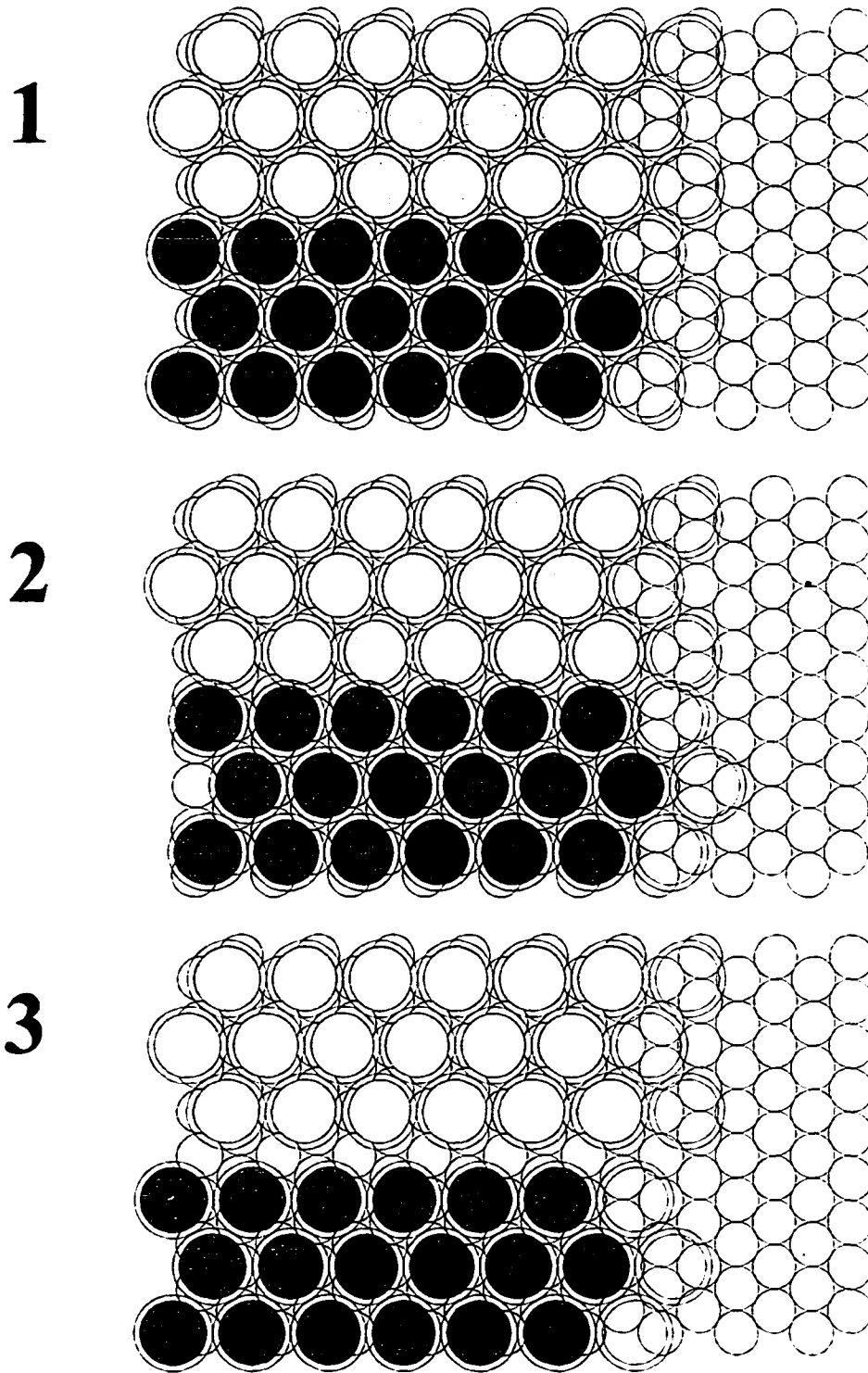


Figure 47

Domain boundaries perpendicular to the Au(NNN) direction.

1. no domain boundary at all (1-1, 2-2, 3-3, 4-4, 5-5, 6-6);
2. smallest *real* domain boundary (1-4, 2-3, 3-2, 4-1, 5-6, 6-5);
3. next smallest (1-2, 2-5, 3-6, 4-3, 5-4, 6-1).

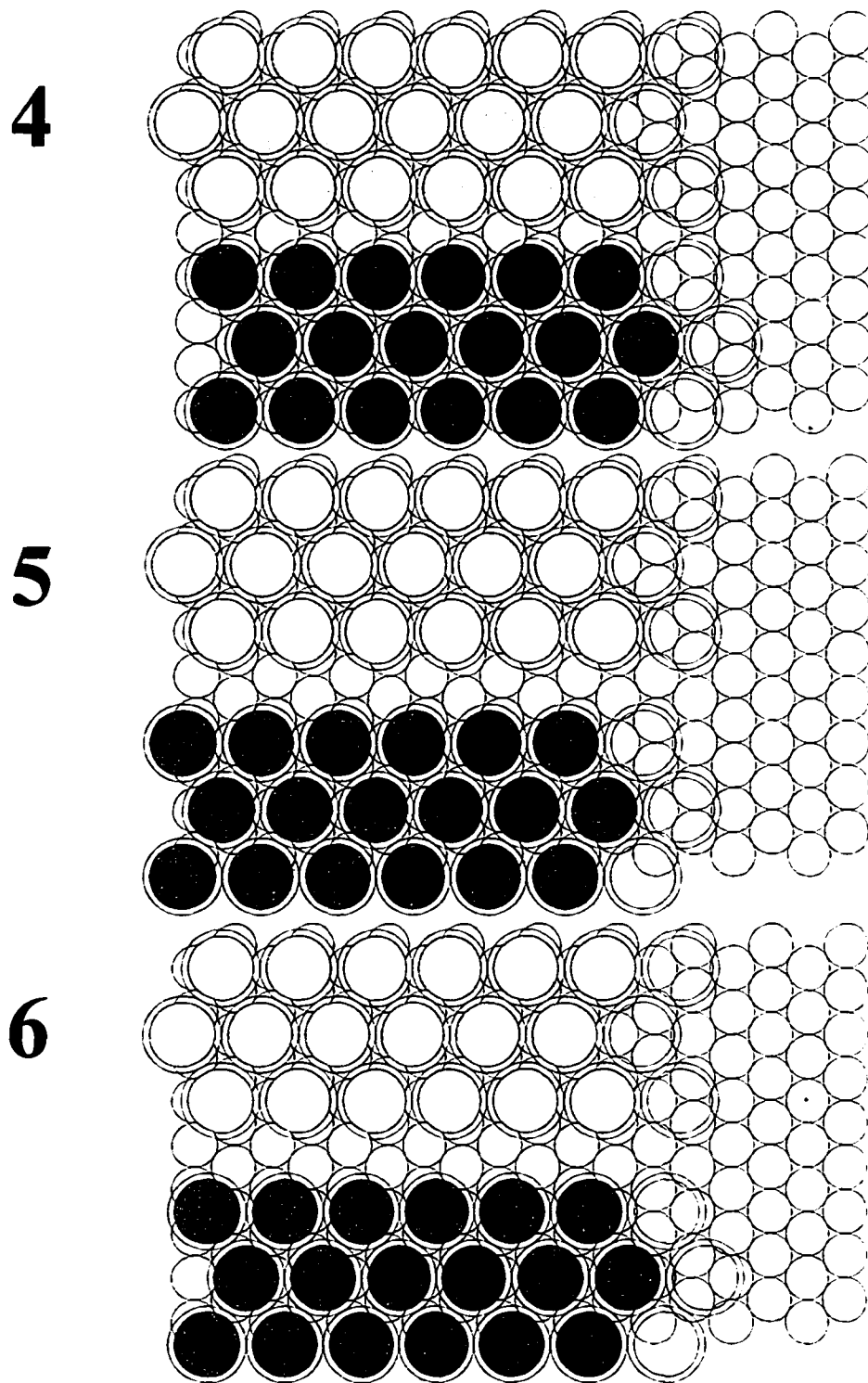


Figure 48

Domain boundaries perpendicular to the Au(NN) direction.  
 4. thin (1-3, 2-6, 3-5, 4-2, 5-1, 6-4); 5. wide-offset (1-5, 2-4,  
 3-1, 4-6, 5-3, 6-2); 6. wide(1-6, 2-1, 3-4, 4-5, 5-2, 6-3).

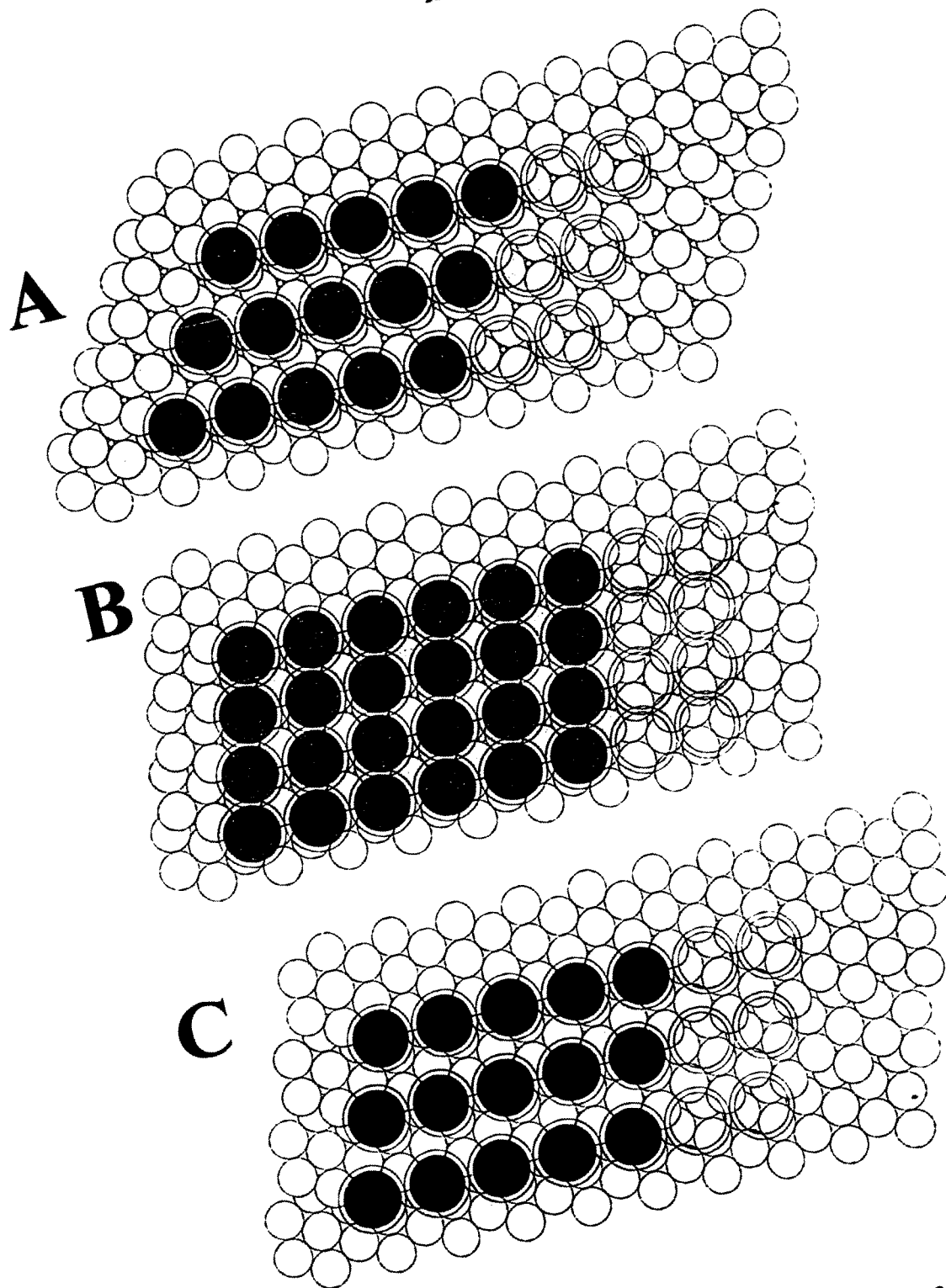


Figure 49 The 110 steps: A is type 2, B is type 3, and C is type 4.

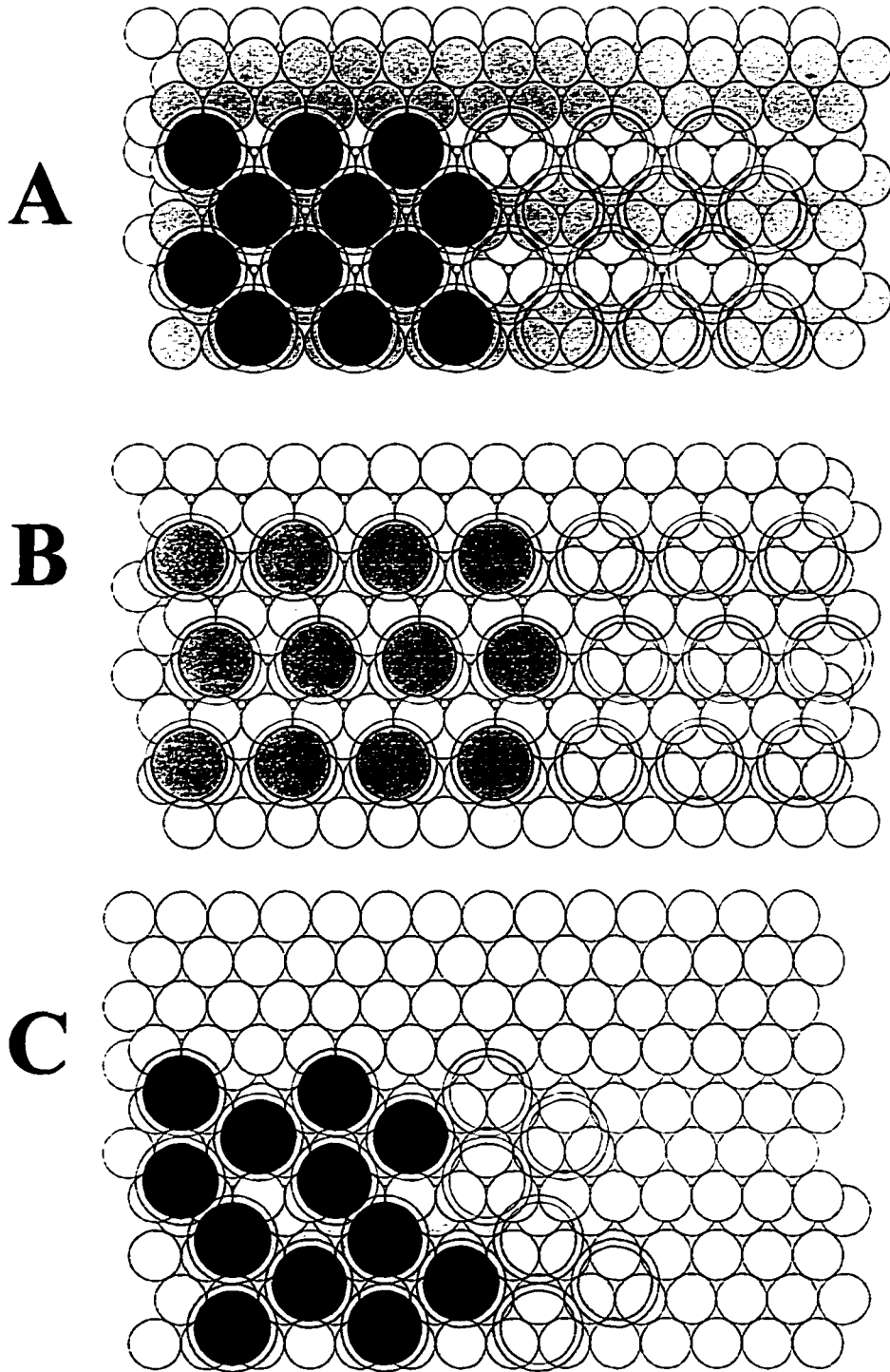


Figure 50

The 111 steps: A is type 2, B is type 3, and C is type 4.



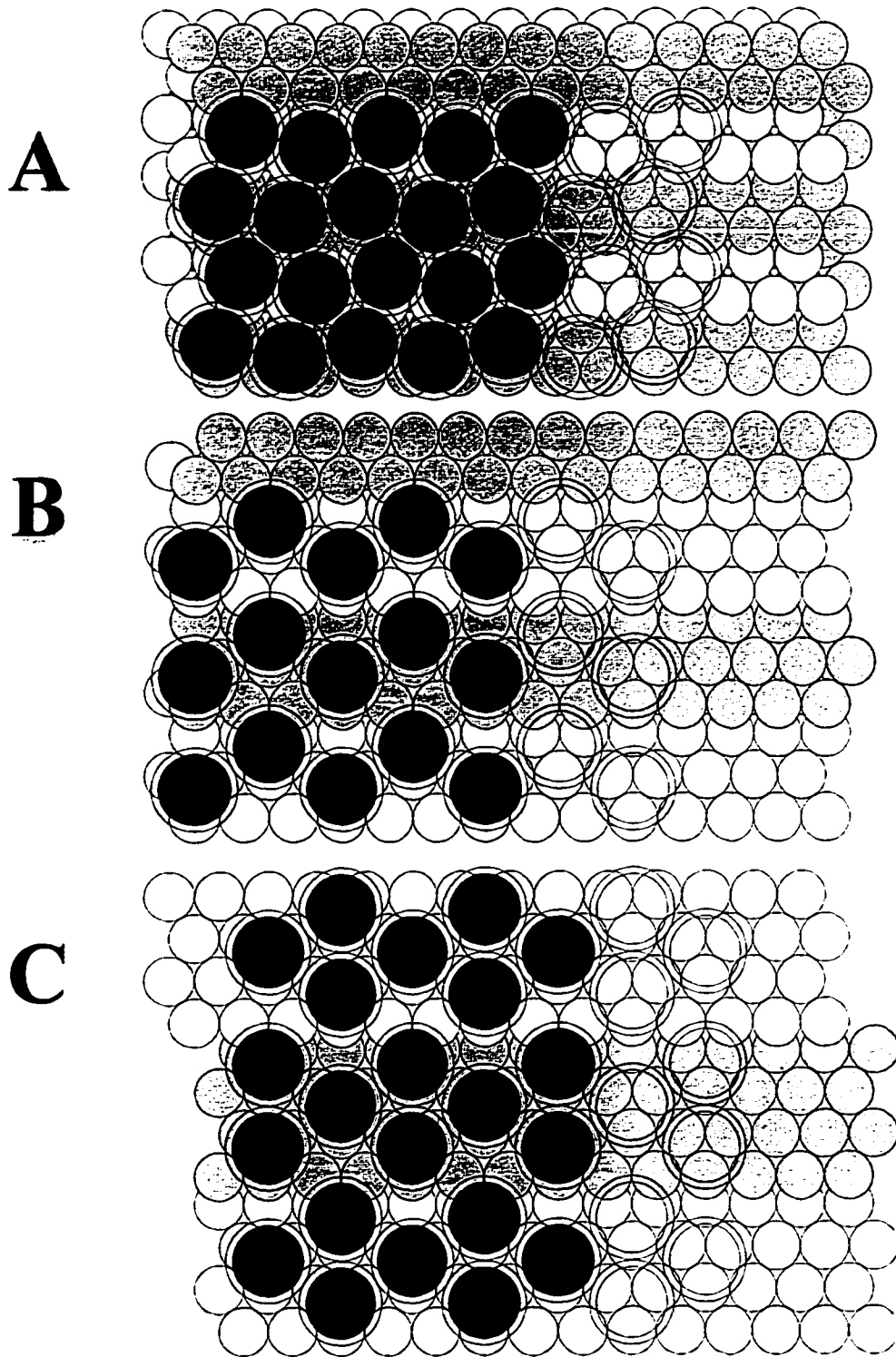


Figure 51

The 100 steps: A is type 2, B is type 3, and C is type 4.

**Table 6 Summary of Annealed Model Results**

defect type	direction <sup>a</sup>	list of configurations	probability <sup>b</sup>	L/A <sup>c</sup> nm <sup>-1</sup>	$\alpha/\lambda$ (vdW) <sup>d</sup> nm	f (vdW)
1	NNN	1-1, 2-2, 3-3, 4-4, 5-5, 6-6	0.0833	0.2	0.08753	0.001458
2	NNN	1-2, 1-4, 3-2, 3-6, 5-4, 5-6	0.0833	0.2	0.17067	0.002843
3	NNN	2-1, 2-3, 4-1, 4-5, 6-3, 6-5	0.0833	0.2	0.25381	0.004228
4	NNN	2-5, 4-3, 6-1	0.0417	0.2	0.25381	0.002117
5	NNN	1-3, 1-5, 2-4, 2-6, 3-1, 3-5, 4-2, 4-6, 5-1, 5-3, 6-2, 6-4	0.1667	0.2	0.33695	0.011234
6	NNN	2-1, 2-3, 4-1, 4-5, 6-3, 6-5	0.0417	0.2	0.42009	0.003504
1	NN	1-1, 2-2, 3-3, 4-4, 5-5, 6-6	0.0833	0.2	0.15161	0.002526
2	NN	1-4, 2-3, 3-2, 4-1, 5-6, 6-5	0.0833	0.2	0.15161	0.002526
3	NN	1-2, 2-5, 3-6, 4-3, 5-4, 6-1	0.0833	0.2	0.29561	0.004925
4	NN	1-3, 2-6, 3-5, 4-2, 5-1, 6-4	0.0833	0.2	0.29561	0.004925
5	NN	1-5, 2-4, 3-1, 4-6, 5-3, 6-2	0.0833	0.2	0.43961	0.007324
6	NN	1-6, 2-1, 3-4, 4-5, 5-2, 6-3	0.0833	0.2	0.43961	0.007324

- <sup>a</sup> NNN and NN stand for Au next-nearest-neighbor and Au nearest neighbor respectively, as seen in Figure 44.
- <sup>b</sup> The probability is determined from the number of configurations.
- <sup>c</sup> L/A is determined from the examination of domain boundary densities at images obtained both by our group as well as other groups. By measuring the total length of domain boundaries observed for an STM image of known geometric area, the defect density L/A can be easily determined. Interestingly, this number does not seem to vary too much from one experiment to the next.
- <sup>d</sup> This table of numbers was generated by assuming that the thiulates pack as hard spheres with diameters equal to the van der Waals diameters for polymethylene chains.

**Table 7 Summary of Unannealed Model Results**

defect type	direction <sup>a</sup>	probability <sup>b</sup>	L/A <sup>c</sup> nm <sup>-1</sup>	$\alpha/\lambda$ (vdW) <sup>d</sup> nm	f (vdW)
step type 1	100	0.0974	0.273	0.12942	0.034413
step type 2	100	0.0974	0.273	0.15425	0.041015
step type 3	100	0.0260	0.273	0.11004	0.007811
step type 4	100	0.0162	0.273	0.26743	0.011827
step type 1	110	0.0909	0.273	0.14781	0.036680
step type 2	110	0.2013	0.273	0.18542	0.101897
step type 3	110	0.0779	0.273	0.21187	0.045058
step type 4	110	0.0585	0.273	0.34208	0.054632
step type 1	111	0.0487	0.273	0.08753	0.011637
step type 2	111	0.1266	0.273	0.16496	0.057013
step type 3	111	0.0390	0.273	0.19697	0.020971
step type 4	111	0.0162	0.273	0.37858	0.016743

- <sup>a</sup> The directions point along the three basic directions illustrated in Figure 36
- <sup>b</sup> The probability is computed according to the model shown in Figures 33-42. The probability for a particular type of step is equal to the fractional length of that type of step with respect to the total length of all kinds of allowed steps.
- <sup>c</sup> L/A is computed from the total length of steps per unit area of the surface (geometric area).
- <sup>d</sup> This table of numbers was generated by assuming that the thiolates pack as hard spheres with diameters equal to the van der Waals diameters for polymethylene chains.

## REFERENCES

- 1 Israelachvili, J. N. *Intermolecular and Surface Forces: With Applications to Colloidal and Biological Systems*; Academic Press: San Diego, California 1985.
- 2 Drexler, K. E. *Nanosystems: Molecular Machinery, Manufacturing, and Computation*; John Wiley & Sons: New York, New York 1992.
- 3 Ulman, A. *An Introduction to Ultrathin Organic Films: From Langmuir Blodgett to Self-Assembly*; Academic Press: New York, New York 1991.
- 4 Hubbard, A. T. *The Handbook of Surface Imaging and Visualization*; CRC Press: New York, New York 1995.
- 5 Binnig, G.; Quate, C. F.; Gerber, C. *Physical Review Letters* 1986, 56, 930.
- 6 Tersoff, J.; Hamann, D. R. *Physical Review B* 1985, 31, 805.
- 7 Chen, C. J. *Introduction to Scanning Tunneling Microscopy*; Oxford University Press: New York, New York 1993.
- 8 Guntherodt, H.-J. *Forces in Scanning Probe Methods*; Kluwer Academic Publishers: Dordrecht, The Netherlands, 1995.
- 9 Fink, H. W. *IBM Journal of Research and Development* 1986, 30, 460.
- 10 Bonnell, D. A. *Scanning Tunneling Microscopy and Spectroscopy: Theory, Techniques and Applications*; VCH: New York, New York 1993.
- 11 Burnham, N. A.; Colton, R. J. "Force Microscopy" in *Scanning Tunneling Microscopy and Spectroscopy: Theory, Techniques and Applications*; VCH: New York, New York 1993, pp 191-249.
- 12 Sarid, D.; Elings, V. *Journal of Vacuum Science and Technology B* 1991, 9, 431.
- 13 Radmacher, M.; Tillmann, R. W.; Fritz, M.; Gaub, H. E. *Science* 1992, 257, 1900.
- 14 Meyer, G.; Amer, N. M. *Applied Physics Letters* 1988, 53, 1045.
- 15 Schonenberger, C.; Alvarado, S. F. *Reviews of Scientific Instruments* 1989, 60, 3131.
- 16 Siedle, P.; Butt, H.-J. *Langmuir* 1995, 11, 1065.

- 17 Neubauer, G.; Cohen, S. R.; McClelland, G. M.; Horne, D.; Mate, C. M. *Reviews of Scientific Instruments* **1990**, *61*, 2296.
- 18 Akamine, S.; Quate, C. F. *Journal of Vacuum Science and Technology B* **1992**, *10*, 2307.
- 19 Durig, U.; Zuger, O.; Stalder, A. *Journal of Applied Physics* **1992**, *72*, 1778.
- 20 Warmack, R. J.; Zheng, X.-Y.; Thundat, T.; Allison, D. P. *Reviews of Scientific Instruments* **1994**, *65*, 394.
- 21 Hoh, J. H.; Engel, A. *Langmuir* **1993**, *9*, 3310.
- 22 Grafstrom, S.; Ackermann, J.; Hagan, T.; Neumann, R.; Probst, O. *Journal of Vacuum Science and Technology B* **1994**, *12*, 1559.
- 23 Burnham, N. A. *Applied Physics Letters* **1993**, *63*, 114.
- 24 Burnham, N. A.; Colton, R. J.; Pollock, H. M. *Journal of Vacuum Science and Technology A* **1991**, *9*, 2548.
- 25 Burnham, N. A.; Colton, R. J. *Journal of Vacuum Science and Technology A* **1989**, *7*, 2906.
- 26 Overney, R. M.; Bonner, T.; Meyer, E.; Ruetschi, M.; Luthi, R.; Howald, L.; Frommer, J.; Fujihira, M.; Takano, H. *Journal of Vacuum Science and Technology B* **1994**, *12*, 1973.
- 27 Salmeron, M.; Folch, A.; Neubauer, G.; Tomitori, M.; Ogletree, D. F.; Kolbe, W. *Langmuir* **1992**, *8*, 2832.
- 28 Weisenhorn, A. L.; Hansma, P. K.; Albrecht, T. R.; Quate, C. F. *Applied Physics Letters* **1989**, *54*, 2651.
- 29 Ducker, W. A.; Senden, T. J.; Pashley, R. M. *Nature* **1991**, *353*, 239.
- 30 Ducker, W. A.; Senden, T. J.; Pashley, R. M. *Langmuir* **1992**, *8*, 1831.
- 31 Burnham, N. A. A Continuum Model for Force Microscopy Force Curve Data. In *Computations for the Nano-Scale*; Blochl, P. E., Ed.; Kluwer Academic Publishers: Dordrecht, The Netherlands, 1993; pp 199-207.
- 32 Burnham, N. A.; Dominguez, D. A.; Mowery, R. L.; Colton, R. J. *Physical Review Letters* **1990**, *64*, 1931.

- 33 Durig, U.; Zuger, O.; Pohl, D. W. *Journal of Microscopy* **1988**, *152*, 259.
- 34 Florin, E.-L.; Moy, V. T.; Gaub, H. E. *Science* **1994**, *264*, 415.
- 35 Moy, V. T.; Florin, E.-L.; Gaub, H. E. *Science* **1994**, *266*, 257.
- 36 Meyer, G.; Amer, N. M. *Applied Physics Letters* **1990**, *57*, 2089.
- 37 Baselt, D. R.; Baldeschwieler, J. D. *Journal of Vacuum Science and Technology B* **1992**, *10*, 2316.
- 38 Overney, R. M.; Takano, H.; Fujihira, M. *Physical Review Letters* **1994**, *72*, 3546.
- 39 Mate, C. M.; McClelland, G. M.; Erlandsson, R.; Chiang, S. *Physical Review Letters* **1987**, *59*, 1942.
- 40 Senden, T. J.; Drummond, C. J.; Kekicheff, P. *Langmuir* **1994**, *10*, 358.
- 41 Saenz, J. J.; Garcia, N.; Grutter, P.; Meyer, E.; Heinzlmann, H.; Weisendanger, R.; Rosenthaler, L.; Hidber, H. R.; Guntherodt, H.-J. *Journal of Applied Physics* **1987**, *62*, 4293.
- 42 Weisendanger, R.; Shvets, I. V.; Burgler, D.; Tarrach, G.; Guntherodt, H.-J.; Coey, J. M. D. *Zeitschrift fur Physik B, Condensed Matter* **1992**, *86*, 1.
- 43 Martin, Y.; Williams, C. C.; Wickramasinghe, H. K. *Journal of Applied Physics* **1987**, *61*, 4723.
- 44 Martin, Y.; Wickramasinghe, H. K. *Applied Physics Letters* **1987**, *50*, 1455.
- 45 Tsao, Y.-H.; Yang, S. X.; Evans, D. F. *Langmuir* **1992**, *8*, 1188.
- 46 Tsao, Y.-H.; Evans, D. F.; Wennerstrom, H. *Science* **1993**, *262*, 547.
- 47 Tsao, Y.-H.; Yang, S. X.; Evans, D. F.; Wennerstrom, H. *Langmuir* **1991**, *7*, 3154.
- 48 Ohnesorge, F.; Binnig, G. *Science* **1993**, *260*, 1451.
- 49 Lin, F.; Meier, D. J. *Langmuir* **1994**, *10*, 1660.
- 50 Yang, J.; Shao, Z. *Ultramicroscopy* **1993**, *50*, 157.
- 51 Marti, O.; Drake, B.; Hansma, P. K. *Applied Physics Letters* **1987**, *51*, 484.

- 52 Manne, S.; Hansma, P. K.; Massie, J.; Elings, V. B.; Gewirth, A. A. *Science* **1991**, *251*, 183.
- 53 Zhong, W.; Overney, G.; Tomanek, D. *Europhysics Letters* **1991**, *15*, 49.
- 54 Porter, M. D.; Bright, T. B.; Allara, D. L.; Chidsey, C. E. D. *Journal of the American Chemical Society* **1987**, *109*, 3559.
- 55 Li, T. T.-T.; Weaver, M. J. *Journal of the American Chemical Society* **1984**, *106*, 6107.
- 56 Zhong, C.-J.; Porter, M. D. *Analytical Chemistry* **1995**, *67*, 709A.
- 57 Bain, C. D.; Whitesides, G. M. *Journal of the American Chemical Society* **1989**, *110*, 5897.
- 58 Bryant, M. A.; Pemberton, J. E. *Journal of the American Chemical Society* **1991**, *113*, 8284.
- 59 Nuzzo, R. G.; Zegarski, B. R.; Dubois, L. H. *Journal of the American Chemical Society* **1987**, *109*, 733.
- 60 Zhong, C.-J.; Porter, M. D. *Journal of the American Chemical Society* **1994**, *116*, 11616.
- 61 Sellers, H.; Ulman, A.; Shnidman, Y.; Eilers, J. E. *Journal of the American Chemical Society* **1993**, *115*, 9389.
- 62 Walczak, M.M.; Alves, C. A.; Lamp, B.D.; Porter, M.D. *Journal of Electroanalytical Chemistry*. **1995**, *396*, 103.
- 63 Samant, M. G.; Brown, C. A.; Gordon, J. G. *Langmuir* **1991**, *7*, 437.
- 64 Camillone, N.; Chidsey, C. E. D.; Liu, G.-Y.; Scoles, G. *Journal of Chemical Physics* **1993**, *98*, 3503.
- 65 Chidsey, C. E. D.; Liu, G.-Y.; Rowntree, P.; Scoles, G. *Journal of Chemical Physics* **1989**, *91*, 4421.
- 66 Strong, L.; Whitesides, G. M. *Langmuir* **1988**, *4*, 546.
- 67 Evans, S. E.; Ulman, A. *Chemical Physics Letters* **1990**, *170*, 462

- 68 Widrig, C. A.; Alves, C. A.; Porter, M. D. *Journal of the American Chemical Society* **1991**, *113*, 2805.
- 69 Chidsey, C. E. D.; Loiacono, D. N. *Langmuir* **1990**, *6*, 682.
- 70 Mizutani, W.; Anselmetti, D.; Michel, B. in *Atomic and Nanometer-Scale Modification of Materials: Fundamentals and Applications* a NATO ASI Series E: Applied Sciences, edited by Phaedon Avouris; Kluwer Academic Publishers: Dordrecht, The Netherlands, **1993**, *239*, pp. 43-48.
- 71 Kim, Y. T.; McCarley, R. L.; Bard, A. J. *Journal of Physical Chemistry* **1992**, *96*, 7416.
- 72 Schoenenberger, C.; Sondag-Huethorst, J. A. M.; Jorritsma, J.; Fokkink, L. G. J. *Langmuir* **1994**, *10*, 611.
- 73 Edinger, K.; Goelzhaeuser, A.; Demota, K.; Woell, C.; Grunze, M. *Langmuir* **1993**, *9*, 4.
- 74 Sondag-Huethorst, J. A. M.; Schoenenberger, C.; Fokkink, L. G. J. *Journal of Physical Chemistry* **1994**, *98*, 6826.
- 75 Durig, U.; Zuger, O.; Michel, B.; Haussling, L.; Ringsdorf, H. *Physical Review B* **1993**, *48*, 1711.
- 76 Delamarche, E.; Michel, B.; Gerber, C.; Anselmetti, D.; Guntherodt, H.-J.; Wolf, H.; Ringsdorf, H. *Langmuir* **1994**, *10*, 2869.
- 77 Poirier, G. E.; Tarlov, M. J.; Rushmeier, H. E. *Langmuir* **1994**, *10*, 3383.
- 78 Poirier, G. E.; Tarlov, M. J. *Langmuir* **1994**, *10*, 2853.
- 79 Delamarche, E.; Michel, B.; Kang, H.; Gerber, C. *Langmuir* **1994**, *10*, 4103.
- 80 Schoenenberger, C.; Jorritsma, J.; Sondag-Huethorst, J. A. M.; Fokkink, L. G. J. *Journal of Physical Chemistry* **1995**, *99*, 3259.
- 81 Poirier, G. E.; Tarlov, M. J. *Journal of Physical Chemistry* **1995**, *99*, 10966.
- 82 Fenter, P.; Eisenberger, P.; Liang, K. S. *Physical Review Letters* **1993**, *70*, 2447.
- 83 Dubois, L. H.; Zegarski, B. R.; Nuzzo, R. G. *Journal of Chemical Physics* **1993**, *98*, 678.



- 84 Nuzzo, R. G.; Korenic, E. M.; Dubois, L. H. *Journal of Chemical Physics* **1990**, *93*, 767.
- 85 Alves, C. A.; Smith, E. L.; Porter, M. D. *Journal of the American Chemical Society* **1992**, *114*, 1222.
- 86 Alves, C. A.; Porter, M. D. *Langmuir* **1993**, *9*, 3507.
- 87 McDermott, C. A.; McDermott, M. T.; Green, J.-B.; Porter, M. D. *Journal of Physical Chemistry* **1995**, *99*, 13257.
- 88 Butt, H.-J.; Seifert, K.; Bamberg, E. *Journal of Physical Chemistry* **1993**, *97*, 7316.
- 89 Pan, J.; Tao, N.; Lindsay, S. M. *Langmuir* **1993**, *9*, 1556.
- 90 Liu, G.-y.; Salmeron, M. B. *Langmuir* **1994**, *10*, 367.
- 91 Tupper, K. J.; Colton, R. J.; Brenner, D. W. *Langmuir* **1994**, *10*, 2041.
- 92 Tupper, K. J.; Brenner, D. W. *Langmuir* **1994**, *10*, 2335.
- 93 Kim, Y. T.; Bard, A. J. *Langmuir* **1992**, *8*, 1096.
- 94 Bucher, J.-P.; Santesson, L.; Kern, K. *Langmuir* **1994**, *10*, 979.
- 95 Sun, L.; Crooks, R. M. *Journal of the Electrochemical Society* **1991**, *138*, L23.
- 96 Anselmetti, D.; Gerber, C.; Michel, B.; Wolf, H.; Guentherodt, H. J.; Rohrer, H. *Europhysics Letters* **1993**, *23*, 421.
- 97 Mizutani, W.; Michel, B.; Schierle, R.; Wolf, H.; Rohrer, H. *Applied Physics Letters* **1993**, *63*, 147.
- 98 Stranick, S. J.; Parikh, A. N.; Tao, Y. T.; Allara, D. L.; Weiss, P. S. *Journal of Physical Chemistry* **1994**, *98*, 7636.
- 99 Han, T.; Beebee, T. P. *Langmuir* **1994**, *10*, 2705.
- 100 Chailapakul, O.; Sun, L.; Xu, C.; Crooks, R. M. *Journal of the American Chemical Society*, **1993**, *115*, 12459.
- 101 McCarley, R. L.; Dunaway, D. J.; Willicut, R. J. *Langmuir* **1993**, *9*, 2775.

- 102 McCarley, R. L.; Kim, Y.-T.; Bard, A. J. *Journal of Physical Chemistry* **1993**, *97*, 211.
- 103 Stranick, S. J.; Parikh, A. N.; Allara, D. L.; Weiss, P. S. *Journal of Physical Chemistry* **1994**, *98*, 11136.
- 104 Sprik, M.; Delamarche, E.; Michel, B.; Roethlisberger, U.; Klein, M. L.; Wolf, H.; Ringsdorf, H. *Langmuir* **1994**, *10*, 4116.
- 105 Sun, L.; Crooks, R. M. *Langmuir* **1993**, *9*, 1951.
106. Dubois, L. H. and Nuzzo, R. G. *Annual Reviews of Physical Chemistry* **1992**, *43*, 437.
107. Goss, C. A.; Brumfield, J. C.; Irene, E. A.; Murray, R. W. *Langmuir* **1993**, *9*, 2986.
- 108 At higher magnifications, STM images of alkanethiolate monolayers also show the presence of small (2-5 nm) depressions at annealed gold that are not found at unannealed gold. These depressions, which have a depth consistent with that of a single atom step at a Au(111) surface, arise largely from an adsorbate driven reconstruction of the underlying substrate, see ref. 87. In a preliminary investigation aimed at assessing whether depressions are the cause of the counter-intuitive correlation of roughness and barrier properties, we have characterized the barrier properties and depressions densities at monolayers formed at gold films that were annealed at different temperatures. These results indicated that monolayers formed at surfaces with increased roughness but similar depressions densities functioned as much more effective barrier films (C. J. Zhong, C. A. McDermott, and M. D. Porter, unpublished results).
- 109 Salmeron, M.; Neubauer, G.; Folch, A.; Tomitori, M.; Ogletree, D. F.; Sautet, P. *Langmuir* **1993**, *9*, 3600.
- 110 Salmeron, M. B. *MRS Bulletin* **1993**, *1993*, 20.
- 111 Thomas, R. C.; Houston, J. E.; Crooks, R. M.; Kim, T.; Michalske, T. A. *Journal of the American Chemical Society* **1995**, *117*, 3830.
- 112 Houston, J. E.; Michalske, T. A. *Nature* **1992**, *356*, 266.
- 113 Joyce, S. A.; Thomas, R. C.; Houston, J. E.; Michalske, T. A.; Crooks, R. M. *Physical Review Letters* **1992**, *68*, 2790.
- 114 Joyce, S. A.; Houston, J. E.; Michalske, T. A. *Applied Physics Letters* **1992**, *60*, 1175.

- 115 Thomas, R. C.; Houston, J. E.; Michalske, T. A.; Crooks, R. M. *Science* **1993**, *259*, 1883.
- 116 Thomas, R. C.; Tangyunyong, P.; Houston, J. E.; Michalske, T. A.; Crooks, R. M. *Journal of Physical Chemistry* **1994**, *98*, 4493.
117. Chidsey, C. E. D. *Science* **1991**, *251*, 919.
- 118 Rowe, G. K. and Creager, S. E. *Langmuir* **1994**, *10*, 1186.
- 119 Miller, C.; Cuendet, P.; Grätzel, M. *Journal of Physical Chemistry* **1991**, *95*, 877.
120. López, G. P.; Biebuyck, H. A.; Härter, R.; Kumar, A.; Whitesides, G. M. *Journal of the American Chemical Society* **1993**, *115*, 10774.
- 121 Singhvi, R.; Kumar, A.; López, G.; Stephanopoulos, G. N.; Wang, D. I. C.; Whitesides, G. M.; Ingber, D. E. *Science* **1994**, *264*, 696.
122. Spinke, J.; Liley, M.; Guder, H.-J.; Angermaier, L.; Knoll, W. *Langmuir* **1993**, *9*, 1821.
123. Bailey, A. I. and Courtney-Pratt, J. S. *Proceedings of the Royal Society London A*, **1954**, *227*, 501.
- 124 Levine, O. and Zisman, W. A. *Journal of Physical Chemistry* **1957**, *61*, 1068.
125. Briscoe, B. J. and Evans, D. C. B. *Proceedings of the Royal Society London A* **1982**, *380*, 389.
126. Yoshizawa, H.; Chen, Y.-L.; Israelachvili, J. *Journal of Physical Chemistry* **1993**, *97*, 4128.
- 127 Yoshizawa, H.; McGuiggan, P.; Israelachvili, J. *Science* **1993**, *259*, 1305.
128. DePalma, V. and Tillman, N. *Langmuir* **1989**, *5*, 868.
- 129 Timsit, R. S. in *Fundamentals of Friction: Macroscopic and Microscopic Processes*; Singer, I. L.; Pollock, H. M. Eds.; Kluwer Academic Press: Dordrecht, The Netherlands, **1992**; p 287.
130. Chidsey, C. E. D.; Loiacono, D. N.; Sleator, T.; Nakahara, S. *Surface Science* **1988**, *200*, 45.
- 131 Pierce, M.; Stuart, J.; Pungor, A.; Dryden, P.; Hlady, V. *Langmuir* **1994**, *10*, 3217.

- 132 Lee, G. U.; Chrisey, L. A.; Colton, R. J. *Science* **1994**, *266*, 771.
- 133 Fujihira, M.; Kawate, H.; Yasutake, M. paper presented at the 183rd Meeting of the Electrochemical Society, Honolulu, HI, 18 May 1993.
- 134 Nakagawa, T.; Ogawa, K.; Kurumizawa, T.; Ozaki, S. *Japanese Journal of Applied Physics* **1993**, *32*, L294.
- 135 Hoh, J. H.; Cleveland, J. P.; Prater, C. B.; Revel, J.-P.; Hansma, P. K. *Journal of the American Chemical Society* **1992**, *114*, 4917.
- 136 Mate, C. M. *Wear* **1993**, *168*, 17.
- 137 Erlandsson, R.; Hadziioannou, G.; Mate, C. M.; McClelland, G. M.; Chiang, S. *Journal of Chemical Physics* **1988**, *89*, 5190.
- 138 Cohen, S. R.; Neubauer, G.; McClelland, G. M. *Journal of Vacuum Science and Technology A* **1990**, *8*, 3449.
- 139 Nie, H. Y.; Mizutani, W.; Tokumoto, H. *Surface Science* **1994**, *311*, L649.
140. Mate, C. M. *Physical Review Letters* **1992**, *68*, 3323.
- 141 Haugstad, G.; Gladfelter, W. L.; Weberg, E. B.; Weberg, R. T., Weatherill, T. D. *Langmuir* **1994**, *10*, 4295.
142. Meyer, E.; Overney, R.; Brodbeck, D.; Howald, L.; Lüthi, R.; Frommer, J. and Güntherodt, H. -J. *Physical Review Letters*, **1992**, *69*, 1777.
143. Liu, Y.; Wu, T. and Evans, D.F. *Langmuir* **1994**, *10*, 2241.
144. Overney, R. M.; Meyer, E.; Frommer J.; Güntherodt, H.-J.; Fujihira M.; Takano, H.; Gotoh, Y. *Langmuir* **1994**, 1281.
- 145 Overney, R. M.; Meyer, E.; Frommer J.; Brodbeck, D.; Lüthi, R.; Howald. L.; Güntherodt, H.-J.; Fujihira M.; Takano, H.; Gotoh, Y. *Nature* **1992**, *359*, 133.
146. Frisbie, C.D.; Rozsnyai, L. F.; Noy, A.; Wrighton, M. S. Lieber, C. M. *Science* **1994**, *265*, 2071.
- 147 Wilbur, J. L.; Biebuyck, H. A.; MacDonald, J. C.; Whitesides, G. M. *Langmuir* **1995**, *11*, 825.
148. O'Shea, S. J.; Welland, M. E.; Wong, T. M. H. *Ultramicrosc.* **1993**, *52*, 55.

149. Greenwood, J. A. . in *Fundamentals of Friction: Macroscopic and Microscopic Processes*; Singer, I. L.; Pollock, H. M. Eds.; Kluwer Academic Press: Dordrecht, The Netherlands, 1992; p 57.
150. Yoshizawa, H. and Israelachvili, J. *Journal of Physical Chemistry*, 1993, 97, 11300.
151. Tomanek, D.; Zhong, W.; Thomas, H. *Europhysics Letters* 1991, 15, 887.
152. Because the stick-slip results from a cantilever instability, the absolute corrugation amplitude will depend strongly on the magnitude of  $k_t$ .
153. Binnig, G. *Ultramicroscopy* 1992, 42-44, 7.
154. Equation 1 is derived from the expression relating the friction force to shear stress,  $f = S_c A$  where  $S_c$  is the critical stress required to shear the junction and  $A$  is the contact area [Bowden, F. P. and Tabor, D. *The Friction and Lubrication of Metals, Pt. 1*; Oxford Univ. Press: Oxford 1950.] and the linear relationship between shear stress and contact pressure from Eyring's model,  $\tau = \tau_0 + \alpha p$ , where  $\tau$  is also shear stress and  $p$  is the pressure. Substituting  $\tau$  for  $S_c$  we obtain,  $f = (\tau_0 + \alpha p)A$  and since  $p = F_N/A$ , then  $f = \alpha F_N + \tau_0 A$  which is essentially Equation 1 if we equate  $f_0$  and  $\tau_0 A$ .
155. Eyring, H.; *Journal of Chemical Physics* 1935, 3, 107.
156. Eyring, H. *Journal of Chemical Physics* 1936, 4, 283.
157. Tupper, K. J. and Brenner, D. W. *Thin Solid Films* 1994, 253, 185.
158. Bain, C. D.; Troughton, E. B.; Tao, Y.-T.; Evall, J.; Whitesides, G. M.; Nuzzo, R. G. *Journal of the American Chemical Society* 1989, 111, 321.
159. Bain, C. D. and Whitesides, G. M. *Journal of the American Chemical Society* 1989, 111, 7164.
160. Wood, K. A.; Snyder, R. G.; Strauss, H. L. *Journal of Chemical Physics* 1989, 91, 5255.
161. Evans, S. D.; Goppert-Berarducci, K. E.; Uranker, E.; Gerenser, L. J.; Ulman A.; Snyder, R. S. *Langmuir* 1991, 7, 2700.
162. Stole, S. Ph.D. Dissertation, Iowa State University, Ames Iowa, 1990.
163. The frequency of the  $\nu_s(\text{CH}_2)$  mode and the frequency and bandwidth of the  $\nu_s(\text{CH}_2)$  mode also follow the same general trend with  $n$  as  $\Delta\nu_{1/2}$  shown in Figure 2B.

164. Snyder, R. G.; Strauss, H. L.; Elliger, C. A. *Journal of Physical Chemistry* **1982**, *86*, 5145.
165. Nuzzo, R. G.; Dubois, L. H.; Allara, D. L. *Journal of the American Chemical Society* **1990**, *112*, 558.
166. D. Tabor, in *Fundamentals of Friction: Macroscopic and Microscopic Processes*; Singer, I. L.; Pollock, H. M. Eds.; Kluwer Academic Press: Dordrecht, The Netherlands, 1992; p. 3.
167. Green, J.-B. D.; McDermott, M. T.; Porter, M. D.; Siperko, L. M. *Journal of Physical Chemistry* **1995**, *99*, 10960.
168. Noy, A.; Frisbie, C. D.; Rozsnyai, L. F.; Wrighton, M. S.; Lieber, C. M. *Journal of the American Chemical Society* **1995**, *117*, 7943.
169. Mallouk, T. E.; Harrison, D. J. *ACS Symposium Series 561: Interfacial Design and Chemical Sensing*; ACS: Washington, DC **1994**.
170. Waldeck, D. H.; Beratan, D. N. *Science* **1993**, *261*, 576.
171. Wise, K. D.; Najafi, K. *Science* **1991**, *254*, 1335.
172. Wrighton, M. S. *Science*. **1986**, *231*, 32.
173. Rugar, D.; Züger, O.; Hoen, S.; Yannoni, C. S.; Vieth, H.-M.; Kendrick, R. D. *Science* **1994**, *264*, 1560.
174. Radmacher, M.; Fritz, M.; Cleveland, J. P.; Walters, D. A.; Hansma, P. K. *Langmuir* **1994**, *10*, 3809.
175. Meyer, E.; Overney, R. M.; Lüthi, R.; Howald, L.; Frommer, J.; Güntherodt, H.-J.; Wolter, O.; Fujihira, M.; Takano, H.; Gotoh, Y. *Thin Solid Films* **1992**, *220*, 132.
176. Winograd, N. *Analytical Chemistry* **1993**, *65*, 622A.
177. Benninghoven, A.; Hagenhoff, B.; Niehuis, E. *Analytical Chemistry* **1993**, *65*, 630A.
178. Tarlov, M. J.; Burgess, D. R. F. Jr.; Gillen, G. *Journal of the American Chemical Society* **1993**, *115*, 5305.
179. López, G. P.; Biebuyck, H. A.; Whitesides, G. M. *Langmuir* **1993**, *9*, 1513.
180. Wollman, E. W.; Frisbie, C. D.; Wrighton, M. S. *Langmuir* **1993**, *9*, 1517.

181. Dunn, R. C.; Holtom, G. R.; Mets, L.; Xie, X. S. *Journal of Physical Chemistry* **1994**, *98*, 3094.
182. Betzig, E.; Trautman, J. K. *Science* **1992**, *257*, 189.
183. Ullmann, R. and Kolb, D. M. University of Ulm, personal communication, **1994**.
184. The expected trend in surface free energy from wettability measurements is:  
-CH<sub>3</sub> < -CH<sub>2</sub>Br < -CO<sub>2</sub>CH<sub>3</sub> < -CH<sub>2</sub>OH ~ -CO<sub>2</sub>H [ref. 158].
185. Zhong, C-J.; McDermott, M. T.; Green, J-B., D.; Porter, M. D. unpublished results.
186. Bilayers can also be formed through this dimerization by a gas phase deposition process. (Sun, L.; Kepley, L. J.; Crooks, R. M. *Langmuir* **1992**, *8*, 2101.)
187. Kendall, K. *Nature* **1986**, *319*, 203.
188. Pollock, H. M. in *Fundamentals of Friction: Macroscopic and Microscopic Processes*; Singer, I. L.; Pollock, H. M. Eds.; Kluwer Academic Press: Dordrecht, The Netherlands, 1992; pp. 77-94.
189. Zisman, W. A. *Advances in Chemistry Series* **1964**, *43*, 1.
190. Kumar, A.; Biebuyck, H. A.; Whitesides, G. M. *Langmuir* **1994**, *10*, 1498.
191. Gee, M. L.; McGuiggan, P. M.; Israelachvili, J. N.; Homola, A. M. *Journal of Chemical Physics* **1990**, *93*, 1895.
192. The first term in Equation 1 has the same form as Amonton's Law,  $f = \mu F_N$ , which describes the macroscopic friction between rough surfaces. Although the coefficient of friction,  $\mu$ , and  $\alpha$  are both invariant with normal force, these parameters have different origins [191]. A more complete description of the chemical origins of  $\alpha$  and  $f_0$  at a variety of chemically different surfaces will be the subject of a future report [McDermott, M. T.; Green, J.-B., D.; Porter, M. D. manuscript in preparation.].
193. Although our measurements were made under an atmosphere of flowing argon, it is likely that an adsorbed layer of impurities (e.g., water) exists on the surfaces of the tips and the samples. A component of the observed frictional differences would therefore contain a contribution from interactions with the adsorbed layer. Such a contribution would nevertheless be expected to follow the amount of adsorbed layer present, which would be controlled by the free energies of the surfaces. Experiments are underway to delineate the role of adsorbed layers on our measurements. Interestingly, a recent study on the effect of relative humidity (RH) on AFM-measured friction at both

hydrophilic and hydrophobic surfaces found no detectable changes in the friction below a RH of 75% [Binggeli, M. and Mate, C. M. *Appl. Phys. Lett.* **1994**, *65*, 415.]. In addition, frictional contrasts similar to those in Figures 3 and 4 between segregated -CO<sub>2</sub>H and -CH<sub>3</sub> regions has been observed at a wide range of humidities [ref. 146] and under ethanol [ref. 147].

- 194 Bain, C. D.; Whitesides, G. M. *Langmuir* **1989**, *5*, 1370.
195. A value for  $W_{ad}$  can also be calculated from  $W_{ad} = 2 \Phi (\gamma_1 \gamma_2)^{1/2}$  [Girifalco, L. A.; Good, R. J. *Journal of Physical Chemistry* **1957**, *61*, 904]. Using a representative value for the constant  $\Phi$  of an immiscible system,  $\Phi(\text{water-tetradecane}) = 0.53$ ,  $W_{ad} = 33 \text{ mJ/m}^2$ . This value of  $W_{ad}$  translates to a  $\gamma_{12} = 36 \text{ mJ/m}^2$  which compares well with our estimated limits.
- 196 Myers, D. *Surfaces, Interfaces, and Colloids: Principles and Applications* VCH Publishers: New York, 1991, p.139.
197. Ellipsometric results for *n*-alkanoic acid monolayers adsorbed on Ag yield a thickness of a stearic acid layer between 1.8-2.4 nm depending on the chain tilt [Tao, Y.-T. *Journal of the American Chemical Society* **1993**, *115*, 4350].
- 198 Quate, C.F. *Surface Science* **1994**, *299/300*, 980.
- 199 Magonov, S.N. *Applies Spectroscopy Reviews* **1993**, *28*, 1.
- 200 Blackman, G.S.; Mate, C.M.; Philpot, M.R. *Physical Review Letters* **1990**, *65*, 2270.
- 201 Fujihira, M.; Kawate, H.; Yasutake, M. *Chemistry Letters* **1992**, *1992*, 2223.
- 202 Marti, A.; Hahner, G.; Spencer, N.D. *Langmuir* **1995**, *11*, 4632.
- 203 Berger, C.E.H.; Werf, K.O.v.d.; Kooyman, R.P.H.; Grooth, B.G.d.; Greve, J. *Langmuir* **1995**, *11*, 4188.
- 204 Meyer, E.; Heinzelmann, H.; Grutter, P.; Jung, T.; Hidber, H.-R.; Rudin, H.; Guntherodt, H.-J. *Thin Solid Films* **1989**, *181*, 527.
- 205 Haussling, L.; Michel, B.; Ringsdorf, H.; Rohrer, H. *Angew. Chem. Int. Ed. Engl.* **1991**, *30*, 569.
- 206 Lee, G.U.; Kidwell, D.A.; Colton, R.J. *Langmuir* **1994**, *10*, 354.
- 207 Stuart, J.K.; Hlady, V. *Langmuir* **1995**, *11*, 1368.



- 208 Walczak, M.M.; Popenoe, D.D.; Deinhammer, R.S.; Lamp, B.D.; Chung, C.; Porter, M.D. *Langmuir* **1991**, *7*, 2687.
- 209 The charging current at the negative limit of the potential scan includes a small contribution of background leakage current from a marginally passivated metal clip used to make electrical contact with the probe tip. Experiments using a conventional electrochemical cell invariably exhibit a larger charging current at the positive as opposed to negative potential limit of such scans.
- 210 Bard, A.J.; Faulkner, L.R. *Electrochemical Methods*; John Wiley and Sons: New York, **1980**.
- 211 Popenoe, D.D.; Deinhammer, R.S.; Porter, M.D. *Langmuir* **1992**, *8*, 2521, and references therein.
- 212 Abbott, N.L.; Whitesides, G.M. *Langmuir* **1994**, *10*, 1493.
- 213 Sondag-Huethorst, J.A.M.; Fokkink, L.G.J. *Langmuir* **1992**, *8*, 2560.
- 214 We also considered the possibility of a potential dependent change in the double layer structure at the solution side of the FcT-solution interface that results from the redox transformation of the ferrocenyl group. We do not, however, detect a difference in the approach curves that would support this possibility.
- 215 Rowe, G.K.; Creager, S.E. *Langmuir* **1991**, *7*, 2307.